RAMAN SCATTERING STUDIES AND CHARGE TRANSPORT IN POLYFLUORENES

A Dissertation
Presented to
The Faculty of the Graduate School
University of Missouri-Columbia

In Partial Fulfillment

Of the Requirements for the Degree

Doctor of Philosophy

By

MOHAMMAD ALI IFTEKHAR ARIF

Dr. Suchi Guha,

Dissertation Supervisor

August 2007

The undersigned, appointed by the dean of the Graduate School, have examined the dissertation entitled

“RAMAN SCATTERING STUDIES AND CHARGE TRANSPORT IN POLYFLUORENES”

Presented by MOHAMMAD ALI IFTEKHAR ARIF

A candidate for the degree of Doctor of Philosophy

And hereby certify that, in their opinion, it is worthy of acceptance.

_____

Professor Suchismita Guha

_____

Professor Meera Chandrasekhar

_____

Professor Shubhra Gangopadhyay

_____

Professor Giovanni Vignale

_____

Professor Ping Yu

Dedicated to my parents

ACKNOWLEDGEMENTS

I wish to express my heartfelt gratitude and sincere thanks to my research supervisor Dr. Suchi Guha, assistant professor of Physics Department of physics and Astronomy, University of Missouri Columbia (MU). Without her valuable suggestion, inspiring guidance, constant supervision and encouragement throughout the whole period of work, it would not be possible to complete the job with my little endeavor.

I am also grateful to Dr. Shubhra Gangopadhyay, professor of Electrical and Computer engineering (ECE), for her continuous suggestion and help in the electrical characterization and analysis of the data throughout the project.

I would like to thank my entire committee: Dr. Meera Chandrasekhar, Dr. Shubhra Gangopadhyay, Dr. Giovanni Vignale and Dr. Ping Yu for their continuous suggestions throughout this work.

I would also like to graciously thank our collaborators: Dr. Kartik Ghosh, associate professor, and graduate student, Lamine Fadiga of Physics, Astronomy and Materials Science, Missouri State University, for ITO preparation and AFM analysis; Professor M. Winokur, University of Wisconsin-Madison for the XRD measurements and analysis; Professor U. Scherf , F. Galbrecht and A. Tsami Bergische Universität Wuppertal, Makromolekulare Chemie, Wuppertal, Germany for providing the PF2/6 sample; Chris. Volz an undergraduate student, in the Department of Physics (MU) for theoretical calculation of the vibrational spectra ; research associate Dr. Maruf

Hossain (ECE, MU) for sputterd ITO growth, and graduate student Minseong Yun for ellipsometry and C-V measurements.

I appreciate the generous support from the funding agencies, University of Missouri Research Board grant and the National Science Foundation to accomplish this project.

At a personal level I would like to express my special gratitude to my parents and all of my brothers and sister for their unconditional and continued inspiration throughout the whole period of this undertaking.

Finally, I wish to dedicate this work to my loving parents. Their lifelong support and caring has been instrumental in my life. Thank you all.

TABLE OF CONTENTS

LIST OF FIGURES

CHAPTER 2

CHAPTER 3

CHAPTER 4

CHAPTER 5

CHAPTER 6

CHAPTER 7

LIST OF TABLES

LIST OFABBREVIATIONS

a-a-a	*anti-anti-anti* (all *anti*-alkyl side chain conformation)
a-g-g	*anti-gauche-gauche* side chain conformation
BWF	Breit-Wigner-Fano
CCD	Charge-coupled-device
CDT	Cambridge Display Technology
$CHCl_3$	Chloroform
Cl-φ	Chlorobenzene
CP	Cojugated Polymer
C-V	Capacitance-Voltage
DI	Di-ionized water
D-LAM	Distorted longitudinal accordion motion
EL	Electroluminescence
ETL	Electron transport layer
FET	Field effect transistor
FWHM	Full width at half maximum
HOMO	Highest occupied molecular orbital
HTL	Hole transport layer
ITO	Indium tin oxide
I-V	Current-Voltage
LAM	Longitudinal accordion motion
LCDs	Liquid crystal displays
LCP	Liquid crystal polymer

LED	Light-Emitting-Diode
LEP	Light-emitting- polymer
LUMO	Lowest unoccupied molecular orbital
m-AC	Metastable as-cast
n-LC	Nematic liquid crystal
PA	Polyacetylenes
PEDOT-PSS	Poly (3,4- ethylene dioxy-2,4-thiophene) poly sulphonate
PF	Polyfluorene
PF2/6	Poly[9,9'-(di 2-ethylhexyl)fuorene]
PF8	Poly [(9,9'-(di n, octyl)fluorene]
PL	Photoluminescence
PLD	Pulsed-laser deposition
PLE	Photoluminescence excitation
PLED	Polymer-light-emitting-diode
PPPs	Polyparaphenylenes
PPV	Poly-phenylene vinylene
RGB	Red-Green-Blue
RT	Room temperature
SCLC	Space-Charge-Limited Conduction
SMOLED	Small molecule organic-light-emitting-diode
TCLC	Trapped Charge Limited Current
TSC	Thermally Stimulated Current
XRD	X-ray diffraction

GLOSSARY

Annealing: is a heat treatment process that alters the microstructure of a material causing changes in properties.

Aggregates: the aggregates are characterized by delocalization of the electronic wave function among two or more chains in both the ground and excited states.

Backbone: this term characterizes the atoms and bonds along the shortest connection between the beginning and the end of the polymer chain. Attached to the backbone there are hydrogen and other atoms, or longer side groups.

Bias (forward, reverse): a bias is an external voltage applied to a diode. When the negative pole of the external voltage is attached to the n-doped semiconductor, it is called forward bias, when the positive pole is attached to the n-doped semiconductor; it is called a reverse bias.

Bipolaron: if two charge carriers share the same molecular deformation, a bipolaron is formed so a bipolaron is a bound state of two charged solitons of like charge with two corresponding midgap levels.

Chiral center: an atom in a molecule that is bonded to four different chemical species allowing for optical isomerism.

Conformations: in chemistry, the conformation of a molecule is its structure and in polymer chemistry it is the three dimensional shape of the molecular chain.

Cold crystallization: some glass forming polymer may develop a semicrystalline state characterized by a folded lamellar morphology at the nanometer level when they are heated from the glassy state above the glass transition temperature T_g, this process is frequently referred to as cold crystallization.

Conjugated polymer: the term conjugated means that along the backbone the bonds between carbon atoms alter between single and double bonds along the polymer chain. Since the electrons of the double bonds are delocalized, they form a band structure extended over the whole range of the effective conjugation length.

Conjugation length: conjugation length is the length of a completely undisturbed alternating single and double bond segment, being planar and allowing maximum overlap of π-electrons. This is the ideal case. The effective conjugation length is often shorter than the conjugation length, where impurities, distortions, shifts, or any other kind of irregularities limit the overlap of π-electrons.

Dimer: a dimer refers to a molecule composed of two similar subunits or monomers linked together. It is a special case of a polymer.

Diode: a semiconductor sandwich with n and p doping

Doping: introduction of charge carriers in to a semiconductor either by chemical doping (permanent) or injection/hole pairs.

Electroluminescence (EL): is an optical phenomenon and electrical phenomenon where a material emits light in response to an electric current passed through it, or to a strong electric field. Electroluminescence is the result of radiative recombination of electrons and holes in a material (usually a semiconductor). The excited electrons release their energy as photons – light.

Excimers: an excimer (originally short for excited dimer) is a short-lived dimeric or heterodimeric molecule formed from two species, at least one of which is in an electronic excited state. In an excimer, the exciton is delocalized over two molecules, i.e., $A^* + A \rightarrow A_2^*$ (A_2^* = excimer). The lifetime of an excimer is very short, on the order of nanoseconds.

Exciplex: an electronically excited complex of definite stoichiometry, 'non-bonding' in the ground state. For example, a complex formed by the interaction of an excited molecular entity with a ground state counterpart of a different structure. Like the excimer, the exciplex is only bound in the excited states.

Excitons: a fundamental quantum of electronic excitation in condensed matter, consisting of a negatively charged electron and a positively charged hole bound to each other by electrostatic attraction.

Heat treatment: is the technique of controlled heating and cooling of materials to alter their physical and mechanical properties without changing the product shape.

HOMO: the Highest Occoupied Molecular Orbital is defined as the bonding electronic state highest in energy and can be seen as something similar to the highest state of the occupied valance band in an inorganic semiconductor. Since the electronic states in a polymer or oligomer are not dense enough to be realistically described as bands, the molecular orbitals are a better approximation. The orbitals below the HOMO are often described as HOMO-1, HOMO-2...

Isomer: a chemical structure with definite formula for which there exists one or more distinct structures with the same formula.

Isotropic phase: phase with random alignment and no long range order.

Liquid crystal: an intermediate phase between crystalline solid and isotropic liquids.

Luminescence: a general term which describes any process in which energy is emitted from a material at a different wavelength from that at which it is absorbed. Luminescence can be caused by chemical or biochemical changes, electrical energy, subatomic motions, reactions in crystals, or stimulation of an atomic system.

Luminescence quenching: radiationless redistribution of excitation energy via interaction (electronic energy or charge transfer) between an emitting species and the quencher.

LUMO: The LUMO is the lowest anti-bonding electronic orbital in a molecule. It can be seen as similar to the conduction band. The levels above the LUMO are often written as LUMO+1, LUMO+2...

Mesomorphic state: a state of matter where the degree of molecular order is intermediate between the perfect three dimensional long range positional and orientational order found in solid crystal and the absence of long range order found in isotropic liquids, gases and amorphous solids.

Metastable state: particular excited state of an atom, nucleus, or other system that has a longer lifetime than the ordinary excited states and that generally has a shorter lifetime than the lowest, often stable, energy state, called the ground state. A metastable state may thus be considered a kind of temporary energy trap or a somewhat stable intermediate.

Monomer: a unit of several atoms, which can form larger chains in repetition by chemically bonded to other monomers to form a polymer.

Nematic-liquid crystal: a nematic liquid crystal is a transparent or translucent liquid that causes the polarization (that is, the focusing in a plane) of light waves to change as the waves pass through the liquid. The extent of the change in polarization depends on the intensity of an applied electric field.

OLED: organic-light-emitting diode, is a display device that sandwiches carbon-based films between two charged electrodes, one a metallic cathode and one a transparent anode, usually being glass. The organic films consist of a hole-injection layer, a hole-transport layer, an emissive layer and an electron-transport layer. When voltage is applied to the OLED cell, the injected positive and negative charges recombine in the emissive layer and create electroluminescent light.

Oligomer: a chain consisting of several monomers. These chains are usually formed when two hydrogen atoms or side groups attached to two monomer units are re- placed by a bond to attach to another monomer unit. Oligomers usually consist of repetitive units from two to ten.

Organic: based on the most common molecules found in all life that are based on chains of carbonates with side groups consisting of carbon, hydrogen, nitrogen, oxygen, sulfur etc.

Peierls instability: according to Peierl, the interplay or competition between the energy of π - electron system and the lattice (elastic) energy causes distortion or instability in the polymer chain due to break of translational symmetry in the chain of equidistantly placed atoms, correspondingly creates long-short-long-short alternation in the carbon-carbon distances, reminiscent of alternating single and double chemical bonds. This lattice distortion is also referred to as 'dimerisation', while the chain with equidistant inter-atomic separation is termed 'undimerised'.

Phonons: is a quantized mode of vibration occurring in a crystal lattice, such as the atomic lattice of a solid and play a major role in many of the physical properties of solids, including a material's thermal and electrical conductivities.

Photoluminescence (PL): is a process in which a chemical compound absorbs a photon (electromagnetic radiation), thus transitioning to a higher electronic energy state, and then radiates a photon back out, returning to a lower energy state. The period between absorption and emission is typically extremely short, on the order of 10 nanoseconds. The PL spectra give an idea about the probability that radiative recombination occurs and at which energies the material absorbs and emits.

Plasmons: is the quasiparticle resulting from the quantization of plasma oscillations. They are a hybrid of the electron plasma (in a metal or semiconductor) and the photon. Thus, plasmons are collective oscillations of the free electron gas at optical frequencies.

Polarons: it is energetically favorable for a material to deform its lattice around an excess electron/hole, which can be imagined as a cloud of phonons around the charge carrier. Such an electron/hole surrounded by a phonon cloud is called a polaron. Polarons are quasiparticles and can be thought of as a bound state of a charged soliton and a neutral soliton whose midgap energy states hybridize to form bonding and antibonding levels.

Polymer: oligomers with more than ten repetitive units connected by covalent chemical bonds.

Polymorph: polymorphism is the ability of a solid material to exist in more than one form or crystal structure. Polymorphism can potentially be found in any crystalline material including polymers and metals and is related to allotropy which refers to elemental solids.

Quantum efficiency: quantum efficiency in an optical source or detector, is the ratio of the number of output quanta to the number of input quanta.

Semiconductors: are special case of solids intermediate between metals and insulators whose electrical conductivity can be controlled over a wide range, either permanently or dynamically. The conduction band is empty as in the insulator; however the band gap is small enough to allow some thermal or optical excitation. Also, by chemical impurities (doping), free charge carriers are generated.

Singlet: in theoretical physics, a singlet usually refers to a one-dimensional representation (e.g. a particle with vanishing spin). It may also refer to two or more particles prepared in a correlated state, such that the total angular momentum of the state is zero. Singlet frequently occurs in atomic physics as one of the two ways in which the spin of the two electrons can be combined.

Solitons: the soliton is a domain boundary between the two possible degenerate ground state configurations of trans-$(-CH=CH-)_N$. The localized electronic state associated with the soliton is a nonbonding state at an energy which lies at the middle of the π-π^* gap, between bonding and antibonding levels of the perfect chain.

Thermotropic liquid crystal: a liquid is thermotropic if the order of its components is determined or changed by temperatures.

Trap, Trap state: a chemical impurity (either a dopant, e.g. an atom that can bind or donate an electron, or a crystal structure defect) in a semiconductor forms so called trap states. The trap states attracts a charge carrier that is localized at the trap for a limited amount of time.

Triplet: in quantum mechanics, a spin triplet is a set of three quantum states of a system, each with total spin $S = 1$ also known as second excited state of a molecule produced by absorption of light to produce the singlet state, then loss of some energy (fluorescence) to arrive at the longer-lived triplet state The molecule may remain sufficiently long in the triplet state for a second activating light quantum to be effective in producing a second triplet state, obviously at still a higher level of excitation, hence reactivity. Alternatively, it may lose the triplet state energy directly and return to the ground state.

ABSTRACT

Organic semiconductors, such as short-chain oligomers and long-chain polymers, are now a core constituent in numerous organic and organic-inorganic hybrid technologies. Blue-emitting polyfluorenes (PFs) have emerged as especially attractive π conjugated polymers (CP) due to their high luminescence efficiency and excellent electronic properties and thus great prospects for device applications. The performance of devices based on these polymers depends on side chain conformations, overall crystalline structure, and charge transport processes at the microscopic level. This project entails detailed Raman scattering studies and charge transport properties of two side chain substituted PFs: Poly(2,7-[9,9'-bis(2-ethylhexyl)] fluorene) (PF2/6) and Poly(9,9-(di-n,n-octyl) fluorene) (PF8). The structural properties of PFs are extremely sensitive to the choice of functionalizing side chains. PF8 adopts metastable structures that depend upon the thermal history and choice of solvents used in film forming conditions. Raman scattering techniques as a function of thermal cycling are used to monitor the changes in the backbone and side chain morphology of PF8. These studies establish a correlation between the conformational isomers and the side and main chain morphology. Theoretical modeling of the vibrational spectra of single chain oligomers in conjunction with the experimental results demonstrate the incompatibility of the β phase, a low energy emitting chromophore, with the overall crystalline phase in PF8. Further, electroluminescence and photoluminescence measurements from PF-based light-emitting diodes (LEDs) are presented and discussed in terms of the crystalline phases and chain morphologies in the PFs.

Charge carrier injection and transport properties of PF-based LEDs are presented using current-voltage $(I-V)$ characteristic which is modeled by a space-charge-limited conduction (SCLC) for discrete and continuous traps. PF2/6 with a high level of molecular disorder is an exemplary system for the SCLC model with discrete single level shallow traps. Charge transport as a function of sample thickness uncovers the origin of these traps. The thickness dependent SCLC measurements show the influence of both surface and bulk traps on charge transport. Temperature dependence of $I-V$ and dc conductivity measurements suggest thermal assisted variable-range hopping transport instead of band transport in these materials. Charge carrier injection and doping in CPs induce structural deformation with the formation of self-localized excitation states, such as polarons or bipolarons inside the band gap. Raman scattering studies of PF2/6-based LEDs with doping and in the presence of injected and photo-generated charge carriers show increasing backgrounds with asymmetric Briet-Wigner Fano (BWF) line shapes, indicating strong electron-phonon interactions.

CHAPTER 1

Motivation and research objectives

1.1 Introduction

Soft materials are gaining a lot of importance in today's technological applications. For many applications the mechanical properties are more important, while for others (e.g., in the semiconductor industry) the electronic properties are of interest; other applications demand a combination of mechanical and electronic properties. Semiconducting polymers are a class of materials with electrical conductivity in the range of 100 to 10^{-12} $(\text{Ohm cm})^{-1}$.[1] There are at least four major classes of semiconducting polymers: filled polymers, ionically conducting polymers, charge transfer polymers and conjugated conducting polymers. The latter and charge transfer polymers constitute two important subgroups in semiconducting organics, a field initiated by the discovery of electrical conductivity in molecular charge transfer complexes in 1954.[2,3]

The field of semiconducting polymers gained importance since 1977, when it was discovered that chemically doped polyacetylene exhibits several orders of magnitude increase in its electrical conductivity.[4] Semiconducting polymers bring together the virtues of plastics and semiconductors in materials of emerging technological importance and outstanding potential. Their enormous potential comes from the fact that they combine novel semiconducting electronic properties with the scope for easy shaping and processing. The electronic and optical properties of polymers can be tuned quite easily by changing their chemical structure, making them very versatile and procecessable.

Organic molecules have been known to show electroluminescence (EL) since the early 1960s.[5] In the 1980s EL was reported from double layer vacuum-sublimed molecular thin film devices.[6] The discovery of EL from the conjugated polymer poly-phenylene vinylene (PPV) in 1990[7] finally enabled the production of optoelectronic devices using simple coating techniques, which are less expensive compared to vapor deposition of inorganic materials and organic molecules. This has revolutionized the field of optoelectronics, where semiconducting polymers are conceived as a building block for transistors, light-emitting diodes, solar cells, photo-detectors and even lasers.

The use of neutral or undoped conjugated polymers as well as other electroplastics (electroactive polymers with charge transporting properties) as active materials for semiconductor device applications has become the dominant theme in the field of organic materials.[2] Conjugated polymers (CP) like PPV, polyfluorene have been the materials of choice for plastic LEDs because of their processability, relatively high efficiency, and a wide range of color emission for full color display.

1.2 Motivation and research objectives

Since after the initial discovery of EL from PPV by Burrough et al. in 1990,[7] considerable progress has been made in the field of organic electronics. Despite the enormous versatility for optoelectronic applications, some of the fundamental physics underlying the construction or optimization of practical devices based on these polymers remains controversial or poorly understood.

π-CPs have key advantages over their conventional solid-state inorganic counterparts in terms of tunability of the emissive color by structural modifications. Band gap and color tuning of CP by chemical modification and copolymerization offer extensive

research work for high efficient Red-Green-Blue (RGB) LEDs, which constitute the active elements in a new generation of plastic optoelectronic devices.[8,9]

Whilst all three colors have been demonstrated, there are relatively few efficient and high brightness blue emitting polymers. The family of PFs is an extensively studied class of electroluminescent CPs due to their strong blue emission which can be easily down-converted into green and red emission by doping with lower bandgap fluorescent dyes to obtain the full gamut of colors.[10,11] For that reason, developing an efficient and stable blue polymer LED is of foremost interest.

Two members of the PF family: poly[9,9'-(di-n, octyl)fluorene] (PF8) and poly[9,9'-(di 2-ethylhexyl)fluorene] (PF2/6), having optical emission peaked in the blue and high luminescence quantum efficiencies create excellent prospect for blue LEDs and other optoelectronic device applications.[12,13,14]

In PFs there is evidence of local inhomogeneities in the structural order that give rise to heuristic families of conformation isomers with, in sum, both segmental and wormlike disorder.[15] Much current research efforts are directed in understanding the relationships between the side chain moiety and the observed physical properties.[16] There are many ambiguities regarding backbone conformations and side chain structure which control the electronic and optical properties.

At the simplest level, bulky side chain constituents will reduce close packing of the conjugated polymer backbones[17] and thereby diminish the formation of interchain electronic pathways and optical excitations. Vibrational frequencies and intensities determined by Raman spectroscopy are strongly influenced by conformations of the main backbone, their planarity as well as side chain conformations. Application of Raman

scattering is especially useful in PFs for discerning the families of chain conformers and structural phases. In light of the ambiguities in the structure, one of our main focuses in this work has been to study chain morphologies and crystalline structure of PF8 and PF2/6, using temperature-dependent Raman scattering cast from different solvents, and to subsequently understand their impact on LEDs.

In addition to structure, other defect states and disorder impact the charge transport properties that eventually govern the performance of PF-based optoelectronic devices. Efficient charge transport through a polymer chain relies on the conformation and structural phases in the solid state as well as the density of chemical and/or structural defects.

Charge injection, charge transport, and recombination are the three crucial contributions that optimize the device efficiency of a polymer LED.[18] An unbalanced injection results in an excess of one carrier type that does not contribute to light emission, which can rise to confinement of EL emission to a region close to one of the injecting electrodes, where enhancement of nonradiative decay rate is expected and thereby decrease the quantum efficiency substantially.[19]

Charge injection in PF based blue emitting polymers is a topic of heavy debate. Since structural properties of PFs are extremely sensitive to the thermal history and choice of solvents used in film forming conditions, devices fabricated from this polymer will have a significant effect on their charge transport properties and hence device performance.

In order to understand the role of structure and defects on the charge transport of PFs, in the first half of this research we have carried out extensive Raman scattering

studies of PFs. This is then followed by $I-V$ characteristics of PF based diodes to investigate charge transport properties and density of defect levels as well as their distribution.

Charge storage in CPs induces structural deformation which results in the formation of localized excitation states within the band gap. Carrier transport in these materials is typically very low and mainly occurs by variable-range hopping[20] with polarons being the actual carriers.[21] In CPs with a nondegenerate ground state both doubly charged (spinless) bopolarons and singly charged polarons coexist.[22] Doping or injected charges result either in the formation of polarons or bipolarons. The last part of the dissertation focuses on Raman scattering studies from PF2/6-based LED structures in the presence of photoinduced and doped charge carriers in the presence of an external electric field to get an insight into polaronic and bipolaronic absorption.

References:

[1] C.C. Ku and R. Liepins, Electrical properties of polymers: Chemical Principles; Hanser publishers: Munich, (1987).

[2] Bing R. Hsieh, Yen wei, Semiconducting polymers; Applications, Properties, and Synthesis, American Chemical Society (1999).

[3] A.J. Heeger, Reviews of modern physics (Nobel Lectures) Vol. **73** July (2001).

[4] C. K. Chiang, C. R. Fincher, Y. W. Park, A. J. Heeger, H. Shirakawa, E. J. Louis, S. C. Gau, A. G. MacDiarmid, Phys. Rev. Lett., **39**, 1098–1101 (1977).

[5] M. Pope, H. P. Kallmann, P. Magnante. J. Chem. Phys., **38,** 2042 (1963).

[6] C. W. Tang, S. A. VanSlyke, Appl. Phys. Lett., **51**, 913-915 (1987).

[7] J. H. Burroughes, D. D. C. Bradley, A. R. Brown, R. N. Marks, K. Mackay, R. H. Friend, P. L. Burns, A. B. Holmes, Nature, **347,** 539(1990).

[8] E.Z. Faraggi, H. Chayet, G. Cohen, R. Newman, Y. Avny, D. Davidov, Adv Mater.**7**, 742 (1995).

[9] M. Berggren, O. Inganas, G. Gustafsson, M.R. Anderson, T. Hjertberg. O. Wennerstrom, Nature, **372**, 444 (1994).

[10] D. Sainova, T. Miteva, H. G. Nothofer, and U. Scherf , I. Glowacki and J. Ulanski, H. Fujikawa, D. Neher, Appl. Phys. Lett.,**76**, 1810(2000).

[11] Andreas Meisel, Dr. Phil.nat. thesis on "Alignment characterization and application of polyfluorene in polarized Light-emitting –Devices", University of Frankfurt, (2001).

[12] U.Scherf, E. J. W.List, Adv. Mater., **14**, 477(2002).

[13] D. Neher, Macromol. Rapid Commun., **22**, 1366(2001).

[14] M. Leclerc, J. Polym. Sci., Part A, **39**, 2867(2001).

[15] M. Knaapila, R. Stepanyan, M. Torkkeli, B. P. Lyons, T. P.Ikonen, L. Almasy, J. P. Foreman, R. Serimaa, R. Gu¨ntner, U. Scherf, and A. P. Monkman, Phys. Rev. E **71**, 041802 (2005).

[16] M. Grell, D. D. C. Bradley, G. Ungar, J. Hill, K. S. Whitehead, *Macromolecules* , **32**, 5810(1999).

[17] Y. N.Li, G.Vamvounis, S. Holdcroft, *Macromolecules*, **35**, 6900(2002).

[18] W. Paul, M. Blom, Marc J.M., de jong and Coen T.H.F. Liedenbaum, Polym. Adv. Technol., **9**, 390-401 (1998).

[19] N. K. Patel, S. Cinà, and J. H. Burroughes, IEEE, J. QE, **8,** No.2 (2002).

[20] P. E. Parris, V. M. Kenkre and D. H. Dunlap, Phys. Rev. Lett., **87**, 126601 (2001).

[21] M. N. Bussac and L. Zuppiroli, Phys. Rev. B **55**, 15587 (1997).

[22] A.J. Heeger, S. Kivelson, J.R. Schrieffer, and W.P. Su, Rev. Mod. Phys., **60**, 781 (1988).

CHAPTER 2

Semiconducting conjugated polymers

2.1 Introduction

Electrically conducting or semiconducting conjugated polymers (CPs) have attracted an overwhelming interest in laboratories around the globe for the last three decades. These materials may combine the processability and outstanding mechanical characteristics of polymers with tailored electrical, optical and magnetic properties of functional organic molecules. After the discovery of metallic properties in doped polyacetylene in 1977,[1] remarkable progress has been made in synthesizing CPs, in understanding their properties, and in developing them for their use in electronic and optical devices.[2]

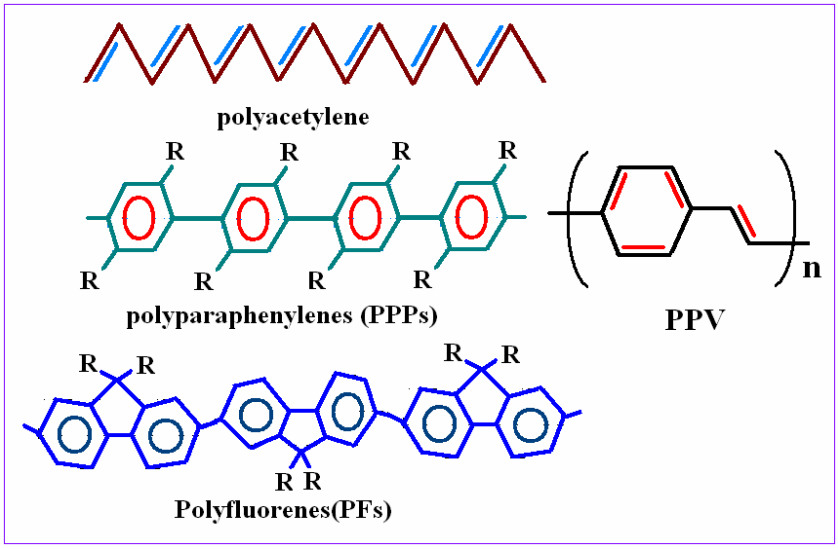

Figure (2.1): Typical long chain organic semiconductors (top to bottom) are polyacetylenes, polyparaphenylenes (PPPs), PPV, and polyfluorenes (PF).

The PPV family of polymers serves as a prototypical class of CP for application as well as for fundamental understanding of electronic process since the discovery of its light emitting properties.[3] Device applications, such as optical switching, solar cells, light-emitting displays, and field effect transistors are a direct consequence of active research since the 1980s.[4]

2.2 π conjugation

In an inorganic solid, semiconductivity is described by the band theory of solids.[5] Within this theory the energetic structure of a solid is defined primarily by the lattice structure. In a crystalline solid, rather than having discrete electron energies, the available energy states form bands. Semiconductors are then materials for which the top of the highest occupied, or valence band is separated from the bottom of the lowest unoccupied, or conduction band by an energy of ~1-3 eV. Organic semiconductors are made up of molecules which consist mainly of carbon and hydrogen atoms, held together by covalent bonds, and the individual molecules are held together by Van der Waals forces.

The molecules in an organic semiconductor can be found arranged in a perfectly regular manner (single-crystal) to completely disorder (amorphous).[6] A special state of condensed matter is liquid crystallinity, being between that of a crystalline solid and an isotropic liquid. Certain organic semiconductors comprised of disk-shaped organic molecules have been found to possess such a state. Semiconducting CPs and oligomers can be described in terms of aggregates. Aggregates are characterized by delocalization of the electronic wave function among two or more chains in both the ground and excited states of weakly interacting polymer chains, having a conjugated π-electron backbone.[7]

Principle of π-conjugation

Most luminescent organic molecules and polymers are π-conjugated compounds, where they have alternating single and double or single and triple bonds throughout the molecule or polymer backbone.[8] Such materials are said to be "conjugated" if it is possible to swap the positions of the single and double bonds and end up with a structure that still satisfies the chemical-bonding requirements for carbon.

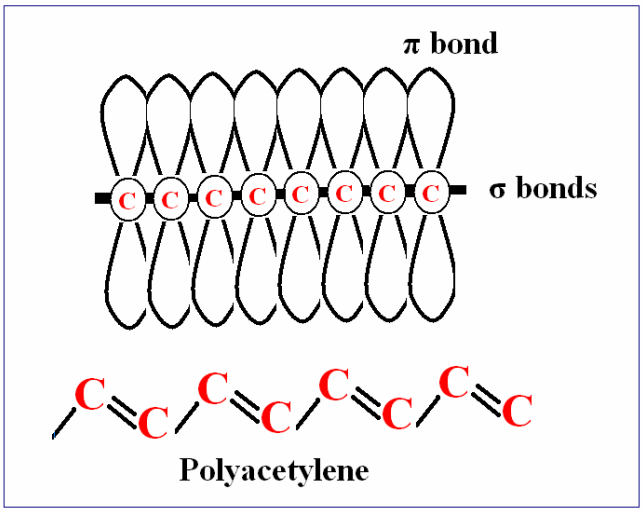

Figure (2.2): Schematic representation of the electronic bonds between carbon atoms (above) in polyacetylene (below).

Let us consider the structurally simplest CP, polyacetylene, which consists of a chain of carbon atoms. The atomic orbitals of the carbon atoms in a CP can be considered as hybridized, meaning that the 2s orbital is linearly combined with the 2p orbitals to form new orbitals. In the case of polyacetylene and most CPs, the 2s orbital mixes with the $2p_x$ and the $2p_y$ orbitals to form three energetically equivalent sp^2 orbitals, located in the corners of an equilateral triangle shown in Fig. 2.4. These are responsible for the so-called σ-bonding to the three neighbors (at least two of which are also carbon atoms). The

fourth electron resides in the unaffected $2p_z$ orbital, which is oriented perpendicular to the molecular plane (Fig. 2.3). The $2p_z$ orbitals of all carbon atoms are linearly combined to form the so-called π molecular orbitals, which are delocalized along the polymer chain and are involved in the transport of charge.

In case of benzene, which is an example of a cyclic conjugated molecule it has six carbon atoms arranged as a hexagon. Each carbon atom forms sp^2 σ bonds with one hydrogen atom and its two adjacent carbon atoms. The π electron now forms a ring orbital above and below the plane of the hexagon. The π electrons are shared equally between the two bonds on either side of each carbon atom.[9]

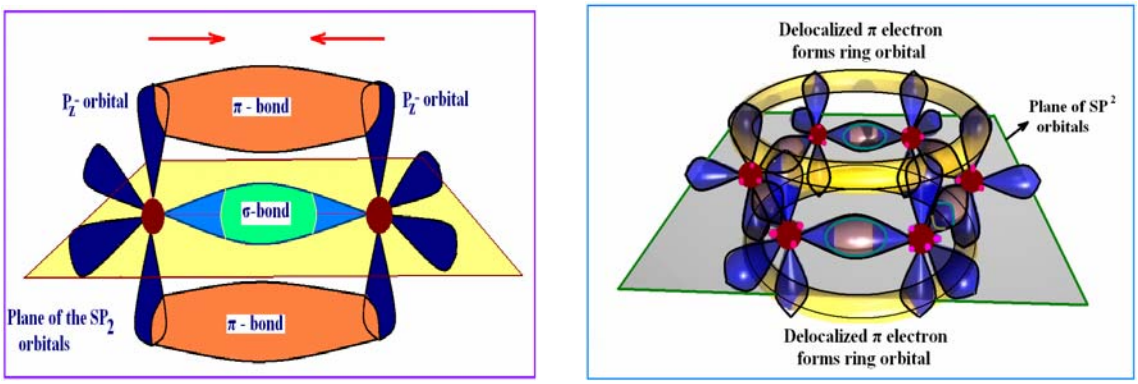

Figure (2.3): (Left) Ethylene molecule. The carbon and hydrogen atoms lie within a plane defined by the σ bonds. (Right) The π electrons of a benzene molecule form a delocalized ring orbital above and below the plane of the hexagon defined by the six carbon atoms.

The polymer chains are not conjugated along the whole chain, but instead they consist of conjugated segments only, since twists and bends in the polymer chain disrupt the π-bonds between different segments of the same polymer chain. The mean length of these conjugated segments is designated as the *conjugation length* of the polymer. The electronic structure of the polymer film is described by a distribution of electronic states

which is produced by the distribution of conjugated lengths and is additionally broadened by disorder in the local arrangement of the polymer chains.[10]

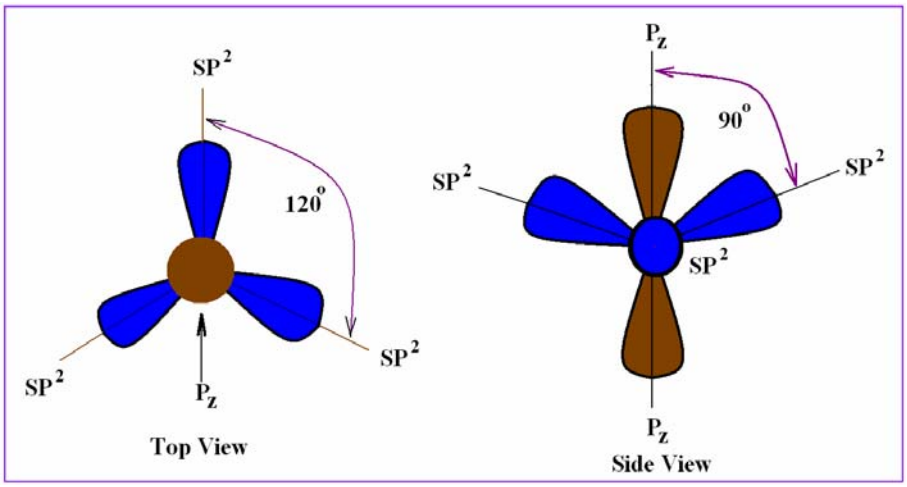

Figure (2.4): sp^2 hybridization.

Typically, CPs are classified into two groups: degenerate ground-state polymers[11,12,13] and nondegenerate ground-state polymers.[14,15] In degenerate ground-state polymers, interchange of single and double bonds on the polymer backbone produces a conjugated chain with identical electronic structure, and gives rise to the possibility of solitonic defects. In nondegenerate ground-state polymers, the interchange of single and double bonds along the polymer backbone yields two states of different energies; i.e., there is no degeneracy in the ground-state energy for the single-double bond interchange transformation, leading to polaron or bipolaron states for charged defects on the polymer.

2.3 Electronic states and transitions in CP

The essential structural characteristic of all CPs is their quasi-infinite π system extending over a large number of recurring monomer units. The lower energy π (or bonding) orbital known as HOMO is similar to the valance band while the higher energy

or excited configuration of the π orbital labeled as π* (or antibonding) orbital (first energy level above the HOMO state) is the LUMO level, similar to the conduction band. In π-CP the bond alternation instability known as the Peierls instability doubles the size of the repeat unit, thereby making CPs semiconducting.[16]

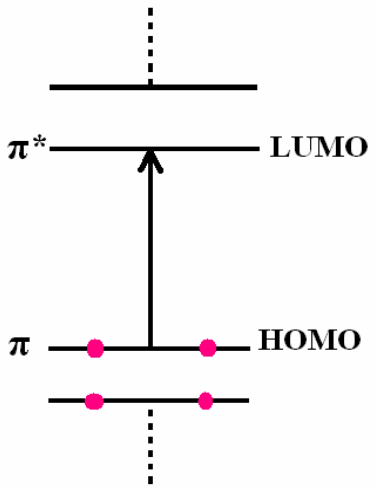

Figure (2.5): Schematic energy diagram for a conjugated molecule

Electronic transitions

Electrons in the ground state of a conjugated molecule and polymer are all paired off in bands with their spins antiparallel. This means that the ground state of HOMO level has a spin quantum number S equal to zero. The excited states, however can either have S=0 or S=1. This is because the excitation process puts an unpaired electron in the excited state and leaves an unpaired electron in the HOMO state.

According to the rules of addition of angular momenta, two spin ½ electrons can combine to give a total spin of either 0 or 1 (Fig. 2.6). The multiplicity of the spin states is equal to (2S+1), because there are (2S+1) degenerate m_s levels in each state. Hence the S=0 states are known as singlets, while the S=1 states are called triplets. Triplets tend to have lower energies than their singlet counterparts and have longer life times.

The separation of the electronic levels into singlet and triplet states has very important consequences on the optical spectra. Each molecule will have a series of singlet excited states labeled S_1, S_2, S_3…., in addition to its singlet ground state which is labeled S_o. There will be a similar series of triplet excited states labeled T_1, T_2, T_3….. Since photons carry no spin, they can excite only transitions between electronic states of the same spin. Therefore, transitions from the S_o ground state to the triplet excited state are not allowed. The main optical absorption edge therefore corresponds to the $S_o \rightarrow S_1$ singlet-singlet transition. The emission spectrum is likewise dominated by the $S_1 \rightarrow S_o$ transition.

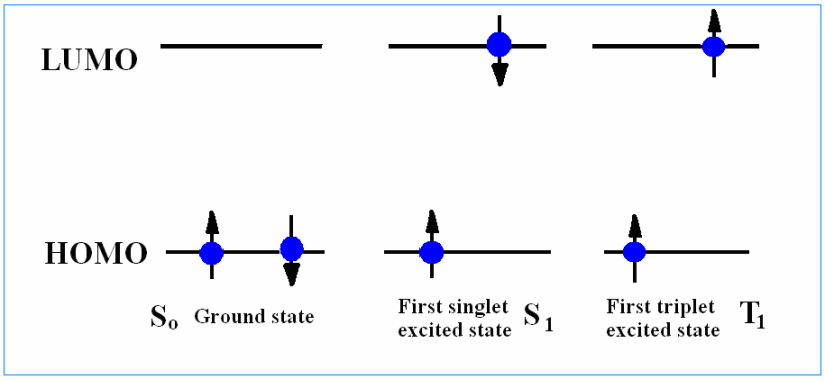

Figure (2.6): The unpaired electrons of an excited molecule can either have their spins antiparallel or parallel are known as singlet and triplet state.

The singlet excited states have short lifetimes of order 1-100 pico sec due to the dipole allowed transitions to the S_o ground state. The lowest triplet state on the other hand, has a long radiative lifetime because of the low probability for the $T_1 \rightarrow S_o$ transition. The different time scales for the singlet-singlet and triplet-singlet transitions are conveniently distinguished by describing the emission process as fluorescence and phosphorescence, respectively.[9]

2.4 Applications of conjugated polymer

The semiconducting polymers, which have been intriguing researchers for the past 20 years, are now poised to enter the market-place. One of the most advanced applications lies in displays, where semiconducting polymers can be used as the active element in LEDs.[3,17,18] Most of the photonic phenomena known in conventional inorganic semiconductors have been observed in recently developed semiconducting polymers. "Plastic" photonic devices are rapidly becoming a reality: high-performance photonic devices fabricated from conjugated polymers have been demonstrated, including diodes,[19] photodiodes,[20,21,22] field-effect transistors,[23,24,25,26] polymer grid triodes,[27] light-emitting electrochemical cells,[28,29] and optocouplers,[30] are all the categories that characterize the field of photonic devices. These polymer-based devices have reached performance levels comparable to or even better than those of their inorganic counterparts. Semiconductor devices consist of a series of layers-electrodes, the active semiconductor material, and insulators. It is further attractive if they can be assembled, as polymers can, in solution.

Semiconducting polymers comprise a unique class of *solid-state* laser materials with emission that spans the entire visible spectrum. Photopumped lasing and light amplification by stimulated emission have been demonstrated in microcavities and waveguides. The observation of optically pumped lasing in undiluted submicron thick films of conjugated polymers offers the promise of constructing laser diodes with such polymers as gain media.[31]

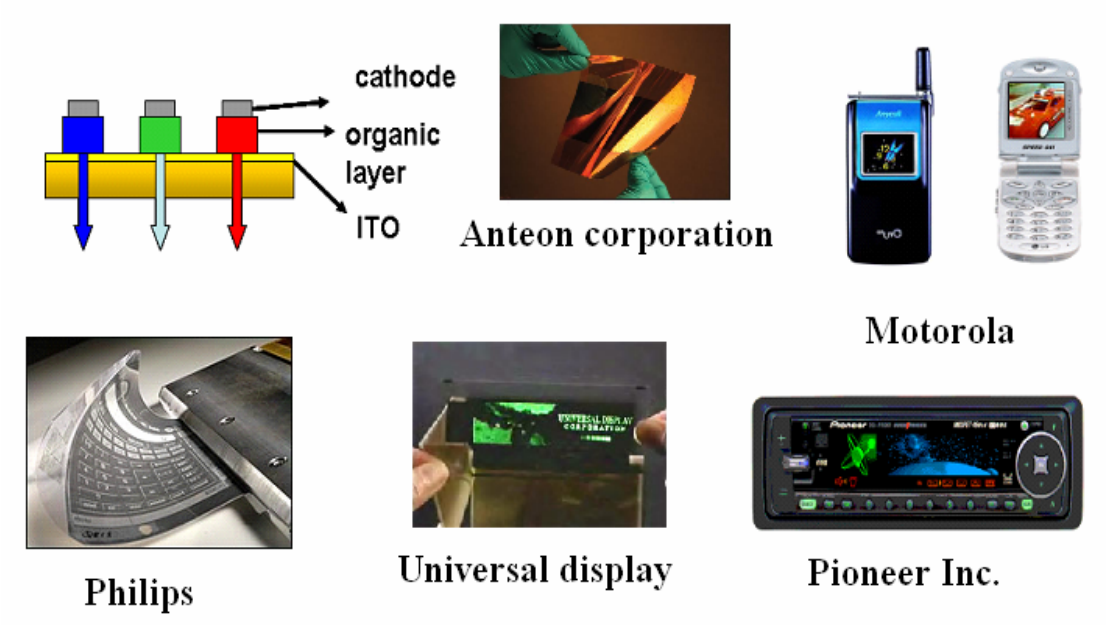

Figure (2.7): A selection of commercially available and future products, in which semiconducting organic moieties are employed.[32]

The advances in printing technology, i.e. high resolution ink-jet printing to fabricate semiconductor devices by processing the conducting polymer from solution has proven to be an enabling step in the development of plastic electronic devices.[33] Many research industries like Philips Research Laboratories have developed "all-polymer" transistors in which every part is made of plastic. Other companies working in these areas include IBM, DuPont, Xerox, plastic logic and Cambridge display technology (CDT). Unlike silicon processors, which are fabricated in flat wafers, Plastic Logic's fabrication process prints the chips on rolls of film that can be applied as smart labels to various surfaces, even clothing.[34] So the future prospect is to provide electronics completely made from plastics, combining their mechanical properties and low production costs of polymeric materials with the electrical properties of semiconductors in one material.

2.5 Polyfluorene and its derivatives

In the development of organic LEDs, blue light emission is of particular importance for a full spectrum of color. Even though a number of fully conjugated and partially conjugated (alternating conjugated and non conjugated segments) polymers have been designed and synthesized in an attempt to realize efficient blue PL and EL, only a limited number of these polymers appear promising for use in blue LEDs.[35]

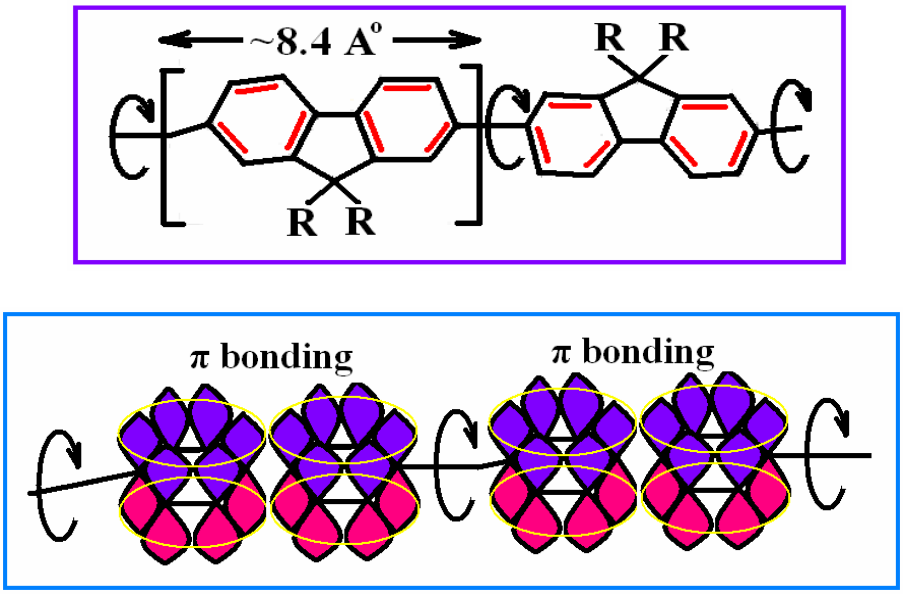

Figure (2.8): (Top) Chemical structure of poly (dialkyle fluorene) and (Bottom) sketch of the P_z orbitals responsible for π conjugation, the sp^3 orbital necessary for σ conjugation.

Polyfluorenes are excellent for blue LED applications and are now becoming a core building block in a myriad of new device technologies. PF, in which only alternating pairs of phenylene rings are fused, represent structural intermediates to PPPs. They are known for their high solid-state quantum efficiencies, good electron mobilities, and exceptional thermal and chemical stability in inert environments.[36]

Polyfluorenes derivatives

PFs belong to the class of rigid-rod polymers where the monomer unit consists of rigid planar biphenyl units, bridged by a carbon atom in position 9 (shown in fig. 2.9) ensuring a high degree of conjugation. This carbon-9 atom may also carry additional substituents to modify the polymer processability and the interchain interactions in films, without significantly altering the electronic structure of the individual chains. PF derivatives depend on suitable substituents at carbon-9 position which enable solubility in common organic solvents as well as the processing of high-quality thin films by spin casting. The thermal stabilities of the homo and copolymers are excellent with decomposition temperatures exceeding 400°C.[37]

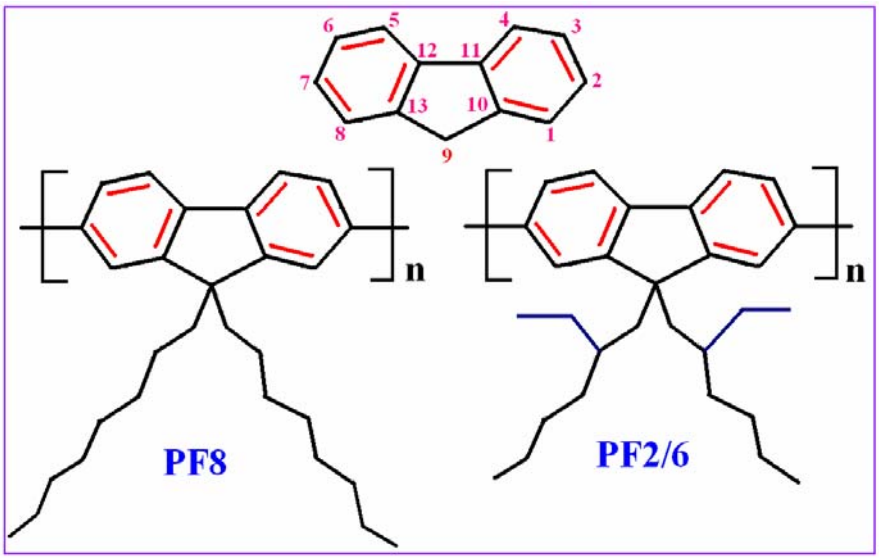

Figure (2.9): Structure of polyfluorene homopolymer with PF8 and PF2/6 structure

In the last few years a large number of oligomer and polymer derivatives have been synthesized. Of these, many recent reports address a relatively select subset of linear and branched dialkyl-substituted fluorenes. Poly[9,9-(di *n*, *n*-alkyl)fluorenes], PF8 (dioctyl),

P6 (dihexyl), and PF2/6 [di(2-ethylhexyl)], have received extra attention because these polymers are mesomorphic, and there are also reports of multiple crystalline phases.[36] All PFs display extremely high fluorescence efficiencies both in solution and in solid state, with emission wavelengths predominantly in the blue region. Their absorption spectra are broad and featureless while PL spectra show well defined vibronic structures. Via copolymerization, the band gap and energy levels can be readily adjusted over the whole visible range.[38]

A great deal of research is directed to understand the relationships between the side chain moiety and the observed physical properties.[39] The side chains can also give rise to a rich array of mesomorphic behavior with the appearance of n-LC phases.[40,41,42] Use of side chains containing chiral centers creates opportunities for optical activity and the emission of circularly polarized light.[43,44] In the next section we discuss the structure and crystalline phases of PF2/6 and PF8 and conformational isomers.

(a) Poly(2,7-[9,9'-bis(2-ethylhexyl)]) fluorine (PF2/6)

Among three closely related PF derivatives, PF2/6 is perhaps most unusual for its peculiar structural properties, i.e., evidence for either a 5/1 or 5/2 helix, and the opportunities for imparting optical activity. Substitution of the ethyl group at the second carbon position of the hexyl side chain is, by construction, a chiral center.[45]

Despite the molecular level disorder, thermally annealed PF2/6 films forms one solid state hexagonal phase. In this phase the individual PF2/6 chains adopt a five-fold helix with coherence lengths exceeding 50 nm[46] and a unit cell incorporates three polymer chains[47] as shown in Fig. 2.10.

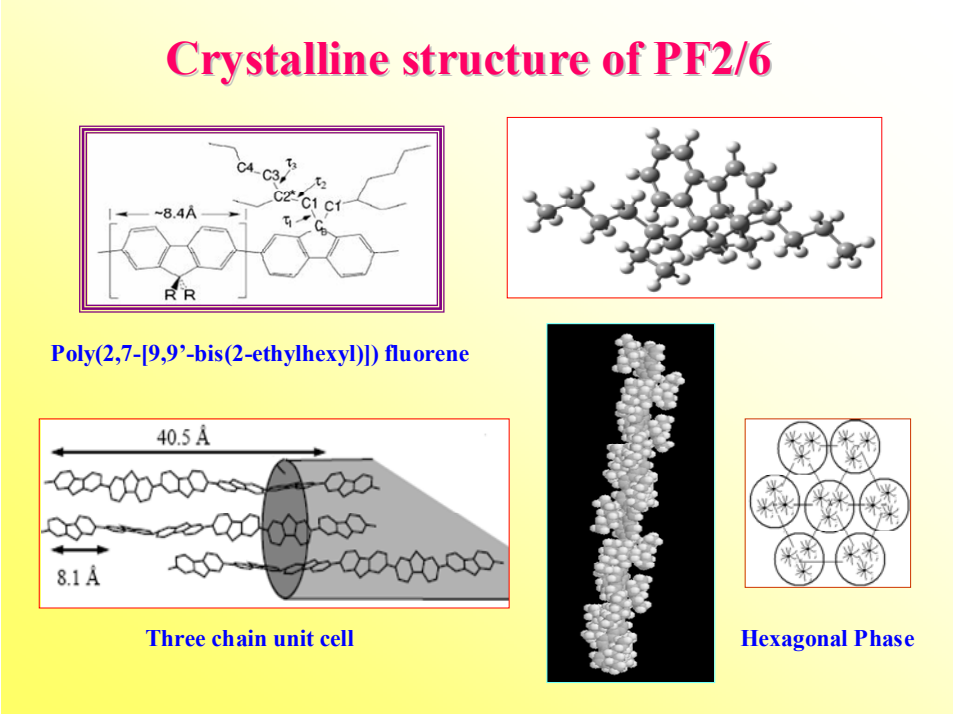

Figure (2.10): PF2/6 and its hexagonal phase.[46]

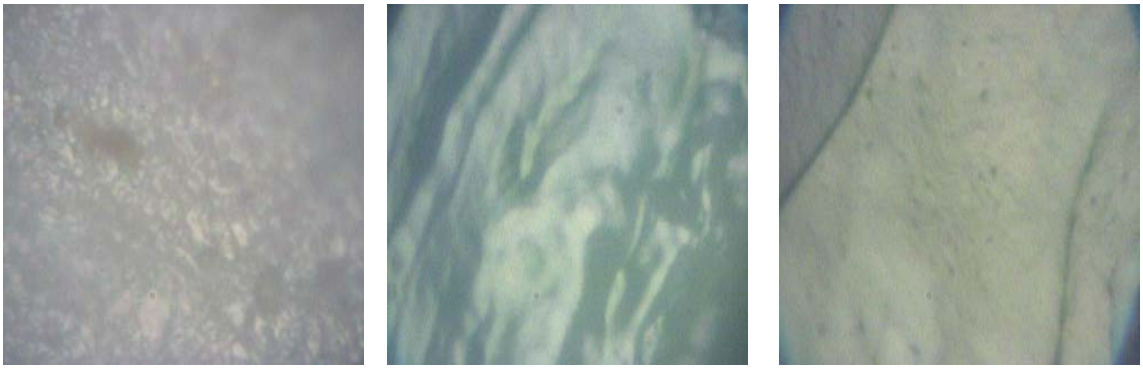

Figure (2.11): Microscopic image of PF2/6 at 25°C, nematic liquid crystal (160-170°C) and after cooling from nematic liquid crystal to room temperature.

(b) Poly(9,9-(di-n,n-octyl) fluorene) PF8

PF8 which has a good solubility and easily accessible transition temperature for LC phase ~174 °C is known for good alignment properties.[48] The absorption of PF8 consists

of a strong featureless π-π* transition that peaks at about 3.2 eV (380 nm) and has a relatively narrow line width (full width at half maximum ~ 0.6 eV).[37]

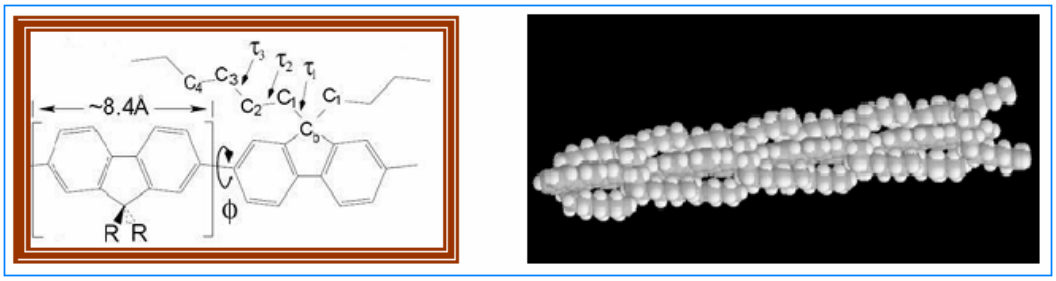

Figure (2.12): Poly(9,9-(di-n,n-octyl) fluorene.

PF8 is metastable and with many backbone conformations, one of them is often referred to as β phase. The β-type conformation is claimed to be more planar and less disordered than the α form. Increased planarity implies reduced interband transition energy, and there is an approximate100 meV redshift in the PL spectra of the β form in comparison with films of a pure α[49] Structural properties of PFs are extremely sensitive to the choice of functionalizing side chains. The metastable structures of PF8 are extremely sensitive to the thermal history and choice of solvents used in film forming conditions.

Structural studies of PF8 have identified at least five crystalline phases, schematically shown in Fig. 2.13. In addition to a nematic-liquid crystal (*n*-LC) mesophase appearing at temperatures above 150°C, two crystalline phases (α and α') have been isolated, which are seen upon cooling from the *n*-LC state at different levels of undercooling.

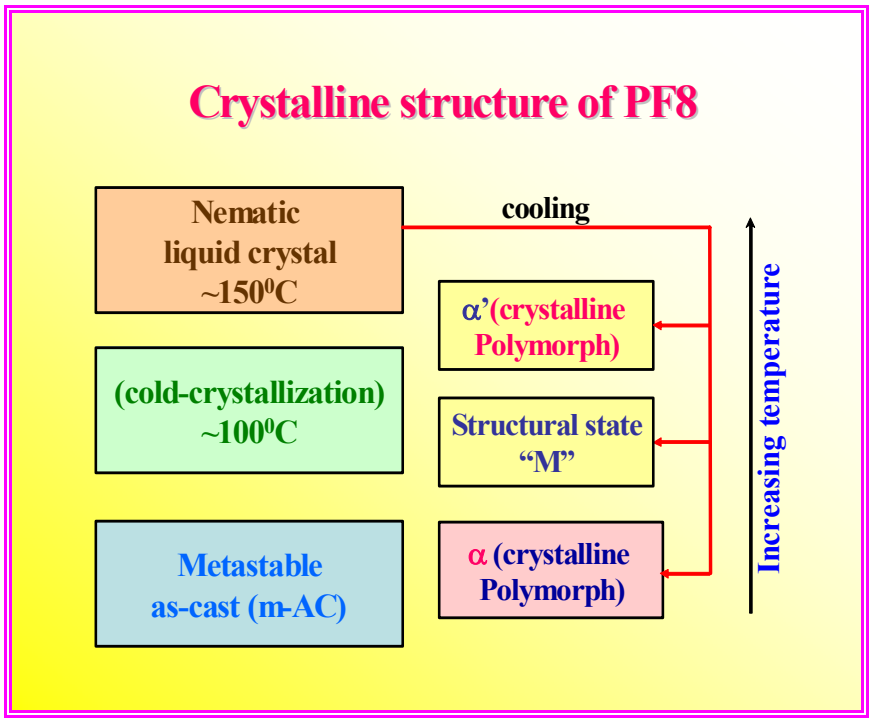

Figure (2.13): Different crystalline phases of PF8

Metastable as-cast (m-AC)

Uniformly appearing phase in PF8 is a metastable structure which can be formed by spin coating or as formed films from solution exist in a metastable disordered state.

K1 (Cold Crystallization)

On mild heating to temperatures just above 100-110^{o}C (m-AC) state undergo cold crystallization to an ordered state K1.

Structural state "M"

In PF8, thermal cycling initiates complex and sample dependent structural evolution. The progression towards the well-ordered α crystal phase is especially variable and, in most

instances, slow cooling from the thermotropic n-LC yields a structural state "M" intermediate between α and α' phases.[50]

Structural form K2

Since the formation of structural phase in PF8 depends on the solvent and thermal cycling, it has been shown that in one case when PF8 powder was obtained by rapid precipitation from MeOH solvent, formation of α crystal is completely suppressed and an alternative structural form can be obtained known as K2.[50]

Nematic Liquid crystal (n-LC)

n-LC also known as nematic glass or nematic mesophase. This phase appears at 150^{o}C or above which is semicrystalline and exist upto 300^{o}C.

Alpha (α) crystalline polymorph

This crystalline phase appears on different levels of undercooling from the n-LC state. In general, rapid thermal quenching from the n-LC phase facilitates transformation to the α crystal phase. It has a large unit cell and large coherence length. The signature of this phase can also be seen by annealing the sample. TEM and XRD observation proposed a structural model of orthorhombic, with a=2.56 nm, b=2.34, c=3.2 nm.[51,52]

Alpha (α') crystalline polymorph

This is the second crystalline polymorph which is similar to alpha phase; in addition it is exceptionally well oriented with respect to the surface normal. This phase is kinetically favored at crystallization temperature of Tc = 130^{o}C. In this phase slight increase in b axis 2.38 (compared to alpha, b=2.34 nm) lowered symmetry along this axis.[52]

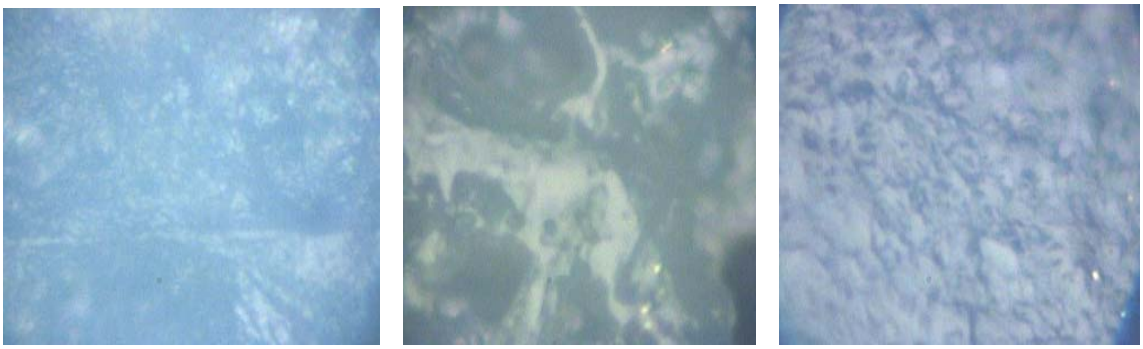

Figure (2.14): Optical microscopic image of PF8 cast from (p-xylene) at 25^{o}C, nematic liquid crystal (160-170^{o}C) and PF8 powder after cooling from nematic liquid crystal.

2.6 Conformational isomers of PF8

From a modeling study of F8 in a gas phase different families of conformational isomers have been identified depending upon the torsional angles between the fluorene monomers, shown by the arrow in Fig. 2.15.[53,54] These isomers are known as C_{α}, C_{β}, and C_{γ} . The C_{β}, conventionally referred to as the β phase, is the more planar form with a torsional angle ~165°. The C_{α} and C_{γ} isomers are associated with torsional angle of 135° and 155°, respectively.

The β phase is one such conformational isomer that represents a more planar backbone conformation and is identified in spectroscopic measurements as a separate long wavelength feature in both optical absorption and emission spectra. Although this phase appears as a minority constituent, it dominates the optical emission.[55,56]

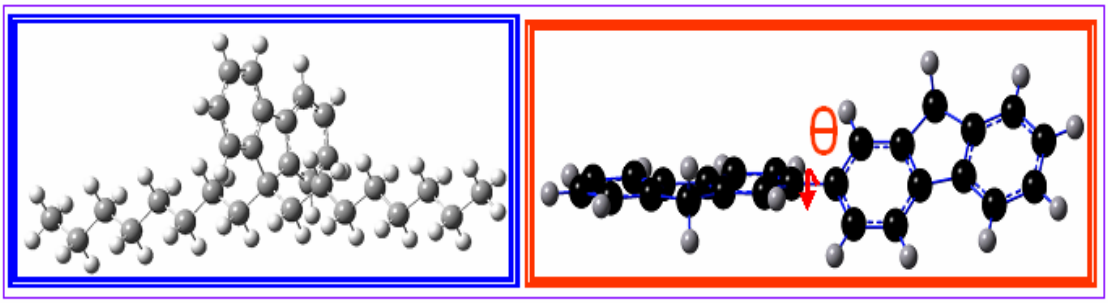

Figure (2.15): (Left) Poly(9,9-(di-n,n-octyl) fluorene) monomer with side chains and (Right) torsional angle between two monomer units.

Beta conformer (C_β): torsional angle ~165°.

Gamma conformer (C_γ): torsional angle ~155°.

Alpha conformer (C_α): torsional angle ~135°.

References:

[1] C. K. Chiang, C. R. Fincher, Jr., Y. W. Park, A. J. Heeger, H. Shirakawa, E. J. Louis, S. C. Gau, A. G. MacDiarmid, Phys. Rev. Lett.,**39**, 1098 (1977).

[2] H. S. Nalwa, Handbook of Organic Conductive Molecules and Polymers, Wiley, New York (1997).

[3] J. H. Burroughes, D. D. C. Bradley, A. R. Brown, R. N. Marks, K. Mackay, R. H. Friend, P. L. Burn, A. B. Holmes. Natur **347,** 539–541 (1990).

[4] William Barford, "Electronic and Optical Properties of Conjugated Polymers", University of Sheffield, UK, Clarendon Press, Oxford, (2005).

[5] Ashcroft and Mermin "Solid state physics" (1976).

[6] B.G. Yacob "Semiconductor Materials: An Introduction to Basic Principles" Springer (2003).

[7] F. Ruini, U. Rossi, E. Hohenester, R.B. Molinari, Capaz, and M.J. Caldas, "Ab-initio study of Coulomb correlated optical properties in conjugated polymers", Synthetic Metals **119**, 257 (2001).

[8] Joseph Shinar, "Organic Light Emitting Devices, A survey", Springer-Verlag New York, Inc. (2004).

[9] Mark Fox, "Optical properties of solids" Oxford University Press Inc. (2001)

[10]Andreas Meisel, thesis on "Alignment, Characterization and Application of Polyfluorene in Polarized Light-Emitting Devices" for Doctor of natural sciences, Solid state physics, Department of Physics of the University of Frankfurt/M. (2001).

[11] A.J. Heeger, S. Kivelson, J.R. Schrieffer, and W.P. Su, Rev.Mod. Phys. **60**, 781 (1988).

[12] K. Fesser, A.R. Bishop, and D.K. Campbell, Phys. Rev. B, **27**, 4804 (1982).

[13] J.L. Bre´das, R.R. Chance, and R. Silbey, Phys. Rev. B, **26**, 5843 (1982).

[14] W.R. Salaneck, R.H. Friend, and J.L. Bre´das, Phys. Rep., **319**, 231 (1999).

[15] J. Hwang and D. B. Tanner, I. Schwendeman and J. R. Reynolds, Physical Review B, **67**, 115205 (2003).

[16] Alan J. Heeger MRS Bulletin, www.mrs.org/publications/bulletin, November (2001).

[17] D. Braun, A. J. Heeger, *Appl. Phys. Lett.,* **58**, 1982-1984 (1991).

[18] G. Gustafson, Y. Cao, Treacy, G. M. Treacy, F. Klavetter, N. Colaneri, A. J. Heeger, *Nature* **357**, 477 (1992).

[19] H. Tomozawa, D. Braun, S. Phillips, A. J. Heeger, H. Kroemer, *Synth. Met.*, **22**, 63 (1987).

[20] G. Yu, A. J. Heeger, *J. Appl. Phys.*, **78**, 4510 (1995).

[21] J. J. M. Halls, C. A. Walsh, E. A. Marseglia, R. H. Friend, S. C. Moratti, A. B. Holmes, *Nature,* **376**, 498 (1995).

[22] G. Yu, J. Gao, J. C. Hummelen, F. Wudl, A. J. Heeger, *Science* , **270**, 1789 (1995).

[23] J. H. Burroughes, C.A. Jones, R. H. Friend, *Nature*, **335**, 137 (1988).

[24] F. Garnier, R. Hajlaoui, A. Yasser, P. Srivastava, *Science*, **265,** 1684 (1994).

[25] A. R. Brown, A. Pomp, C. M. Hart, D. M. de Leeuw, *Science*, **270**, 972 (1995).

[26] L. Torsi, A. Dodabalapur, L. J. Rothberg, A. W. P. Fung, H. E. Katz, *Science* **272**, 1462 (1996).

[27] Y.Yang, A. J. Heeger, *Nature*, **372**, 344 (1994).

[28] Q. Pei, G. Yu, C. Zhang, Y. Yang, A. J. Heeger, *Science*, **269**, 1086(1995).

[29] Q. Pei, Y. Yang, G. Yu, C. Zhang, A. J. Heeger, *J. Am. Chem. Soc.* **118**,3922(1996).

[30] G. Yu, K. Pakbaz, A. J. Heeger, *J. Electron. Mater.* **23**, 925 (1994).

[31] F. Hide, Mariäa Ariäa A. Diäaz-Garciäa, B. J. Schwartz, and A. J. Heeger, Account of Chemical Research, Vol. **30**, No. 10, 430-436 (1997).

[32] Changhee Lee, Presentation on OLED 1, School of Electrical Engineering and Computer science, Seoul national University, South Korea, (2005).

[33] Alan J. Heeger, Synthetic Metals **125**,23-42 (2002).

[34] Jennifer Ouellette, Semiconducting Polymers on Display, American institute of Physics, June/July (2001).

[35] Wang-Lin Yu, Jian Pei, Wei Huang, and A. J. Heeger, Adv. Mater. **12**,825 (2000).

[36] M. J. Winokur, W. Chunwachirasiri, Journal of Polymer Science: Part B: Polymer Physics, Vol. **41**, 2630–2648 (2003).

[37] Dieter Neher, Macromol. Rapid Commun., **22**, 1365-1385 (2001).

[38] Jonathan J. M. Halls, Ana C. Arias, J. D. MacKenzie, W. Wu, M. Inbasekaran, Ed P. Woo, and R. H. Friend Adv. Mater., **12**, No. 7 (2000)

[39] M.Grell, D. D. C. Bradley, G. Ungar, J. Hill, K. S. Whitehead, Macromolecules, **32**, 5810 (1999)**.**

[40] M. J. Winokur,; D. Spiegel,; Y. H. Kim,; S. Hotta,; A. J. Heeger, *Synth. Met.* **28**, C 419 (1989).

[41] M. Grell, D. D. C. Bradley, M. Inbasekaran, G. Ungar, K. S. Whitehead, E. P. Woo; Synthetic Metals, **111**, 579 (2000).

[42] M. Redecker; D. D. C. Bradley, Inbasekaran, M.; Woo, E. P. Appl. Phys. Lett., **74**, 1400 (1999).

[43] M. Oda, H. G. Nothofer, U. Scherf, V. Sunjic, D. Richter, W. Regenstein, D. Neher, *Macromolecules*, **35**, 6792 (2002).

[44] Y.Geng, H. A. Trajkovska, D. Katsis, J. J.Ou, S. W. Culligan, S. H. Chen, J. Am. Chem. Soc., **124**, 8337 (2002)**.**

[45] B. Tanto, S. Guha, C.M. Martin, U. Scherf, and M. J. Winokur, Macromolecules **37**, 9438 (2004).

[46] M. Knaapila, R. Stepanyan, B. P. Lyons, M. Torkkeli, T.P.A. Hase, R. Serimaa, R. Gäuntner, O.H. Seeck U. Scherf, and A. P. Monkman, *Macromolecules,* **38,** 2744 (2005).

[47] G. Lieser, Oda, M. Oda, T. Miteva, A. Meisel, H. G. Nothofer, U. Scherf, *Macromolecules*, **33**, 4490 (2000).

[48] M. Grell, D. D. C. Bradley, M. Inbasekaran, E. P. Woo. Adv. Mat. **9**, 798 (1997).

[49] M. J. Winokur, W. Chunwachirasiri, Journal of Polymer Science: Part B: Polymer Physics, **41**, 2630–2648 (2003).

[50] B. Tanto, S. Guha, M. Arif, and M.J. Winokur, unpublished.

[51] S. H. Chen, A. C. Su, C. H. Su, and S. A. Chen, *Macromolecules*, **38**, 379 (2005).

[52] S.H. Chen, H.L. Chou, and A.C. Su, S.A. Chen, *Macromolecules*, **37**,6833-6838 (2004).

[53] M. J. Winokur, J. Slinker, and D. L. Huber, Phys. Rev. B, **67**, 184106 (2003).

[54] W. Chunwaschirasiri, B. Tanto, D. L. Huber, and M. J. Winokur, Phys. Rev. Lett., **94**, 107402 (2005).

[55] M. Grell, D. D. C. Bradley, G. Ungar, J. Hill, and K. S. Whitehead, *Macromolecules*, **32**, 5810 (1999).

[56] A. J. Cadby, P.A. Lane, H. Mellor, S. J. Martin, M. Grell,C. Giebeler, D.D.C. Bradley, M. Wohlgenannt, C. An, and Z.V. Vardeny, Phys. Rev. B, **62**, 15 604 (2000).

CHAPTER 3

Experimental Techniques

3.1 Overview of optical characterization techniques

3.1.1 Absorption

The process of absorption is caused by the onset of optical transitions across the fundamental band gap of the material. When electrons are excited between the bands of a solid by making optical transitions that are dictated by selection rules it is called interband absorption.[1]

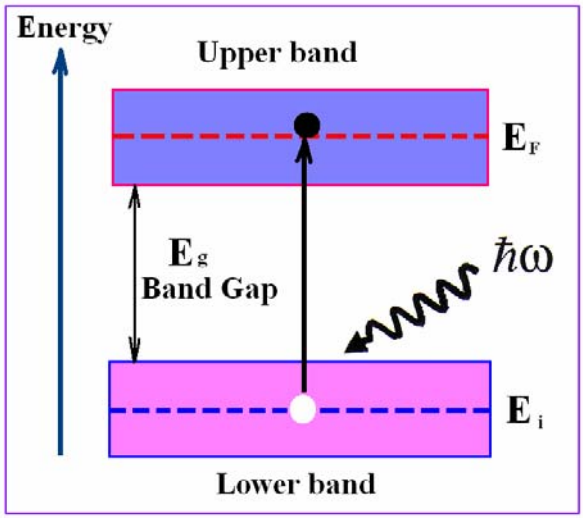

Figure (3.1): Interband optical absoption between an initial state of energy E_i in an occupied lower band and a final state at an energy E_f in an empty upper band. The energy difference between the two bands is the band gap.[2]

Experimental setup of absorption

An absorption spectrophotometer is an instrument that measures the amount of optical absorption in a material, as a function of wavelength. There are four main components of a spectrophotometer: (1) a light source which is usually a tungsten-filament or gas-discharge lamp. Different light sources are used in different regions of the spectrum. (2) a monochromator ; the input to the monochromator is the broadband light from the light source; the output is tunable and highly monochromatic light. (3) a sample chamber which holds the sample under investigation, and (4) a detector which measures the amount of light that passes through the sample. Typically, detectors are either solid-state photodiodes (silicon, germanium, etc.) or photomultiplier tubes. The basic setup for measuring the absorption or transmission of light through a sample is shown in Fig. 3.2.

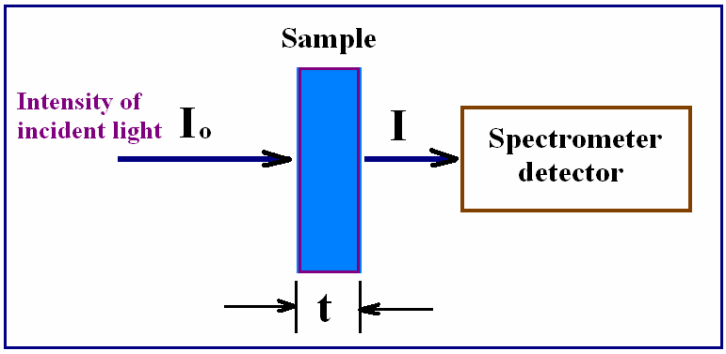

Figure (3.2): Light of intensity I_o incident upon a sample of thickness t undergoes a loss in intensity upon passing through the sample. The intensity measured after passing through the sample is I.

When light of some wavelength λ with intensity I_o passes through the sample the intensity of the light is reduced to a value I, due to absorption within the sample and reflection at the surfaces of the sample. Measuring I_o and I can be used to determine the

transmission of the sample at wavelength λ. In addition to transmission, another useful way to report the optical absorption is in optical absorbance or optical density. Absorbance (A) is a dimensionless quantity defined as the negative of the base-ten logarithm of the transmission (T) $A = -\log_{10} T$. Another quantity of interest is the absorption coefficient (α). The absorption coefficient is given by Beer's Law which relates I to I_o by $I = I_o e^{-\alpha t}$ where "t" is the thickness in cm and consequently, absorption coefficient α is in cm^{-1}. As the absorbance is the negative base-ten logarithm of the transmission then $\alpha = 2.303A/t$. Absorption spectrometers measure the intensity of the transmitted light as a function of wavelength and compare it to the intensity of the reference at the same wavelength.[1, 2]

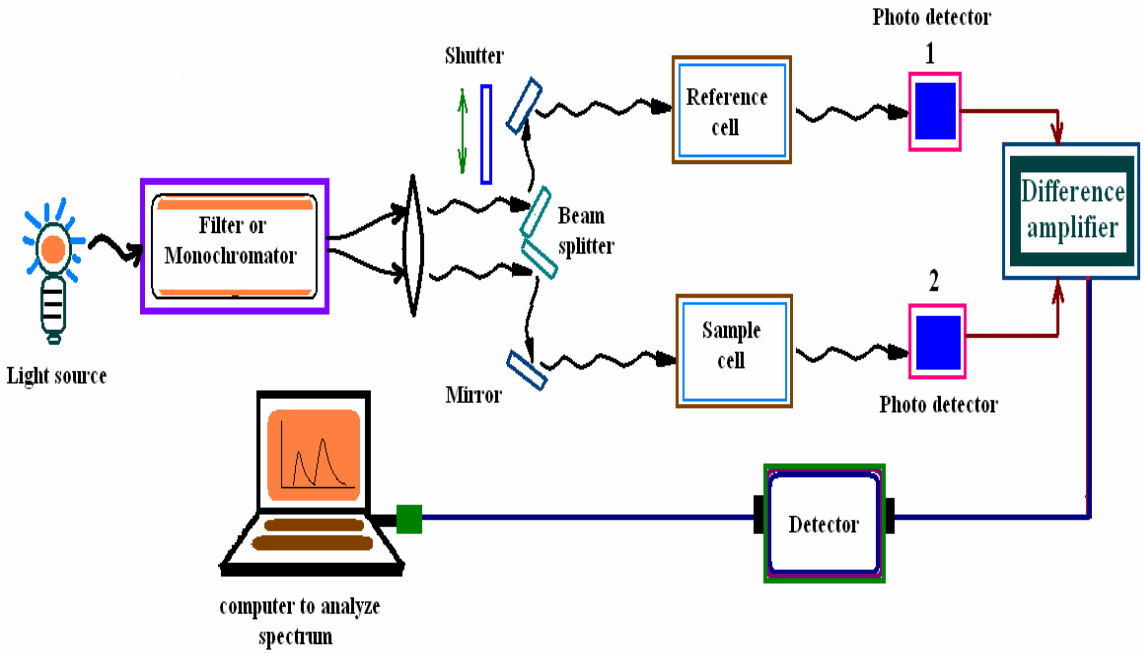

Figure (3.3): Schematic of double beam UV-Visible spectrometer to measure absorption spectra in the wave length range of 200-900 nm.

For the experimental absorption spectra measurements of PFs, thin films were prepared by spin coating from toluene solution on to a sapphire substrate. The ultraviolet visible spectra (UV-Visible) absorption spectra were measured on a Shimadzu UV 2401 PC UV visible recording spectrometer. The schematic is shown in Fig. 3.3.

3.1.2 Photoluminescence

When light of sufficient energy is incident on a material, photons are absorbed and electronic excitations are created. Photo-excitation causes electrons within the material to move into permissible excited states. When these electrons return to their equilibrium states, the excess energy is released by emission of light (a radiative process) or via a nonradiative process. If radiative relaxation occurs, the emitted light is called photoluminescence (PL). The energy of the emitted light is related to the difference in energy levels between the two electron states involved in the transition between the emitted states and excited states.

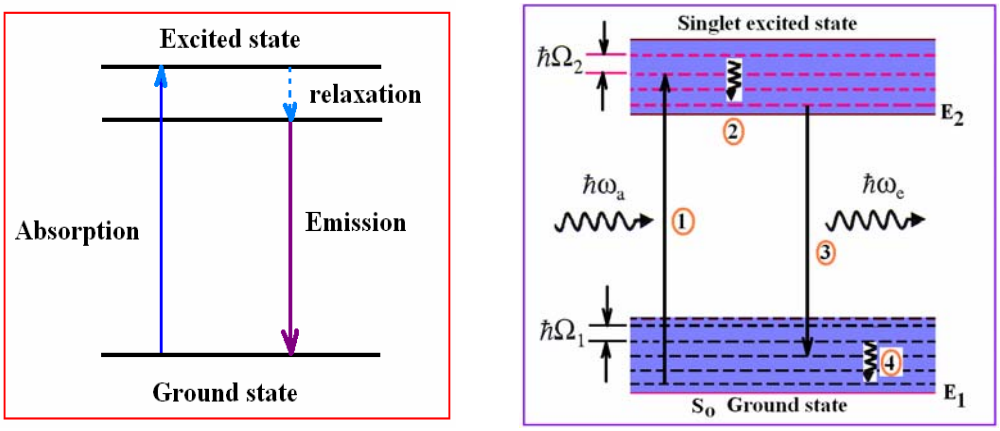

Figure (3.4): (Left) Luminescence process and (Right) schematic diagram of the vibrational electronic transitions in a molecule between the ground state and an excited state (1) absoption (2) non-radiative relaxation (3) emission (4) non-radiative relaxation.[2]

Typical experimental setup of PL

PL is simple, versatile, and nondestructive. The instrumentation that is required for ordinary PL work is modest: an optical source (laser), mirror, collection lenses, optical power meter or spectrophotometer, and a photodetector. A typical PL set-up is shown in Fig.3.5.

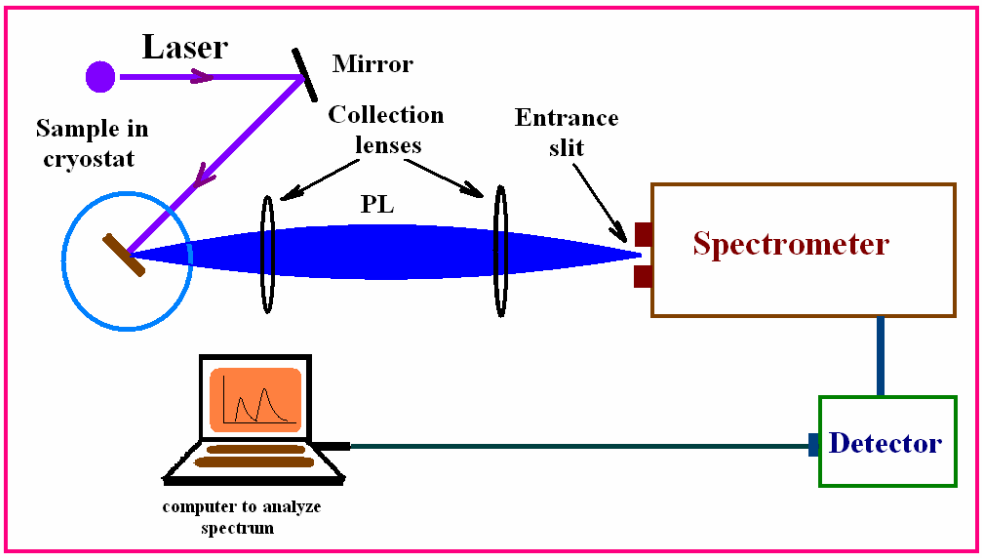

Figure (3.5): Typical schematic diagram and experimental setup for PL measurements.

Our PL measurements of PF thin films were prepared by spin coating from toluene solution. The UV line of an Ar+ (argon ion) was used in our experiment. There are three lines of wavelength in UV laser 351.4 nm, 351.1 nm, and 363.8 nm respectively. An external prism was used to separate lines. Neutral density filters were used to reduce the intensity of the laser line to avoid heating the sample. The emission spectra were collected using a miniature flexible fiber optic spectrometer USB 2000 detector. For some measurements the 325 nm line of HeCd laser was also used as the excitation source. The schematic of our PL system is shown in Fig. 3.6.

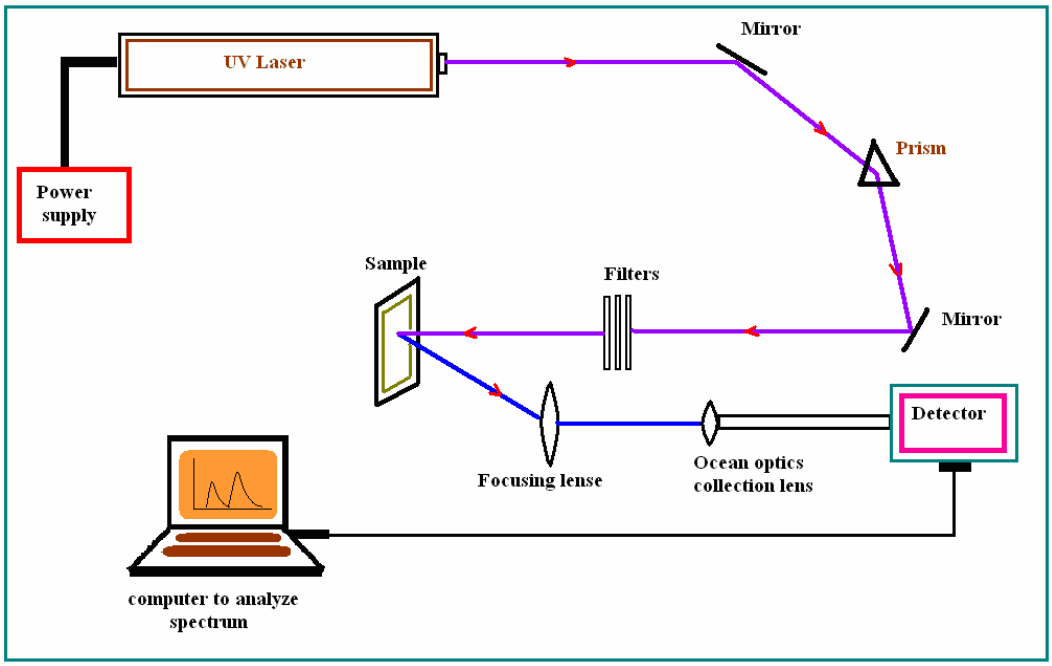

Figure (3.6): Schematic of the experimental arrangement used for the observation of photoluminescence spectra of PF and PF-based LED.

3.1.3 Raman Scattering

The inelastic scattering of light was first predicted in 1923 by Smekal. However, it was not until 1928 that Sir C.V. Raman did the first set of experiments that confirmed Smekal's prediction and led to the Nobel Prize in 1930. The early experiments consisted of irradiating a number of liquids and gasses with the ultraviolet radiation from sunlight.[3] Unlike Rayleigh scattering, which corresponds to the elastic scattering of light, Raman scattering is an inelastic process caused by quasiexcitations. These excitations, for example, can be vibrational modes in a molecule, phonons in a crystal, plasmons, or magnons.[4]

When monochromatic radiation of a certain wave length is incident on systems like dust-free, transparent gases and liquids, or optically perfect transparent solid some of the light is transmitted, some absorbed, but a majority of the light is scattered. Most of the light is elastically scattered. This scattering is called Rayleigh scattering. However, a small fraction of the light (~1 in 10^7 photons) will be inelastically scattered at frequencies different from the incident photons.

The energy difference between the incident and scattered light or the shift in frequency of the light is due to the interaction of the photons with the vibration and rotation of the molecules in the material being studied. The inelastic scattered light makes up the Raman spectrum. Since this is a very small portion of the total scattered light, precise instruments are needed to detect it.

A virtual transition can occur for a photon whose energy is below the ground-to-first excited- state gap (Fig. 3.7). A strong light source can produce a distorted (perturbed) excited state due to the change in the potential caused by the external electromagnetic field, represented as a virtual superposition of the free molecular states. Raman scattering consists of a dipole transition from the ground state to this new state, followed by a transition back down to another ground state with different rotational and vibrational energy. The process is "virtual" because the two transitions are not directly observed. Both stokes and anti-stokes process occur simultaneously in Raman scattering; only their intensities are different.

If the interaction of incident photon shifts the frequency of the scattered photon to a higher frequency, corresponding to a lower final energy an energy equal to $\nabla(\omega_{incident} - \omega_{scattered})$ given to the scattering medium then it is an anti-stokes process, if it is shifted

to a lower frequency or higher final energy it is called a stokes process. Fig. 3.8 shows the difference between elastic (Rayleigh) and inelastic scattering with stokes and anti-stokes processes.

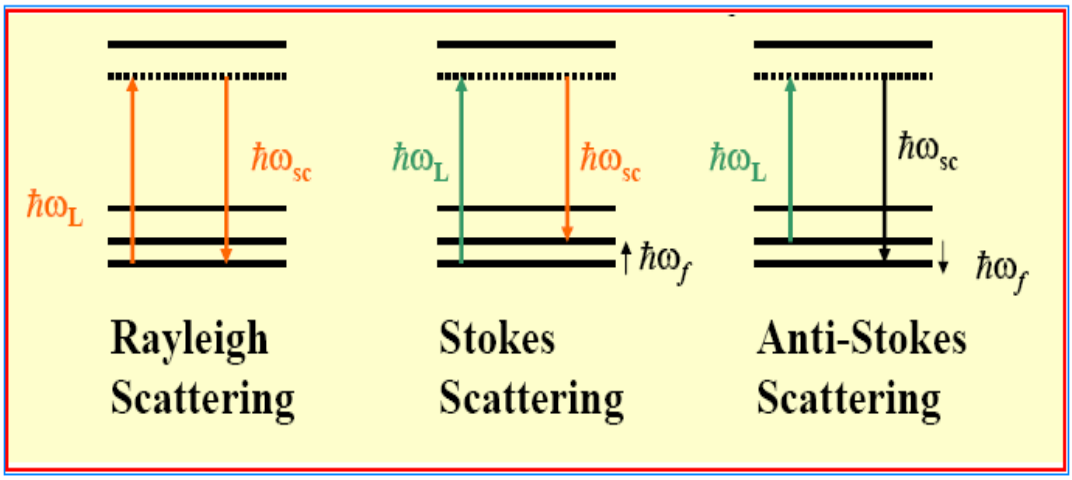

Figure (3.7): Elastic (Rayleigh) and Inelastic scattering with stokes and anti stokes process.

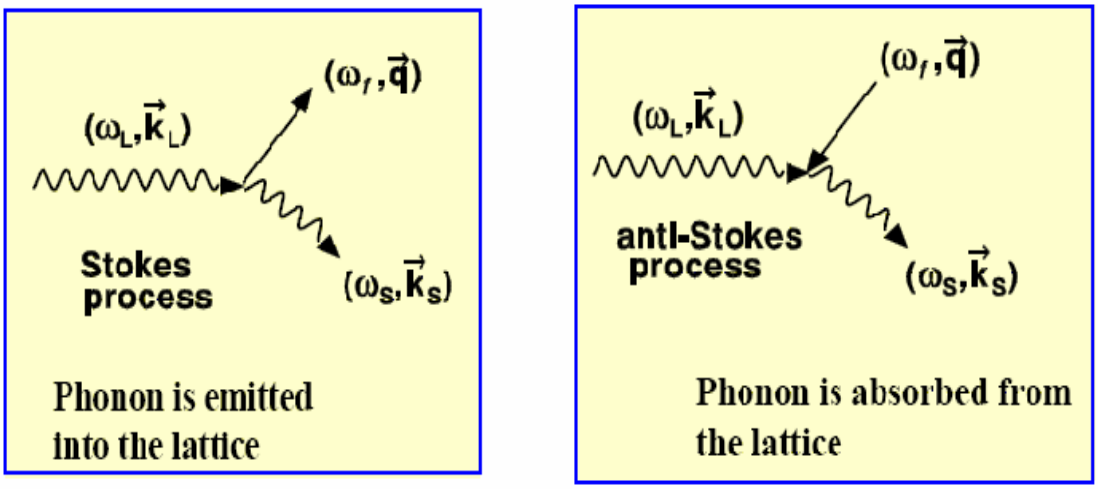

Figure (3.8): Schematic diagram for first-order Stokes and anti-Stokes process.

Experimental setup

The Raman study of materials requires the following components (1) an excitation source, generally a continuous wave (CW) laser; (2) a means of shining the light on the sample such as microscope or collimated optics (3) collection optics to collect the Raman scattered photons; (4) a monochromator to separate the Raman signal into its constituent wavelengths; (5) a detector to detect the scattered photons and (6) a computer system to store and display the spectra.

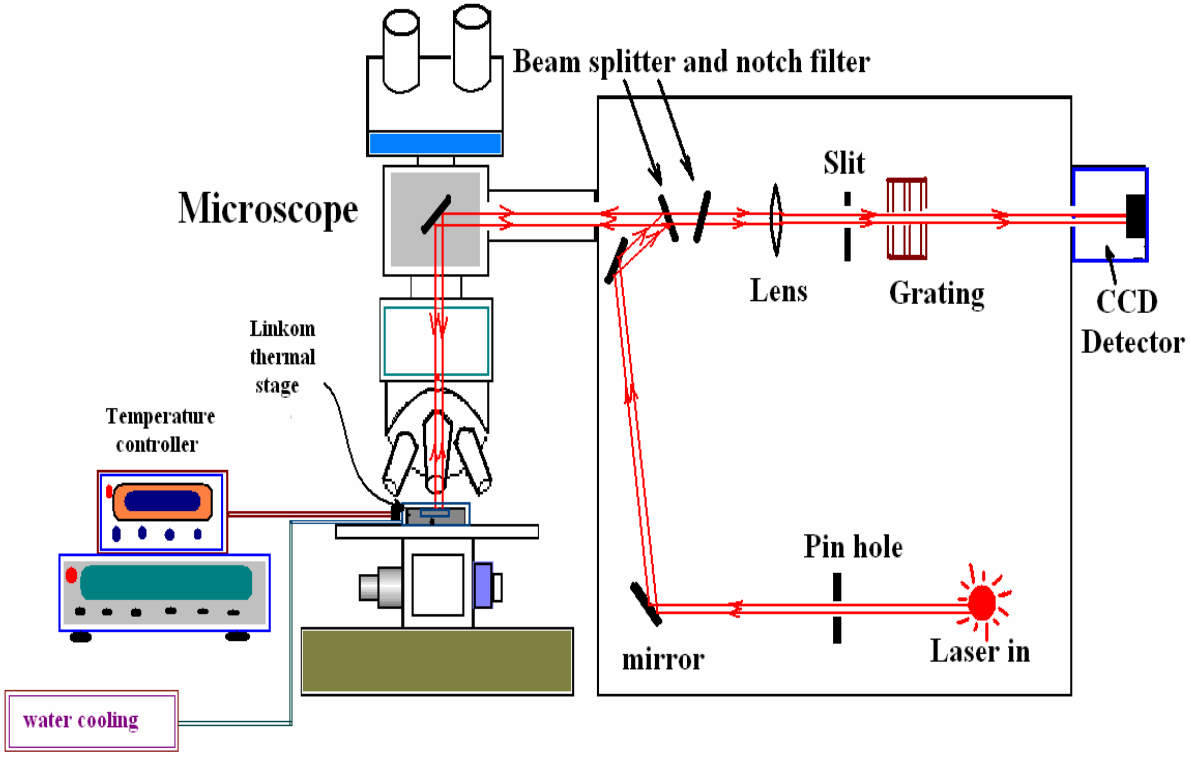

Figure (3.9): Schematic of the micro Raman setup.

In modern Raman spectrometers, lasers are used as a photon source due to their highly monochromatic nature, and high beam fluxes. This is necessary as the Raman effect is weak. In the visible spectral range, Raman spectrometers use notch filters to cut

out the signal from a very narrow range centred on the frequency corresponding to the laser radiation.

Our experimental setup for Raman scattering is an Invia Renishaw spectrometer which is attached to a confocal microscope to obtain high spatial resolution with different objective lenses to illuminate the sample. The schematic of the Raman setup is shown in Fig. 3.9. It utilizes the 785 nm line of a diode laser as the excitation wavelength and collects the Raman scattered light in backscattered (180^{o}) geometry. The system is equipped with two notch filter and charge-coupled-device (CCD). The notch filter separates the inelastic component from the elastic (Raleigh scattering) component. The automatic x-y-z stage attached with the microscope helps to change the position of the spot in the sample and is capable of point by point mapping.

For the temperature dependent Raman scattering setup the samples were affixed to a stainless steel sample holder of a Linkam LTS350 microscope hot-cold stage shown in (Fig. 3.10) with a temperature controller TMS 94. The temperature can be from 196^{o}C to 350^{o}C.

Figure (3.10): Linkam LTS 350 temperature stage and the temperature controller.[5]

3.2 Glove box system for OLED fabrication

Since the device properties of diodes based on organic compounds are extremely sensitive to the environmental conditions, in particular to the presence of oxygen and moisture, this sensitivity of organic semiconductors towards exposition to oxygen and moisture is a strong limiting factor in the operation of semiconductor elements. Special measures need to be taken during preparation and further treatment of the manufactured devices. We use an M-Braun glove-box system for the fabrication of our devices to ensure oxygen and moisture free environment. The system consists of two interconnected glove-boxes filled with dry nitrogen gas (Fig. 3.11)

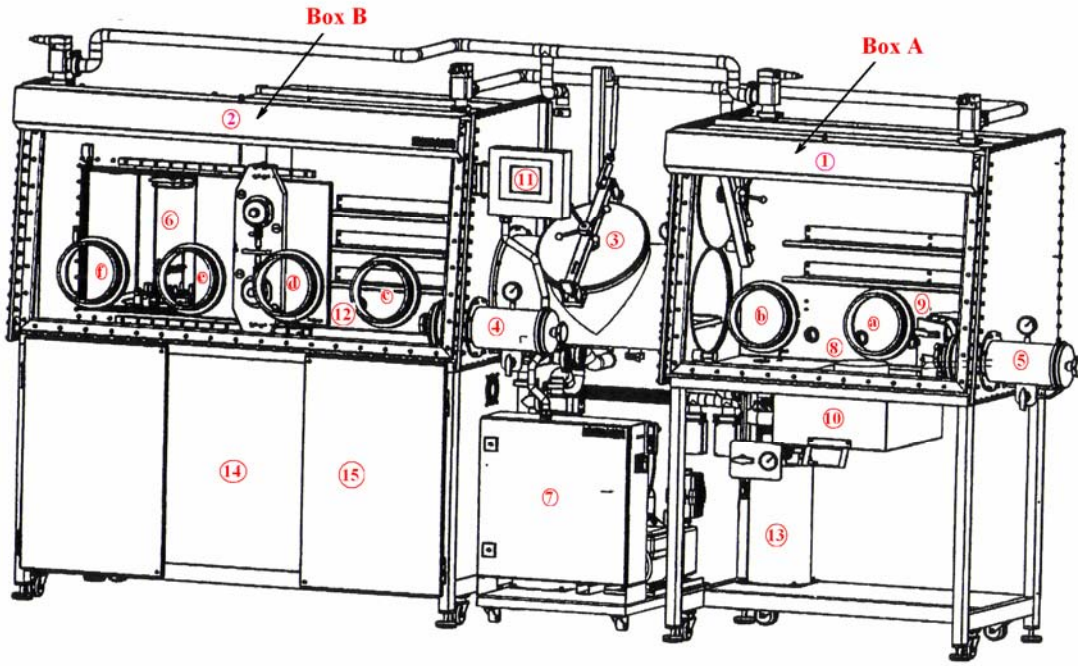

Figure (3.11): Glove box system for the preparation of PF based OLED (1) Box A, (2) Box B, (3) Rail system antechamber (4),(5) small ante- chamber (6) Thermal evaporator (7) Controller for the mini oven (8) Sin coater (9) Mini oven (10) Spin coater controller (11) Touch panel to control the whole system (12) UV light source to cure encapsulation

(13) Solvent trap (14),(15) Power supply and electrical connections and (a),(b),(c),(d),(e),(f) gloves position.

One glove-box (Box A) is fitted with a spin coater and a mini oven, used for spin coating the polymer and baking the film respectively. The other glove box (Box B) is equipped with a thermal evaporator for the deposition of small organic molecules and metals. The two boxes are connected via a T-anti chamber with translation rails and a loading gate.

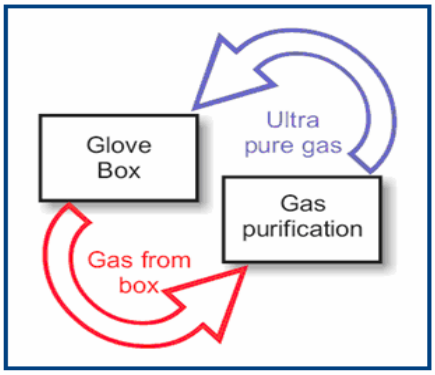

Figure (3.12): Gas circulation process in the glove box.

The glove-box system includes a gas purifier based on a copper catalyst and molecular sieves with closed gas circulation. The wet processing box A contained a purification system that is separated from the other box, protecting the latter from solvent contamination.

Box B also shares the purification system that either allowed independent gas circulation in the two boxes or parallel flow. The water and oxygen content is measured by a H_2O/O_2 analyzer and is typically below 1 ppm for both boxes. The preparation box A, is exclusively used for wet processing of polyfluorenes, using organic solvent such as toluene and *p*-xylene. The glove-box has its own small anti-chamber in order to keep the

T-antichamber protected from solvent contamination and excess materials from outside atmosphere.

The box A is operated in a purification operation mode, where the gas circulation in the box was connected via a charcoal-trap to the glove-box. By permanently removing the polluted nitrogen gas with the protection pump, the used solvent was captured in the trap. Simultaneously the box is refilled with dry nitrogen. In the purifier mode, the nitrogen gas is cleaned from solvent vapors by an activated charcoal solvent trap (MB LMF-I) that preceded the purification system.

Figure (3.13): MBraun Glove box system with box A and box B.

Box A is equipped with a Direct 1000 spin-coater and a small water cooled oven that goes upto 350^{o}C for baking and heat treatment. The spin-coater is inserted in the bottom plate of the glove-box. The accompanying vacuum pump and the controller of the spin-coater were situated outside of the box, ensuring easy handling.

In the metal evaporator (Fig. 3.14), a vacuum of 10^{-6} mbar may be achieved by using a turbo pump. Venting was initiated by an automatic venting mode with time delay, in order to protect the turbo pump. Subsequently, the evaporation chamber is filled with dry nitrogen gas out of the glove-box. This mode of operation allowed us to deposit even reactive metals such as calcium without any protection layer of a non-reactive metal.

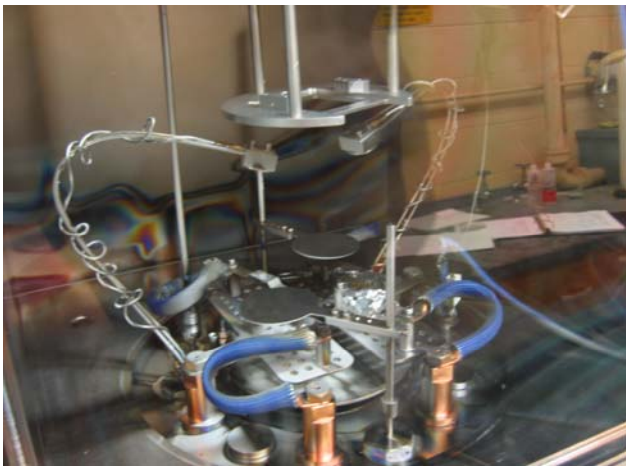

Figure (3.14): Thermal evaporator system with four boats and two shutters and a sample holder on the top.

The metal evaporation system included four evaporation boats as sources located at the bottom of the chamber supported by two automatic/manual shutter for loading the source material. Tungsten and molybdenum boats were employed, depending on the metal to be deposited. Above the four sources, the sample holder was positioned, which could support six samples with the typical size of 1in.x1 in. Just below the sample holder, two quartz balance sensors allow on-line measurement of the evaporation rate and thickness by an externally situated deposition monitor controller (SQC 222 Sigma Co-Deposition). In order to establish a proper deposition rate the quartz balance was situated above the shutters. A UV lamp was also placed in box B to cure the final device structure

after encapsulation with an epoxy to protect further oxidation for exsitu optical and electrical characterization.

3.3 Electrical characterization technique

Electrical properties characterization techniques include direct current (DC) current-voltage ($I-V$), capacitance-voltage ($C-V$), electroluminescence (EL), measurements, resistivity measurements etc. In this work we discuss EL measurement and $I-V$ characterization techniques to study the emission spectra, defects and charge transport in PF based OLEDs.

3.3.1 Electroluminescence

Setup and measurement

The experimental setup of EL measurements include a probe station, Keithly 236 source meter, an Ocean optics USB 2000 spectrometer and a computer with Ocean optics software to collect and analyze the data. The voltage was applied from the source meter to the LED sample through the probe station. The flexible fiber cable of the Ocean optics spectrometer coupled with a CCD detector was setup underneath the OLED device to collect the output light. The spectrometer and the source meter were connected to the computer with a GPIB and a USB connector. Fig. 3.15 shows the schematic of our experimental setup.

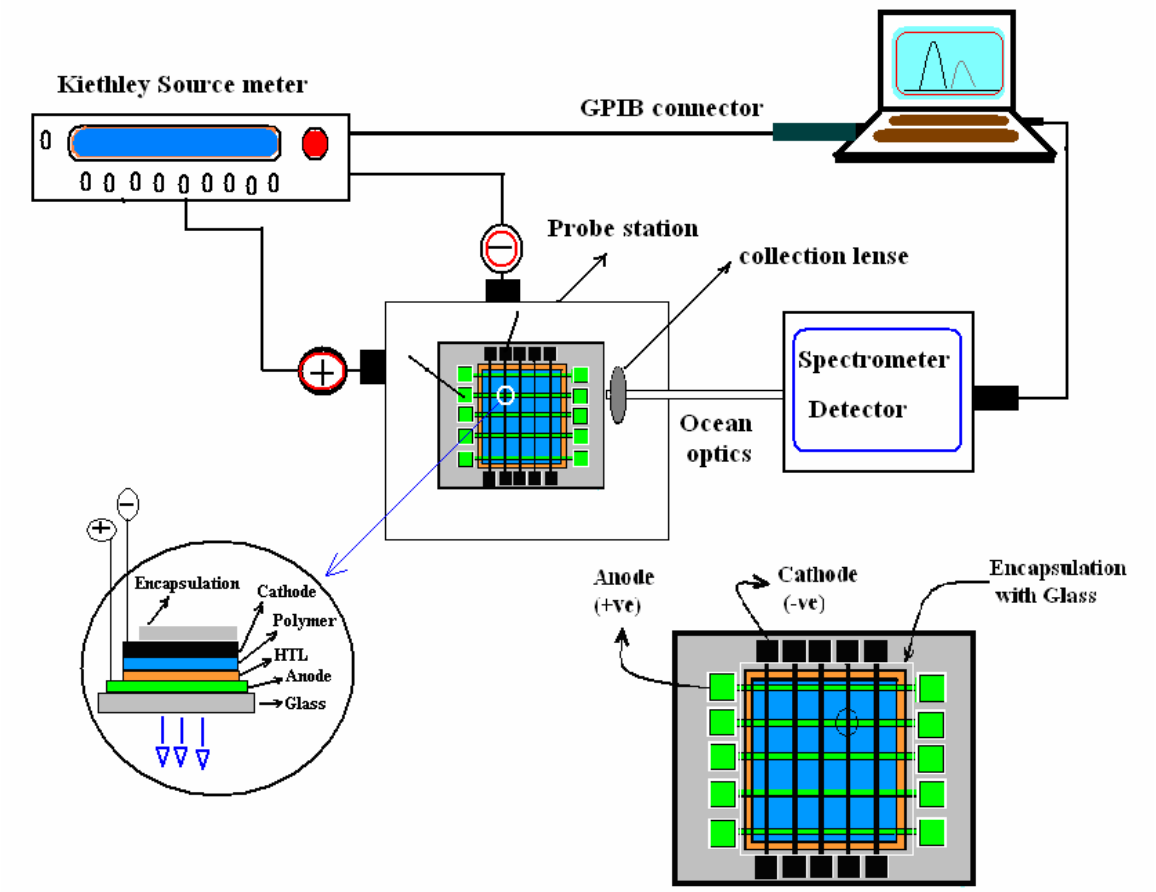

Figure (3.15): Schematic of EL measurements setup for polyfluorene-based light emitting diode.

3.3.2 I-V characterization

In order to characterize a LED's nonlinear behavior, it is desirable to measure the $I-V$ relation, which can give information about the turn on voltage of the device as well as defect states and transport properties of the sample.

For electrical property measurements, using $I-V$ technique it is necessary to make provisions for electrical contact which requires: (1) probe station with needles and sometimes with a microscope attached, to probe very small devices, (2) a source meter to apply voltage and measure current or vice versa, (3) a computer with appropriate

program to collect data and analyze them. Figure 3.16 shows a schematic of our $I-V$ setup.

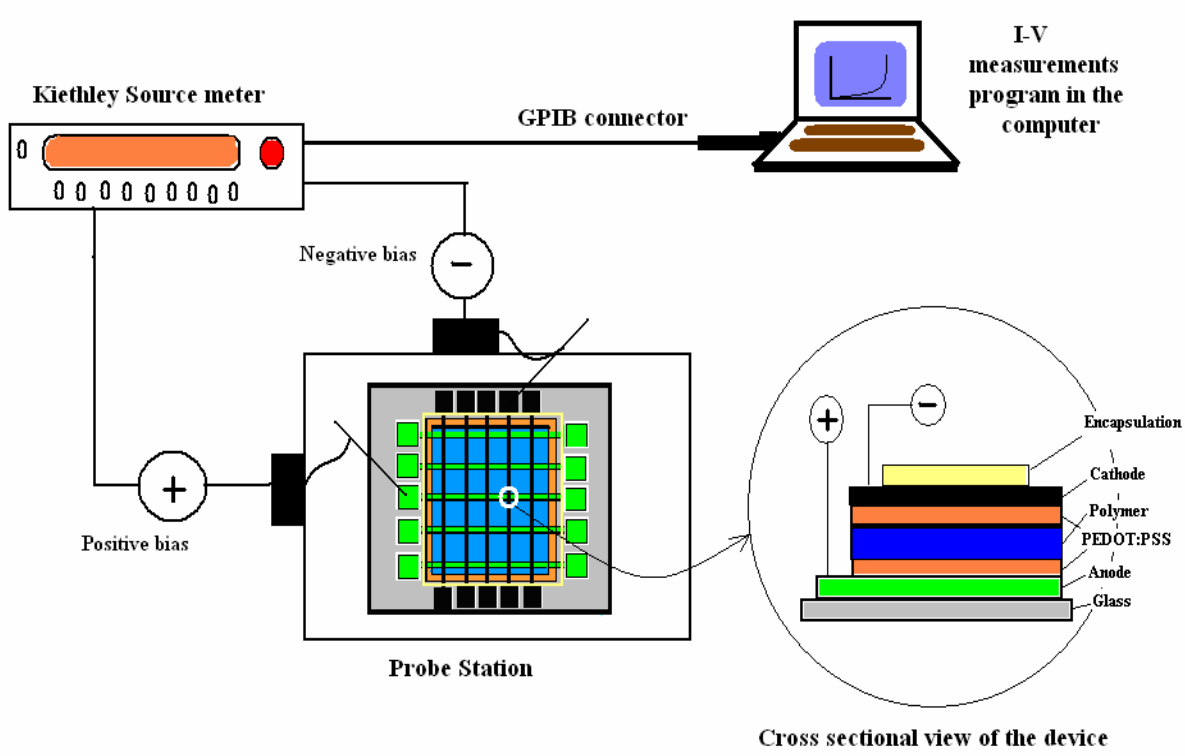

Figure (3.16): Schematic representation of experimental arrangements of current-voltage measurements of PF based diode.

3.3.3 Temperature dependent I-V measurements set up

For temperature dependent measurements, a CTI cryogenic Model 22 refrigerator was used which can go from 20K to 480K with pressurized Helium gas. For $I-V$ measurements the device was loaded into the cryostat with proper contact as shown in Fig. 3.17. The cryogenic refrigerator was connected with a CTI Cryogenics 8001 controller (Helix Technology Corporation) and a CTI 8300 water cooled compressor with He supply. The sample in the cryostat was connected to the Kethley source measure unit

for biasing the device. A Lakeshore 321 auto tuning temperature controller was used to control the temperature in the cryostat. Data was collected with a computer connected to the source meter with GPIB connector.

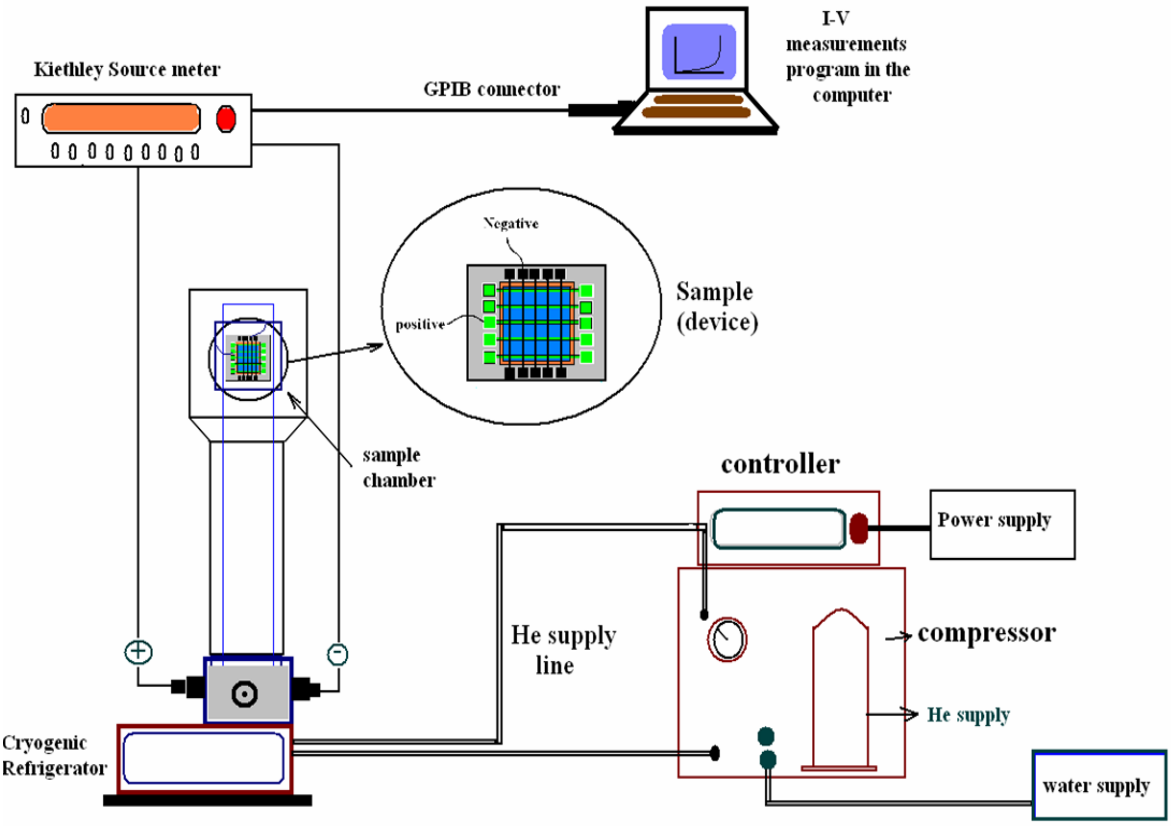

Figure (3.17): Schematic of temperature dependent $I-V$ measurements setup.

3.3.4 Raman scattering from PF based LEDs

The experimental setup for Raman scattering of PF based LEDs is shown in Fig. 3.18. For Raman scattering measurements from OLEDs a single layer PF based LED (cross sectional view shown in the figure) was at first soldered with Cu wire and then placed in the sample holder with appropriate connection. A Kiethly 2400 source meter and a computer with GPIB connector were connected with the sample holder for $I-V$

measurements. The entire sample holder is then placed inside the micro Raman setup. The device was focused with microscope lenses attached to the system and the scattered light from the device was collected in a backscattered geometry discussed earlier in the Raman setup.

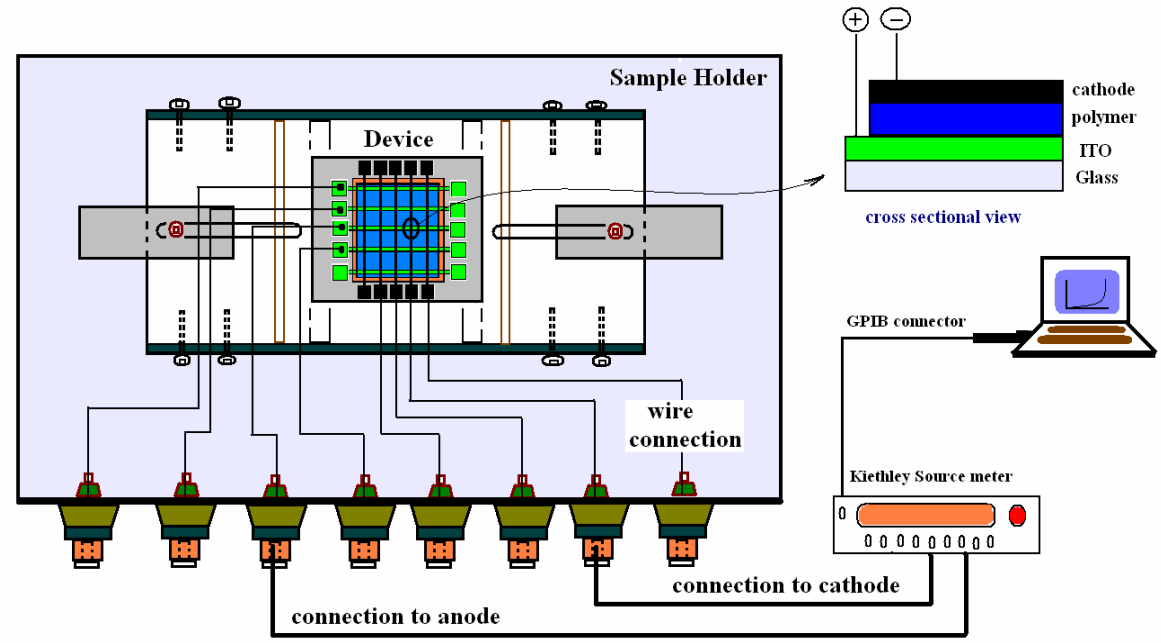

Figure (3.18): Voltage induced Raman scattering setup for PF-based LEDs.

References:

[1] www.physicscourses.okstate.edu

[2] Mark Fox, "Optical absorption of solids", Oxford University Press Inc., (2001).

[3] Suchi Guha "Raman spectroscopic studies of buckminsterfullerene and related compounds" A thesis for Doctor of Philosophy, Arizona State University, May (1996).

[4] A. Singha, P. Dhar, and Anushree Roy , American J. of Phys. **73**, 224-233, (2005).

[5] http://www.linkam.co.uk accessed on 5th April 2007.

CHAPTER 4

Organic light emitting diodes: structure and operation

4.1 Introduction

Semiconducting polymers play a major role these days as active materials in a new generation of electronic and optical devices, including OLEDs[1,2,3], photo detectors, photovoltaic cells, solar cell, sensors[4,5,6] thin film transistors[7,8,9] and optical amplifiers/lasers. OLEDs are being considered for LCDs as one of the most promising next generation flat-panel displays because of their ease of manufacturing, all solid state design, and being self-emitting with wider viewing angle.

4.2 Historical background

The EL from organic compounds was first demonstrated in 1953 by Bernanose[10] but was not significantly developed. The origin of EL in organics can be traced back to the revolutionary work on molecular crystals and, in particular, to the experiments of Pope and co-workers on anthracene single crystals in 1963 followed by Helfrich and collaborators in 1965.[11,12,13] However, the high operating voltage of devices (~1000 V) back then limited its practical use. Significant improvements in terms of driving voltages were then achieved by the use of thin films of similar materials which Roberts and co-workers were able to successfully deposit in 1979.[14] The spearhead of organic electroluminescence research was achieved by Tang and Van Slyke in 1987.[15] They introduced effective heterojunction devices of small-molecular-weight materials, which were fabricated by thermal evaporation with low operating voltages (10V) and attractive

device efficiency (1% photon/electron). Their impressive contributions to organic electroluminescent and photovoltaic devices paved the way for subsequent progress in this field.

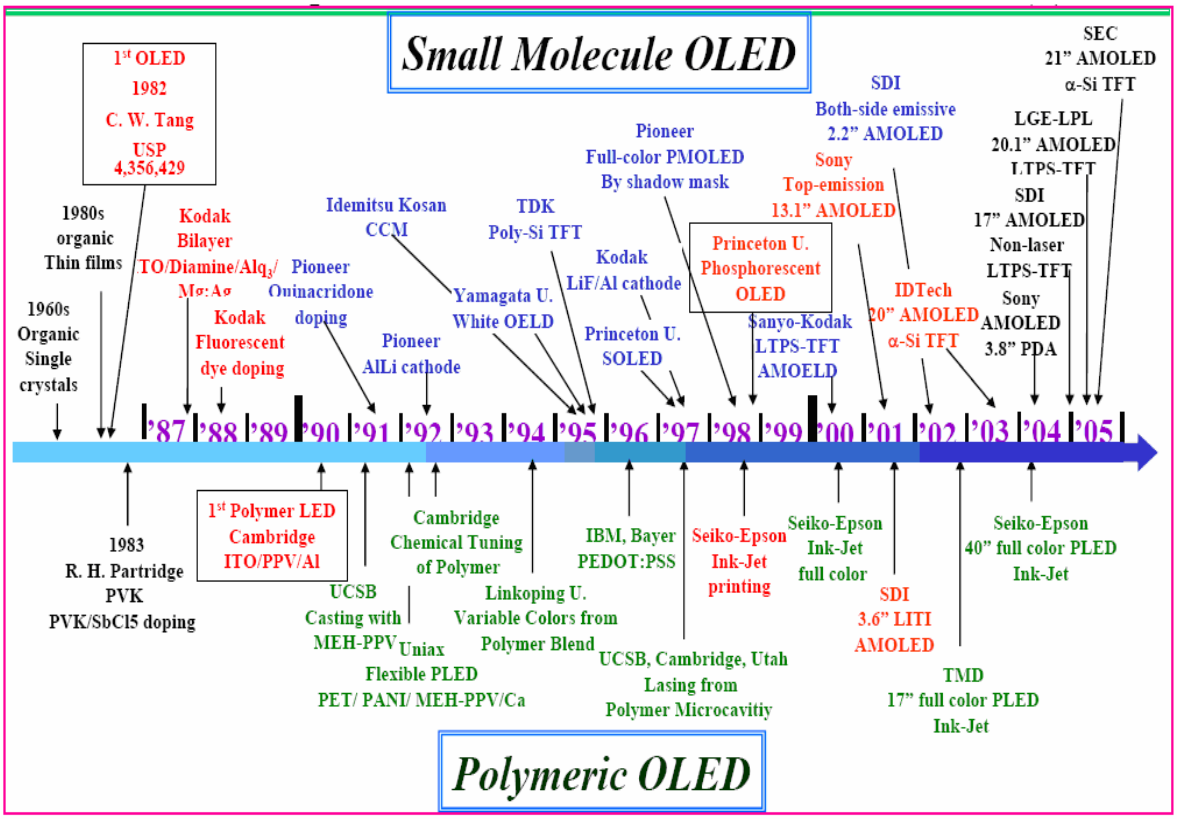

Figure (4.1): OLED history. [Reference[16]]

Some years later after reports of OLEDs of small molecular weight, in 1990 Richard Friend's group in Cambridge University demonstrated OLEDs with conjugated polymers.[17] In contrast to vacuum processing of small-molecule OLEDs, the polymer layers in OLEDs were fabricated by spin-coating or other solution-casting processes. High EL efficiency, wide viewing angle, fast response, and potentially low cost is what makes OLEDs attractive for displays. In addition, their low processing temperatures, and

thus versatility in substrates, render them suitable for some novel display applications, such as in flexible displays.

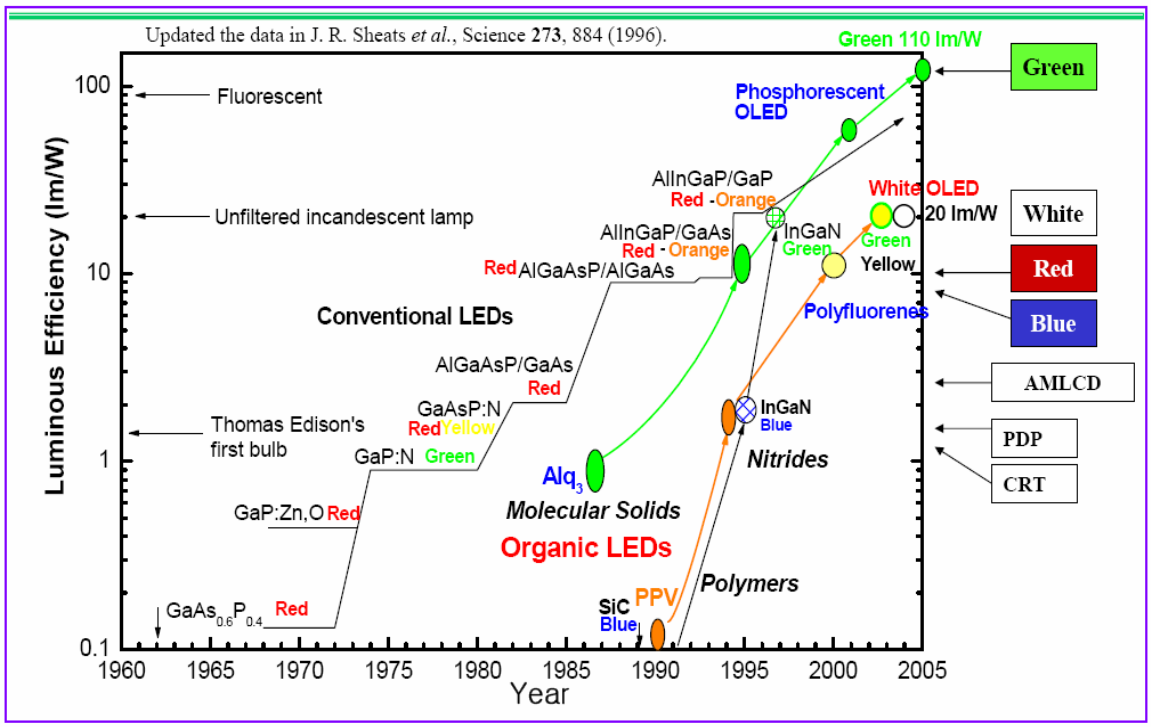

Figure (4.2): Evolution of OLED performance. [Reference[16]]

4.3 Structure/Fabrication of OLEDs

A typical OLED utilizes ~100 nm of a polymer film sandwiched between an anode and a metal cathode. When a forward bias is applied, electrons are injected from the cathode into the LUMO of the polymer and holes are injected from the anode into the HOMO of the polymer. After carriers are injected, they drift in the presence of the externally applied electric field by hopping from molecule to molecule or through the polymer chain to the opposite electrode. A schematic structure of an OLED is shown in Fig. 4.3.

In flexible OLEDs, the anode is made of a transparent conducting organic compound, e.g., doped polyannilyne or poly (3,4-ethylene dioxy-2,4-thiophene) poly sulphonate (PEDOT-PSS) is deposited on a suitable plastic substrate.

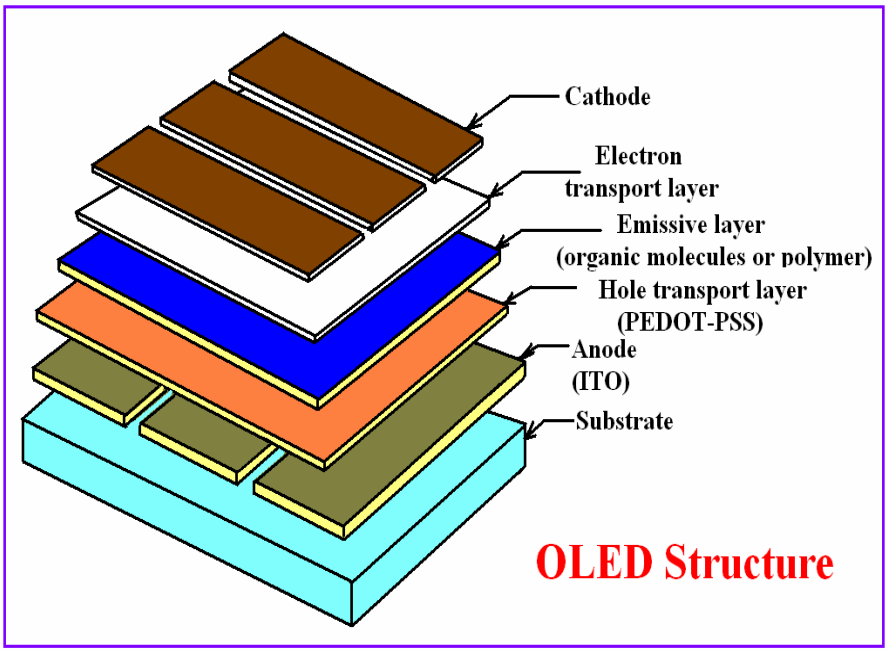

Figure (4.3): Schematic of the structure of a polymer LED.

Cathode may or may not be transparent depending on the type of metal used. The cathode is typically low-to-medium work function metal such as Ca (Φ = 2.87 eV), Al (Φ = 4.3 eV) or $Mg_{0.9}Ag_{0.1}$ (Mg Φ=3.66eV) deposited either by thermal or e-beam evaporation. However, in case of Al and Ca, addition of an appropriate buffer layer (electron transport layer) between the top organic layer and the metal cathode improves the device performance considerably. Fig.4.4 shows a typical multilayer OLED structure.

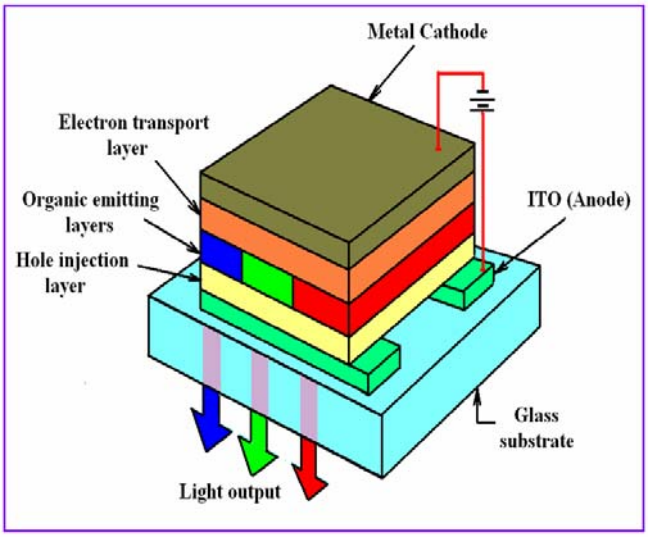

Figure (4.4): Typical structure of multi layer OLED.

Appropriate multilayer structures typically enhance the performance of devices by lowering the barrier for hole injection from the anode and by enabling control over the e^- (electron) and h^+(hole) recombination region, e.g., moving it from the organic/cathode interface, where the defect density is high, into the bulk. Hence the layer deposited on the anode would generally be a good hole transport material, providing the hole transport layer (HTL). Similarly, the organic layer in contact with the cathode would be the optimized electron transport layer (ETL).[18]

The existing OLED fabrication procedures fall into two major categories: (1) thermal vacuum evaporation of the organic layers in small molecular OLEDs (also known as SMOLED) and (2) wet coating techniques of the polymer layers. Thermal evaporation of small molecules is usually performed in vacuum of ~ 10^{-6} torr or better. However it has been observed that the residual gases in the chamber may affect the performance of the device significantly. One of the most salient advantages of thermal vacuum evaporation is that it enables the fabrication of multilayer devices in which the thickness of each layer

can be controlled easily, in contrast to wet coating techniques like spin coating. More about fabrication technique can be found in reference.[18]

4.4 Basic principle of OLEDs

Electrically injected carriers in an OLED recombine to generate light. The device physics is best illustrated by examining the simplest type of OLED with only a single organic layer. When an electron and hole capture one another within the organic layer, they form a neutral "exciton", which is a bound excited state that can decay by emitting a photon.[19] Schematic of the basic operation of OLED is shown in Fig. 4.5 and the step by step mechanism of generation of light in a typical OLED structure is shown in Fig. 4.6.

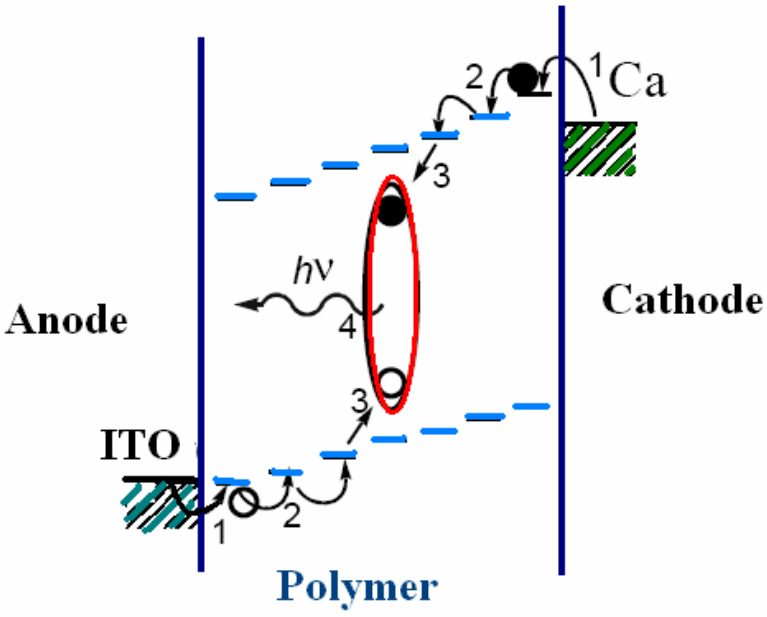

Figure (4.5): Basics of OLED. (1) Charge injection (2) Charge transport (3) Exciton formation (4) Light emission.

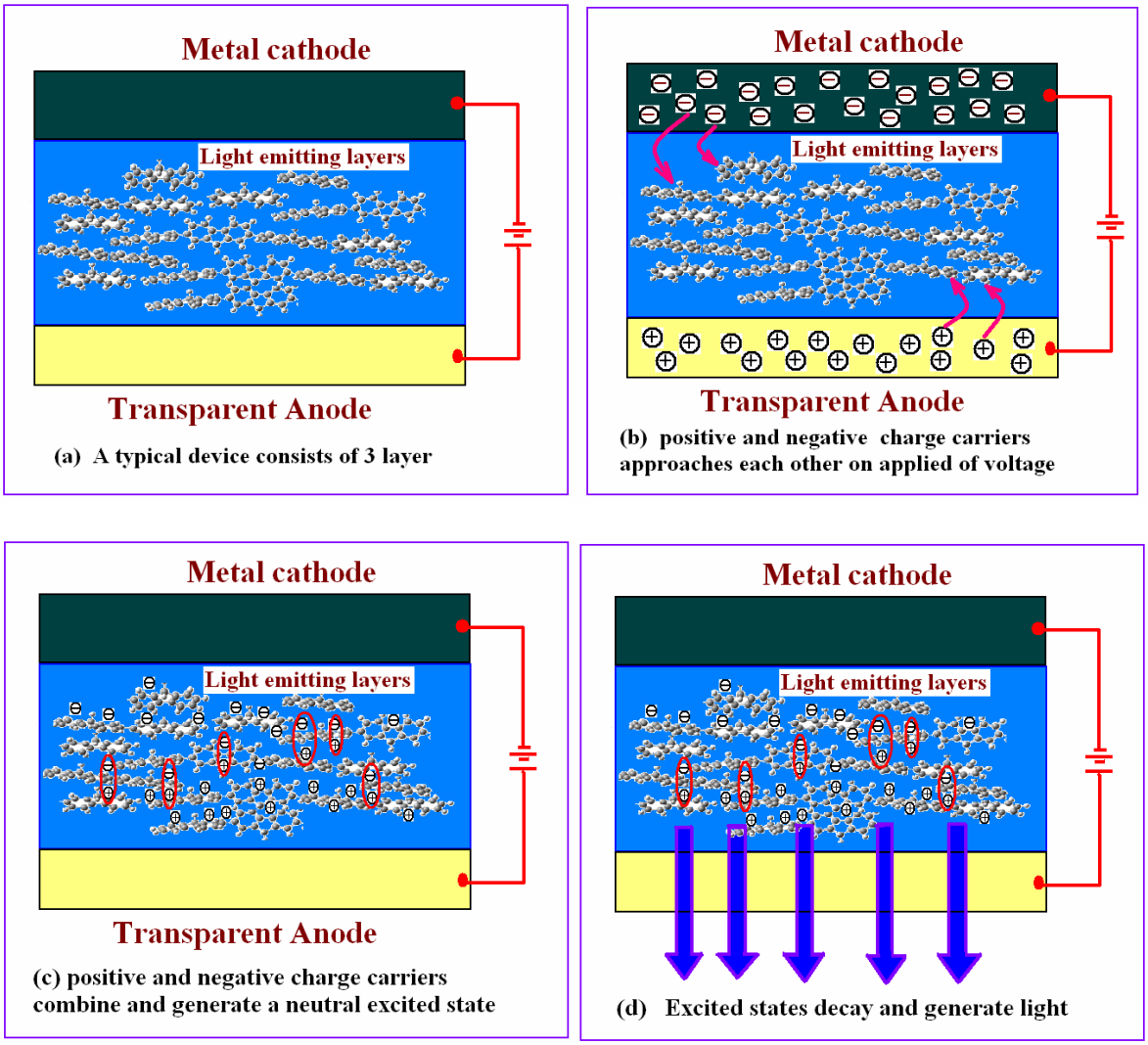

Figure (4.6): Step by step mechanism of generation of light in a typical OLED structure.

4.5 Device efficiency

An OLED is quite different from conventional p-n junction LEDs. The emission color can be tuned over a wide range by appropriate choice of polymer and small molecule based organic materials. In order to maximize the efficiency of an OLED, some factors need to be considered are: (1) electrode interface and charge balance, (2) charge

injection (3) charge transport and (4) electron-hole recombination. Fig.4.7 shows the schematic of successive steps in EL.

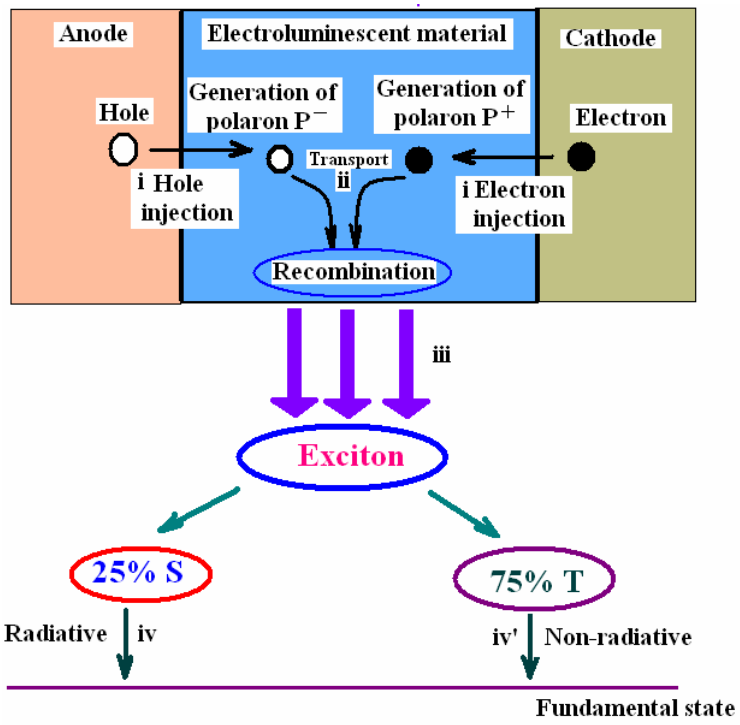

Figure (4.7): Successive steps in electroluminescence.[20]

4.5.1 Electrode interface and charge balance

In order to achieve efficient luminescence, it is necessary to have good balancing of electron and hole currents, efficient capture of electrons and holes within the emissive layer, strong radiative transitions for singlet excitons, and efficient coupling of these excitons to photon states allowed in the device structure. In an ideal picture, the maximum quantum efficiency is achieved when both cathode and anode form an ohmic contact with the polymer (i.e., there is no barrier for charge injection from the metal into the organic layer), and when the mobility of the two carriers is identical. Neglecting any interaction of the charges and the excitons with the electrodes, this condition would then

produce the maximum "charge balance," and therefore the maximum efficiency is achievable.[21]

The nature of interfaces, between the active light-emitting polymer medium and the metal electrode or between the polymer and the ITO layer, are of paramount importance in determining device performance. The control of these interfaces ultimately may be among the more important determining factors in the eventual success of light-emitting devices.[22] The chemistry that occurs at the metal-polymer interface varies with the nature of the metal involved, the polymer, and especially with the cleanliness of both the materials employed and the vacuum system used in the metallization process.[1]

Barriers are almost always present at the polymer electrode interface, and minimizing them for injection has been the effort of many researchers in last few years. The mobility of the two carriers is rarely matched in organic semiconductors. It can differ by several orders of magnitude, and the relative difference can be a function of the applied electric field. This inequality has a profound effect on charge balance, on exciton formation, on the recombination process, and ultimately on the device efficiency.[21]

4.5.2 Charge injection and transport

In spite of the strong chemical interactions between polymer and metal, there is clear evidence that the size of the barriers for electron and hole injection still scales with the electrode work functions. The height of the barrier for hole injection is determined by the difference between the work function of the anode and energy level of the π (valance or HOMO) band; the height of the barrier for electron injection is determined by the energy

difference between the work function of the cathode and the energy level of the π* (conduction or LUMO) band.

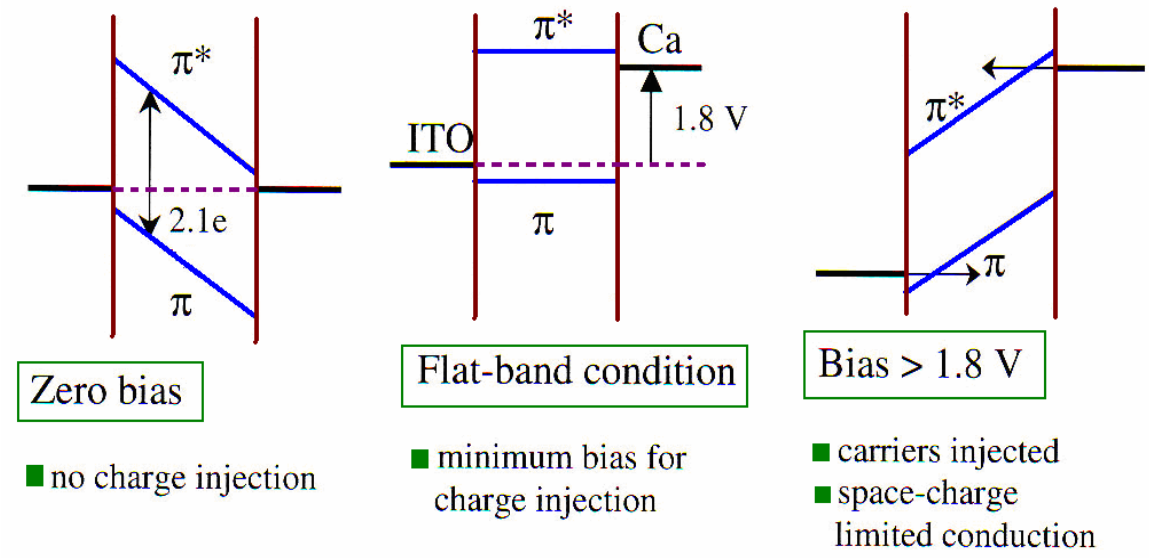

Figure (4.8): The energy band diagram of an LED.[23]

In the zero bias condition there is a common Fermi level across the device but a flat-band condition occurs when the applied voltage equals the difference in the work functions of anode and cathode. This is the minimum voltage required for injection of electrons and holes. Ideally, the electroluminescent emission should turn on at this voltage. In the forward bias condition, carriers are injected through the triangular barriers at the anode (holes) and cathode (electrons); the carriers then meet within the polymer layer where they radiatively recombine.

When a positive bias is applied to the LED, the Fermi level of the cathode is raised relative to that of the anode as shown in Fig. 4.8. Thus the thickness of the barrier is a function of the applied voltage; the barrier thickness decreases as the voltage is increased. Carriers tunnel through the barrier primarily by Fowler-Nordheim field emission tunneling,[24] which is given by

$$J_{FN}(s) = \frac{A}{\phi t^2(y)} E(s)^2 \exp\left(-\frac{B\phi^{3/2} v(y)}{E(s)}\right) \qquad (4.1)$$

where $E(s)$ is the applied electric field, ϕ is the work function of the metal, *A* and *B* are empirical constants, $y = \frac{(eE(s)/4\pi\varepsilon)^{1/2}}{\phi}$, and *v(y)* and *t(y)* are functions which arise due to the inclusion of image charge effects. *v(y)* and *t(y)* are near unity for typical conditions, and therefore the standard practice is to omit them.

Thermionic emission over the barriers can also play a role if the barriers are small and temperature is relatively high. Since the rate of injection by Fowler-Nordheim tunneling is determined by the strength of the electric field, it is important for the polymer layer to be thin so that high electric fields can be obtained at low voltages.[23] For an ideal polymer/metal interface, the form of the band bending in the proximity of the interface is also determined by the doping level of the polymer. Conjugated polymers are usually synthesized with doping level as low as possible. For low doping levels, the width of the band bending region will be considerably greater than the thickness of a typical polymer LED, implying that the electric field is constant throughout the device.[18]

To optimize the performance of OLEDs, it is important to minimize the barriers for charge injection by choosing electrodes with work functions that are well matched to the bands of the polymer. If the electrodes are well matched to the bands of the polymer, then the barrier for charge injection is small and the current that passes through the LED is not limited by injection, rather it is SCLC.[25] SCLC will be discussed in details in Chapter 5. After the optimization of interfaces between electrodes and organic layer, the charge

transport properties are determined by the bulk properties of the organic layer itself, i.e., by the mobilities of the two carriers and by the recombination process. Polymers offer the advantage over small molecules by having delocalized molecular orbitals, as long as their conjugation is preserved. This means that while electrons and holes in small molecule layers can only hop from one molecule to its neighbor, the transport properties of conjugated polymers are a combination of motion along the delocalized orbitals and hopping between different polymer chains. The carrier mobility is normally field dependent in systems where the transport is limited by hopping mechanisms. This is because the barrier for hopping is lowered by the presence of the field, therefore affecting the hopping probability. Although the exact dependence of the mobility on the electric field depends on the properties of the material, in small molecules and conjugated polymers it has been experimentally found that field dependent Poole-Frenkel model in equation (4.2) often fits the experimental data quite well and the mobility is given by

$$\mu(E) = \mu_0 \exp(\gamma E^{1/2}) \tag{4.2}$$

where E is the electric field, and μ_0 and γ are material and temperature-dependent parameters.[21]

4.5.3 Electron-hole recombination: singlet and triplet states

At low electric fields the recombination is limited by the little space charge built up in the organic layer, i.e., most of the carriers can pass into the capture radius of the opposite carrier, therefore producing a large rate of excitons per injected carriers. Due to the exponential dependence of the mobility on the electric field, the space charge increases when increasing the voltage, until a threshold is reached, where the

recombination rate is not large enough to produce efficient excitons formation. In this recombination limited regime the efficiency decreases with applied voltage.

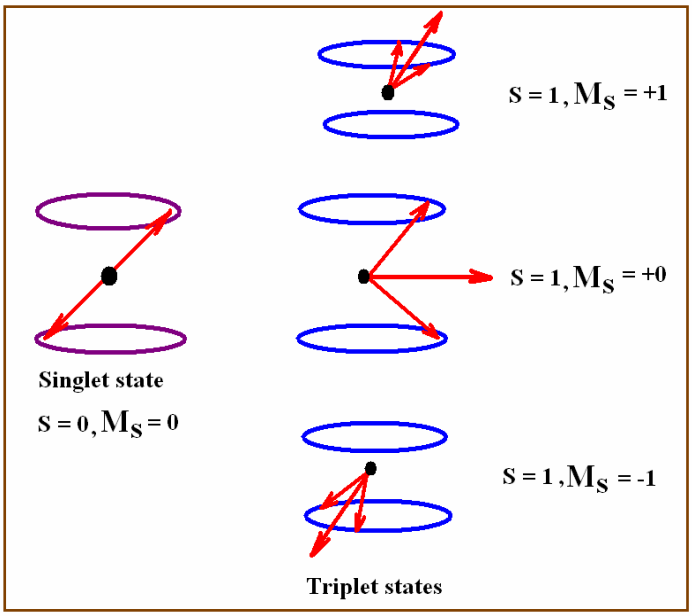

Figure (4.9): Schematic of the spin alignments for the one singlet and three triplet states.[21]

Neutral excited states are produced by charge carrier recombination, and create both singlet (S_1) and triplet (T_1) excitons. An important distinction of these two states is that the singlets can relax radiatively, whereas for the triplet states this process is forbidden, and therefore, relaxation occurs via nonradiative processes. Emission is due to transitions from neutral excited states to ground states. No experimental evidence on direct emission due to a recombination of positive and negative charges in OLED devices has been provided yet. The previous theoretical considerations[26,27] revealed that carrier recombination creates both singlet (S_1) and triplet (T_1) excitons at a ratio of 1:3 which limits the maximally possible quantum efficiency to 25%. In addition exciplex formation

between adjoining molecules, which is frequent and poses a serious problem for obtaining pure EL colors and high efficiency in organic multilayer solid devices.[28]

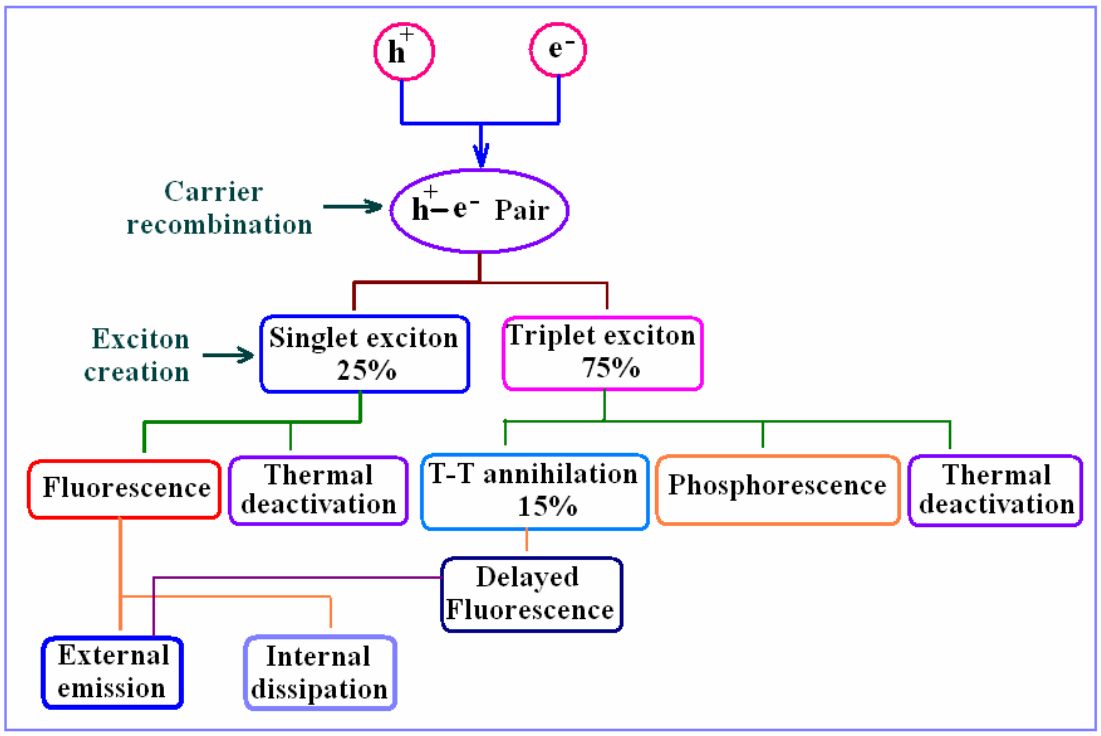

Figure (4.10): Schematic representation of the elementary processes for charge carrier recombination, production of molecular excitons, emission and external emission.[18]

Recent experiments show that the ratio of singlets and triplets can vary significantly from the spin-independent value.[29,30,31] In some cases, the number of singlets can even exceed the triplets, thus positively impacting on the quantum efficiency that can be obtained in these polymer-based materials. However, much of this is at the laboratory level and commercial OLEDs have yet to cross the 25% efficiency.

References:

[1] R. H. Friend *et al.,* Nature (London) **397**, 121–128 (1999).

[2] M. A. Baldo *et al.,* Nature (London) **395**, 151–154 (1998).

[3] D.G.Lidzey, D.D.C. Bradley, S.F. Alvarado, and P. F. Seidler; Nature (London) **386**, 135 (1997).

[4] J.J.M. Halls, C.A. Walsh, N.C. Greenham, E.A. Marseglia, R.H. Friend, S.C. Moratti & A.B. Holmes, Nature **376**, 498-500 (1995).

[5] G. Yu, J. Gao, J. C. Hummelen, F. Wudl, and A. J. Heeger, Science **270**, 1789(1995).

[6] J. J. M. Halls *et al.,* Nature (London) **376**, 498–500 (1995).

[7] C. D. Dimitrakopoulos and D.J. Mascaro, IBM, J. Res. & Dev. **45,** (2001).

[8] B. Crone *et al.,* Nature (London) **403**, 521–523 (2000).

[9] C. D. Dimitrakopoulos, S. Purushothaman, J. Kymissis, A. Callegari, and J. M. Shaw, Science **283**, 822–824 (1999).

[10] A. J. Bernanose, Chem. Phys., **52**, 396 (1955).

[11] M. Pope, H. Kallmann, and P. J. Magnante, Chem. Phys., **38**, 2042-2047 (1963).

[12] W. Helfrich, W.G.Schneider, Phys. Rev. Lett, **14**, 229-233 (1965).

[13] W. Helfrich, and W.G. Schneider, J. Chem. Phys., **44**, 2902-2907 (1966).

[14] G. G. Roberts, M. McGinnity, W.A. Barlow,, and P.S. Vincett, Solid State Comm., **32**, 683-686 (1979).

[15] C.W. Tang, S. A. VanSlyke, Appl. Phys. Lett., **51**, 913-915 (1987).

[16] Changhee Lee, Presentation on OLED 1, School of Electrical Engineering and Computer science, Seoul national University, South Korea (2005).

[17] J. H. Burroughes, D. D. C. Bradley, A. R. Brown, R. N. Marks, K. Mackay, R. H. Friend, P. L. Burns, A. B. Holmes. Nature, **347**, 539 (1990).

[18] Joseph Shinar, "Organic Light Emitting Devices , A survey", Springer-Verlag New York, Inc. (2004).

[19] R. Friend, J. Burroughes and T. Shimoda, Physics World, 35-40 (1999).

[20] André Moliton, Roger C Hiorns, Polymer International, **53**, 1397-1412 (2004).

[21] N. K. Patel, S. Cinà, and J. H. Burroughes, IEEE, J.QE, **8,** No.2 (2002).

[22] W. R. Salaneck, & J. L. Bredas, Adv. Mater. **8**, 48-52 (1996).

[23] Klaus Muller and Ullrich Scherf "Organic light emitting devices synthesis properties and applications", Wiley-Vch.(2006).

[24] R.H. Fowler and L. Nordheim, Proc. R. Soc. London, Ser. A, **119**, 173 (1928).

[25] P.W. M. Blom, M. J. M. De jong, J. J. M. Vleggaar, Appl. Phys. Lett. **63**, 3308 (1996).

[26] M. Pope and C.E. Swenberg, Electronic Processes in Organic Crystal, Oxford University Press, New York, (1981).

[27] T. Yonezawa, T. Nagata, H. Kato, A. Imamura, and K. Morokuma, Introduction of Quantum Chemistry, Kagaku-Dojin, Japan, (1983), (in Japanese).

[28] N.J. Turro, Molecular Photochemistry, Benjamin, san Francisco (1965).

[29] Y. Cao, I. Parker, G.Yu, Z. Gang, and A. Heeger, *Nature*, **397**, 414, (1999).

[30] M. Wohlgenannt, K. Tandon, S. Mazumdar, S. Ramasesha, and Z. V.Vardeny, *Nature*, **409**, 494 (2001).

[31] J.S. Kim, P. K. H. Ho, N. C. Greenham, and R. H. Friend, J. Appl. Phys., **88**, 1073, (2000).

CHAPTER 5

Space-charge-limited conduction and role of defects in OLEDs

5.1 Introduction

The understanding of the basic physics underlying electrical, thermal, and optical behavior of organic materials is essential for the optimization of organic optoelectronic devices. Light emission from a thin film OLED with high quantum efficiency depends upon a complex combination of various electronic processes;[1] dual carrier injection of electrons and holes[2,3] followed by the transport of these charges in the bulk of the film to achieve electron and hole balance being one of the most important.

The charge injection and transport at the organic-metal interface of OLEDs have been extensively studied and reported.[4,5,6] The classical mechanism of the charge carrier injection depends on the potential barrier at the interface and on the temperature dependent energy of electrons or holes incident on that barrier.[7] Alternatively, the injection by means of thermally assisted hopping of charge carriers from the metal electrode into localized electronic states of the polymer may occur.[8] Once charge carriers are injected, their transport through the organic layer towards the adjacent electrode under the influence of the external electric field is determined by the conduction and bulk properties of the material itself. Most organic materials are prone to have defects or traps due to their weak molecular bonds and structural disorder, which introduce localized energy levels inside the band gap between HOMO and LUMO of the organic layers.

5.2 Defects in organic materials

Traps which are favorable energy states inside the band gap of the material can be shallow or deep or distributed in energy. Shallow or deep trap is defined depending on the position of the Fermi level with respect to the trap energy level. For hole traps if the Fermi energy level lies above the trap energy level it is called shallow trap, on the other hand if the Fermi energy level lies below the trap level, it is called deep trap with respect to valance band (shown in Fig. 5.1). The reverse is true for electron with respect to conduction band edge.[9]

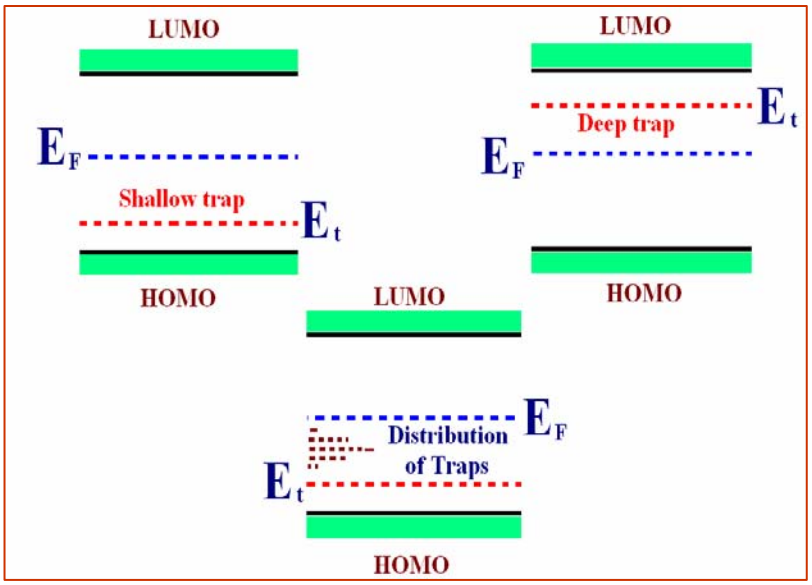

Figure (5.1): Schematic of typical hole traps.

In organic semiconductors the width of the bands can be very narrow and extended states are rarely observed. Especially in amorphous layers of organic thin films the density of states (DOS) is quite well represented by a Gaussian-like distribution of localized states of individual molecules as presented in Fig. 5.2.

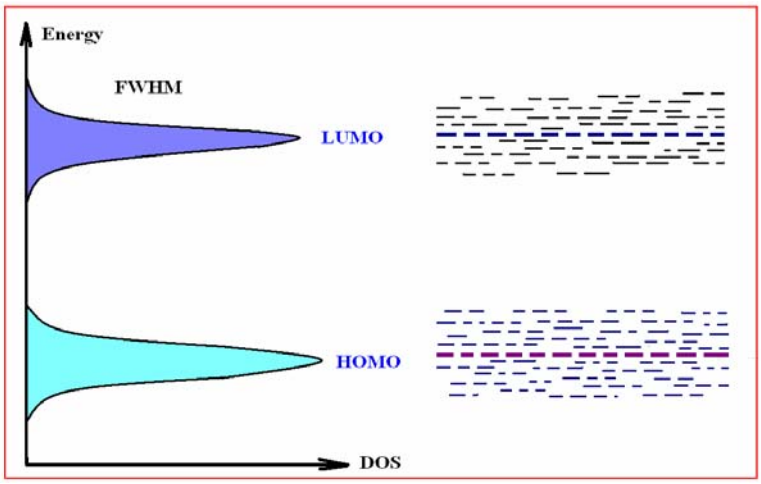

Figure (5.2): Distribution of HOMO and LUMO levels in amorphous organic semiconductors.[10]

Electrical transport is always accompanied by frequent capture of the charge carriers in localized states which may be released after a specific retention period or may recombine with carriers of opposite charge. In case the release rate is higher than the recombination rate, the localized state is called a trap while for a dominant recombination rate the localized state forms a recombination centre.

The magnitude and nature of the current flow changes markedly in which a dominant trap or set of traps exists in the material. In this case, the equilibrium concentration of mobile carriers is greatly reduced, since many of the charge carriers in the system occupy trap states. However, all injected carriers, whether mobile or trapped, contribute to the voltage drop in the material.[11]

Origin of traps

In materials with a high degree of structural disorder, even though chemically very pure, e.g., evaporated films or vitreous solids, one may expect to find traps smoothly distributed in energy (a continuum of localized trapping states will presumably be present

also in good pure single crystal) due to varying degree of association of impurities or structural defect states with each other or with other types of structural defects, such as dislocations.[9] For impurities, if the incorporated molecule is positioned in the gap of the host molecules, it will form a trap state. If a specific kind of structural defect occurs with enhanced probability, for example, on grain boundaries in polycrystalline layers, structural defects may result in more or less discrete trap states deep in the gap.

Sometimes an excess charge carrier in organic molecules leads to a molecular deformation which causes a lowering in energy for the excess charge carrier. Such a carrier together with its molecular deformation is a quasi-particle called polaron. If two charge carriers share the same molecular deformation, a bipolaron is formed. The mobility of a polaron or bipolaron is at least one or two orders of magnitude lower than the mobility of a "free" carrier. In some polymers like polythiophene or polyacetylene the polaron formation causes a lowering in energy of several hundreds of meV. In such cases the charge carrier forms its own trap state on the polymer chain. Such a trapping mechanism is called self-trapping.[10]

5.3 Trap energy level distribution

The origins of the trap states in π-conjugated polymer/molecules are not completely clear at present. Various theoretical models have been developed to understand the effect of traps on conduction and luminescence properties of the system[9,12,13] and have been applied to OLEDs.[14,15,16,17] The trap energy level distribution is generally described by one of the following ways: (1) space-charge-limited conduction with discrete energy levels, and (2) extended distribution of traps with an (a) exponential distribution, and (b)

uniform distribution. In the next section we will focus only on discrete and exponential distribution of traps.

5.3.1 SCLC with discrete trap levels

Current flow through an insulator is limited by space charge when carriers in excess of those present in thermal equilibrium can be injected through an Ohmic contact.[18] Rose[19] and Lampert[9] have shown that space charge limited current measurements are a sensitive tool for the study of insulators. SCLC methods yield information about the charge carrier mobility, their concentration and energy distribution of localized defects or carrier trapping states.[20]

When charge carriers are injected into an insulator by an applied electric field, the injected space-charge decreases the electric field at the injecting surface and can give rise to a space-charge-limited current.

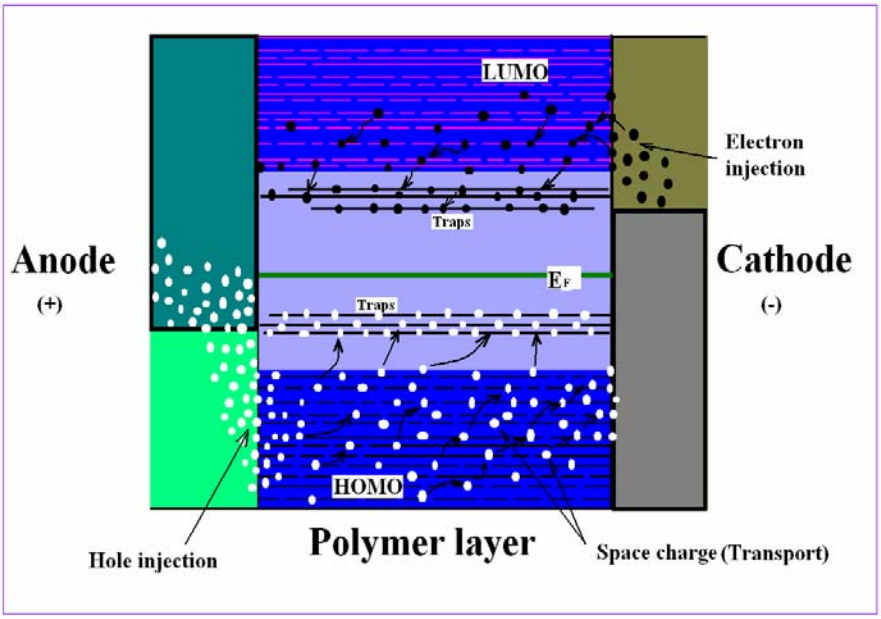

Figure (5.3): Schematic picture of charge injection and space charge transport.

An approximate theory of SCLC in a trap-free insulator was proposed by Mott and Gurney[21,22] and later extended by Rose, Lampert and Mark, and others[23,12] to describe currents limited by the space-charge confined in a single discrete energy level and in localized states with a distribution of energy. The simplified SCLC theory, which is usually applied to model the *I-V* characteristics in organic devices, is based on two main approximations: (1) diffusion currents are neglected to describe the current flow and (2) the Ohmic contact is taken to be an infinite reservoir of charges available for injection. The first approximation simplifies the theory to mathematically manageable for elementary analysis. The second approximation makes the theory independent of any detailed properties of the contact and thereby makes a universal theory possible. In the next section we have briefly discuss the simplified theory and approximate solutions for one carrier current injection in a perfect trap free insulator and insulator with traps. [For a detailed discussion see Lampert and Mark.[9]]

The exact theory for one-carrier SCLC including diffusion, even in the case of a trap free insulator, is extremely complex because it involves the solution of nonlinear differential equations. Approximate analytical solutions[24,25] and numerical treatments[26,27,28,29] of the exact theory have been reported in the literature, but most of them have been proposed to describe the charge carrier transport in inorganic crystals.[30] The current induced by injection of one type of charge carrier while including diffusion at the injection interface has also been reported in the literature.[31] For a review on numerical models of electrical transport in organic insulators see [reference[32]].

The equations characterizing the simplified theory are:

$$J = e\mu nE = e\mu n\frac{V}{L} = \text{constant}, \qquad (5.1)$$

where J is the current density, e is the electronic charge, n is the charge carrier density, μ is the carrier mobility, E is the electric field, V is the applied voltage, and L is the thickness of the sample.

Further
$$(\varepsilon / e)(dE / dx) = n - n_o + \sum_j \left(n_{tj} - n_{j,o}\right), \tag{5.2}$$

where $\varepsilon = \varepsilon_o \varepsilon_r$, ε_0 is the dielectric permittivity and ε_r is the relative dielectric permeability. n_o refer to the thermally generated free carriers and n_t is the trap charge carrier concentration.

For electrons,
$$n(x) = N_c \exp\left(\frac{F(x) - E_c(x)}{kT}\right) \tag{5.3}$$

N_c is the effective density of states in the conduction band, $F(x)$ the Fermi level, E_c is energy of the conduction band edge, k being the Boltzmann's constant and T the temperature in degrees Kelvin, in Eq. (5.3).

$$n_{tj}(x) = \frac{N_{tj}}{1 + (1/g_j)[N_j / n(x)]}, \tag{5.4}$$

where N_t is the concentration of traps and g is the degeneracy factor (statistical weight) for the traps.

$$N_j = N_c \exp(E_{tj} - E_c)/kT\,. \tag{5.5}$$

These equations are solved subject to the boundary condition $E(0) = 0$.

The perfect trap free insulator is the solid state analog of the thermionic vacuum diode. There are neither thermal free carriers nor trapping states in the solid, that is n_o and all the n_{tj} are identically zero in the above equations. The starting point of a SCLC

problem is the one-dimensional single-carrier drift current Eq. 5.1 and Poisson's equations

$$(\varepsilon / e)(dE / dx) = n . \tag{5.6}$$

These two equations combine to give

$$E(dE / dx) = J / \varepsilon\mu . \tag{5.7}$$

This differential equation, subject to the boundary condition $E(0) = 0$ is readily integrated to give

$$E(x) = (2J / \varepsilon\mu)^{1/2} x^{1/2} \tag{5.8}$$

and

$$V(x) = \int_0^x E(x)dx = (8J / 9\varepsilon\mu)^{1/2} x^{3/2} \tag{5.9}$$

Taking $x = L$ and $V = V(L)$ in the above relation, we obtain current-voltage characteristic

$$J = (9/8)\varepsilon\mu(V^2 / L^3) \tag{5.10}$$

This above equation is referred to as the trap-free square law, the Mott-Gurney square law and or Child's law for solids.

I-V for discrete set of traps

Discrete trap levels are more often associated with traps that are farther apart from each other, preventing them from strong coupling. Because of the discrete nature, the $I - V$ characteristic usually has a sharp transition region shown in Fig. 5.5, signifying the change from empty to filled states of the traps.

According to the SCLC theory, for low bias (and neglecting diffusion) in a device with ohmic contacts, the number of injected carriers is smaller or comparable to the thermally generated intrinsic charge carriers, and the $I - V$ characteristics can be

described by Ohm's law. The slope of $\log J - \log V$ plots at low voltages is then equal to 1 shown in Fig 5.5. This condition breaks down at the space charge limit when the injected carrier density becomes so large that the field due to the carriers themselves dominates over that of the applied bias and then becomes space charge limited.[33] Under these circumstances, it becomes trap limited SCLC given by Child's law in presence of discrete shallow trap Eq. (5.11). This behavior is characterized by a strict quadratic dependence of current on voltage (slope 2) in a $\log J - \log V$.

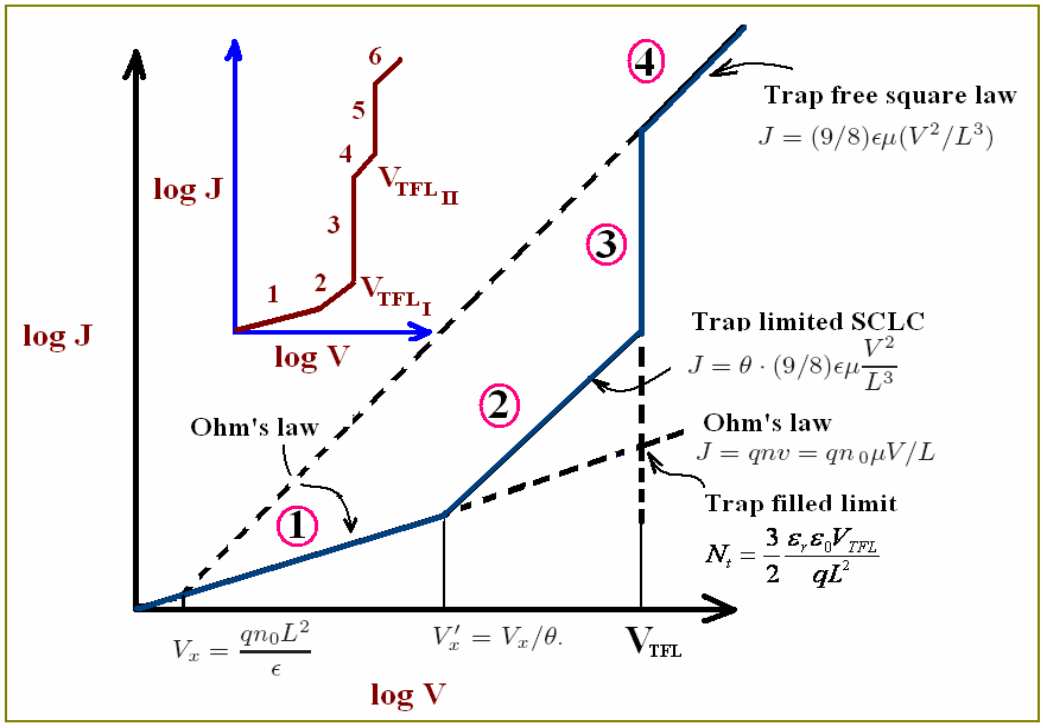

Figure (5.5) Schematic of one-carrier SCLC voltage characteristic for an insulator with a single trap level: (1) Ohmic region, (2) Child's law in the presence of shallow trapping, (3) trap-filled-limit (V_{TFL}), (4) Child's law in the absence of trapping. The inset graph represents one carrier SCLC voltage characteristics for two distinct trap levels; (3) and (5) are V_{TFL} marking the filling of traps lying lower than the quasi-Fermi energy level E_F.

In the case of trap-limited SCLC, Eq. 5.10 is modified as

$$J = \frac{9}{8}\varepsilon_r \varepsilon_0 \mu \theta \frac{V^2}{L^3} \tag{5.11}$$

Apparently this relation has the same $J - V^2$ dependence but a smaller magnitude than that of the trap-free SCL current. The magnitude of current differs approximately by a factor of θ (trapping parameter) between the two cases and is given by

$$\theta = \left(\frac{N_v}{N_t}\right)\exp\left(-\frac{E_t}{kT}\right), \tag{5.12}$$

where N_t is the density of traps N_v is the effective density of states in the valance band and E_t is the energy of trap level. The crossover voltage V_x from Ohm's law to the shallow trap square law will be $1/\theta$ times the cross over voltage for the trap free case and is given by

$$V_x \approx \left(\frac{en_o L^2}{\theta \varepsilon}\right). \tag{5.13}$$

At the trap-filled limit, the onset of trap filled voltage V_{TFL} results in the density of traps

$$N_t = \frac{3}{2}\frac{\varepsilon_r \varepsilon_0 V_{TFL}}{qL^2}\ , \tag{5.14}$$

and finally when all the traps are filled the current is only limited by the space charge and free from the influence of traps. This trap-free SCLC region is similar to equation 5.11 with θ =1, this region is also known as Mott-Gurney law or Childs law in absence of trapping and given by Eq. 5.10.

5.3.2 SCLC with exponential distribution of traps

Considering a hole-only device the distribution function for the hole trap density as a function of energy level E above the valence band, and at a distance x from the injecting contact for holes can be written as[12]

$$h(E,x) = n(E)s(x), \tag{5.15}$$

where $n(E)$ and $s(x)$ represent the energy, and spatial distribution function of traps, respectively. An assumption of uniform spatial trap distribution within the specimen from injecting electrode to collecting electrode implies that the effective thickness of the device, under space charge conditions, remains the thickness itself, and $s(x) = 1$. The specific functional form of the SCLC $J - V$ curve depends on the distribution of trap charges in the band gap.[34]

When traps have an exponential energy distribution, then the distribution of trapped charge is given by[9,12,13]

$$h(E) = \frac{N_t}{E_t}\exp\left(\frac{-E}{E_t}\right); \tag{5.16}$$

and the corresponding $J - V$ relation is given by the Mark-Helfrich law[20]

$$J = N_v \mu q^{1-l}\left[\frac{\varepsilon_r \varepsilon_0 l}{N_t(l+1))}\right]^l \left(\frac{2l+1}{l+1}\right)\frac{V^{l+1}}{L^{2l+1}}. \tag{5.17}$$

The empirical parameter $l = T_t/T$, T is the measurement temperature and T_t is the characteristic temperature. T_t is related to the characteristic energy of the trap distribution, $E_t = kT_t$ where k is the Boltzmann constant. The parameter l describes how the concentration of traps changes with energy in the forbidden gap; l =1 being the

shallow-trap behavior with a discrete energy. Equation (5.17) predicts a $J \propto V^m$ dependence, where $m = l + 1$ Thus, the slope of a $\log J - \log V$ plot directly determines the characteristic temperature and energy.

Sometimes it is desirable to write Eq. (5.17) in the Arrhenius form to bring out the temperature dependence of the current. After simple algebraic manipulations it can be rewritten as

$$J = \left(\frac{\mu_p N_v q V}{L} \right) f(l) \exp\left[-\frac{E_t}{kT} \ln\left(\frac{q N_t L^2}{2\varepsilon_s \varepsilon_0 V} \right) \right] \tag{5.18}$$

where

$$f(l) = \left(\frac{2l+1}{l+1} \right)^{l+1} \left(\frac{l}{l+1} \right) \left(\frac{1}{2^l} \right). \tag{5.19}$$

For any value of l>2 taking f (l) as a constant introduces negligible error in current. Equation (5.18) can therefore be written as

$$J = \left(\frac{\mu_p N_v q V}{2L} \right) \exp\left[-\frac{E_t}{kT} \ln\left(\frac{q N_t L^2}{2\varepsilon_s \varepsilon_0 V} \right) \right]. \tag{5.20}$$

Eq. (5.20) provides the Arrhenius dependence of current on temperature and gives the activation energy as[35]

$$E_a = \frac{E_t}{k} \ln\left(\frac{q N_t L^2}{2\varepsilon_s \varepsilon_0 V} \right) \tag{5.21}$$

This is an important result because it relates directly the slope of $\ln J - 1/T$ curves at a constant voltage to the total trap density. Here E_t can be determined from the slope m of the $\log J - \log V$ curves at any one temperature. Further, an examination of Eq. 5.20 shows that the current is almost temperature independent at a crossover voltage V_c. The

variation in current at the crossover voltage for different values of l is less than (1%) where $E_a = 0$, and

$$V_c = \frac{qN_t L^2}{2\varepsilon_s \varepsilon_0} \tag{5.22}$$

From $\log J - \log V$ plots, extrapolating the power law determines the crossover voltage V_c which directly gives N_t provided other parameters in Eq. 5.22 are known.

I-V for exponential distribution of traps

For exponential distribution of traps the $I-V$ characteristics can be described by trap charge limited model where the $\log J - \log V$ curves can be divided into three distinct regions. (a) , (b), (c) as shown in figure (5.6).

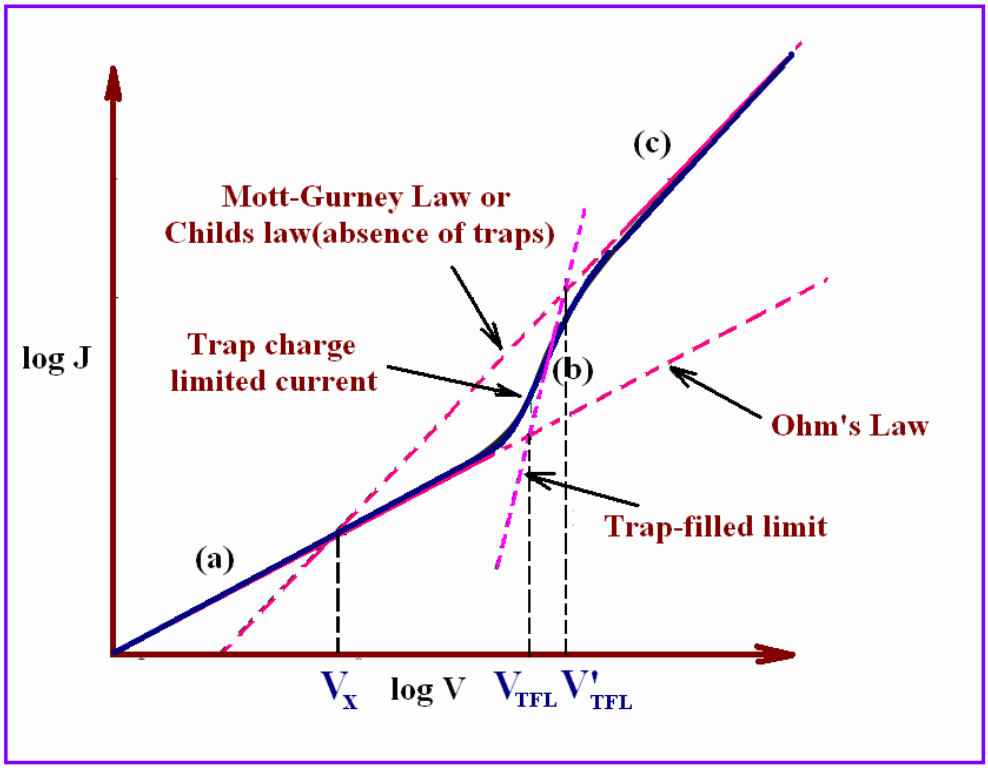

Figure (5.6): Current-voltage characteristics for exponential traps.

In region (a) the applied external electric field is small and the interface barrier blocks charge injection; hence the number of charge carriers participating in the current does not increase. Current depends exclusively on applied field, and on the conductivity of the material. Conduction is due to the intrinsic thermally generated charge carriers, as well as due to some charges associated with the dopants, and obeys Ohm's law.

The region (b) is known as the charge injection limited and trap filling region. When the applied voltage passes the threshold of blocking the number of charges, the total current increases with increase in voltage. We understand this as the filling of traps within the bulk where the bulk material accommodates this increase in charge carriers. Rapid increase in current with small increases in voltage is due to this increase in charge carrier density in the bulk. This region is characterized by $J = KV^m$, m is the slope. This is usually described by the power law which assumes the filling of traps distributed exponentially or uniformly within the band gap, the maximum density being at the band edge. If the trap distribution is discrete, then the curve is vertical in region (b). The slope therefore can be used as a criterion for comparison of the stretching of the exponential distribution. Low slope implies gradual (extended) distribution, while higher slopes indicate sharp distribution.

In the intersection region between (b) and (c) all existing trapping centers are occupied by injected charge carriers, and the material starts to resist any further injection. If the mobility is so low that the extra injected charges cannot be swept to the collecting electrode at the same rate at which they are being injected, space charge then accumulates near the injecting electrode and creates a field impeding further injection. The rate of

increase of current with voltage decreases, until it becomes constant again when all traps are occupied. Trap free space charge limited current should then flow.

Finally region (c) corresponds to trap free space charge limited current. Since the obtained slope in the double log plot is equal to 2 and is described by Child's law. Note that this law does not necessarily imply the absence of traps in the material, but rather that they are all filled.

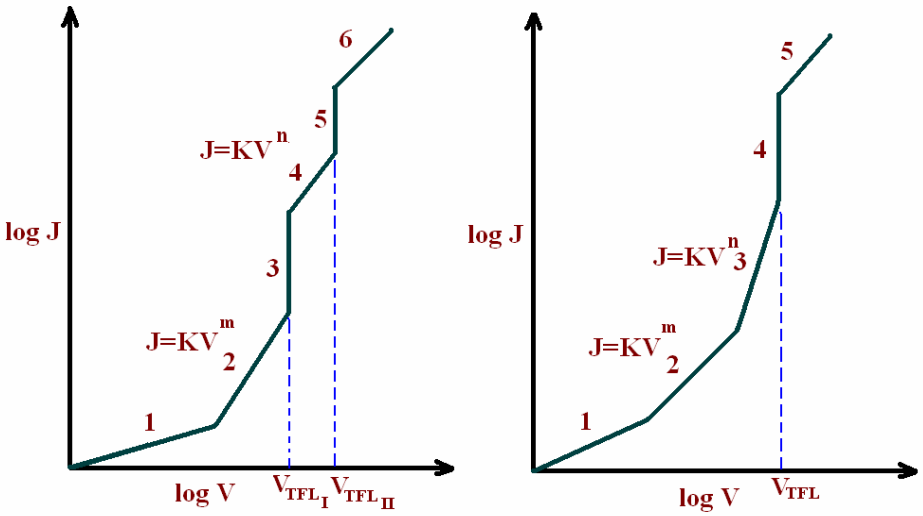

Figure (5.7): Prototypical current-voltage characteristics for SCLC flow with two sets of exponential distribution of traps and with two overlapping trapping centers distributed in energy where m and n are greater than 2

If there is more than one TCL (trap charge limited) region which can be represented by exponential distribution or uniform distribution present, then there will be several transition in the current as the quasi Fermi level sweeps through each set of traps with slopes more than 2 which is shown in Fig. 5.7[36, 37]

There are some additional nonliniear conduction theories which have been observed in thin film materials and are described by

$$J = J_0 \exp\left(\frac{\beta E^{1/2}}{kT}\right) \tag{5.23}$$

In Eq. (5.23), J_0, is a constant and β is a constant that changes value with changes in the conduction mechanism.[38,39] Among these conduction theories are Schottky barrier-controlled conduction , Pool-Frenkel hopping conduction, and Pool-Frenkel hopping conduction with shallow traps.

The constant in equation (5.23) $\beta = \beta_s$ is given by

$$\beta_s = \left(\frac{e^3}{4\pi\varepsilon_0\varepsilon_r}\right)^{1/2} \tag{5.24}$$

for Schottky-barrier-controlled conduction; ε_r is the high-frequency dielectric constant. Poole-Frenkel hopping conduction and Poole-Frenkel hopping conduction with shallow traps are represented by using $\beta = \beta_{PF} = 2\beta_s$ and $\beta = \beta_{PFST} = 4\beta_s$ for Poole-Frenkel conduction and Poole-Frenkel conduction with shallow traps, respectively. Since all three of these conduction methods are described by Eq. 5.23, the dominant conduction mechanism must be differentiated by determining the slope of the $\ln(J) - V^{1/2}$ curve. The refractive index of the material may be calculated from the slope by using the relation $n = \varepsilon_r^{1/2}$; comparison of the calculated refractive index to a measured value of the refractive index reveals which conduction mechanism is operative.

5.4 DOS calculation from SCLC

For determining the density and the distribution of energy states, methods other than the SCLC method can be used: field-effect technique,[40] capacitance–voltage methods,[41] and deep-level transient spectroscopy (DLTS).[42] However, these three alternative

techniques require highly doped material and specially designed device structures. It is, therefore, difficult and unreliable to use these three methods for measuring the density of states. SCLC technique proves more effective because of the ease the experiments and the relative reliability of the resolved energy distribution of density of gap states (DOS).

A number of studies show that injection current can be a powerful tool for studying insulators or high resistivity materials. The most widespread contribution from using this tool is the information about defect states in the forbidden gap. Such localized defect states can strongly influence the injected current flowing in response to an applied voltage. SCLC offers a well-established and extremely sensitive method to study energetic and special profiles of traps for current carriers in insulators and semiconductors.[43] Defect state concentrations as low as 10^{12} cm^{-3} can be detected by this technique to study energetic and spatial profiles of traps for current carriers.[44]

Different methods of analysis have been developed and demonstrated to determine the distribution function $g(E_{Fn})$, defined as the number of states per unit volume in a unit energy interval from the $J-V$ characteristics of the space-charge limited region. Few of them being: (a) step by step method (b) differential method, and (c) exponential distribution.[45]

In the **step by step method** which was adopted by den Boer (1981), the average density of states $g(E)$ is given by

$$g(E_{Fn}) = \frac{\chi \varepsilon_r \varepsilon_0 (V_2 - V_1)}{eL^2 (\Delta E_{Fn})} \quad , \tag{5.25}$$

where χ accounts for nonuniformity of the internal space charge field ΔE_{Fn}, the quasi-Fermi level, which moves towards the conduction or valance band edge with applied voltage is given by

$$\left(\Delta E_{Fn}\right) \approx kT \ln\left(\frac{J_2 V_1}{J_1 V_2}\right) \tag{5.26}$$

where J_1 and J_2 are current densities in the logarithmic $J-V$ cure as the potential is increased from V_1 to V_2.[46]

The **differential method** which is a more elaborate method of the analysis of the DOS was introduced by J. Sworakowski,S. Nespurek[43] (1980). It requires an accurate knowledge of the slope of the $J-V$ curve as a function of V. This method enables one to extract the parameters of the traps from SCL current-voltage curves without any apriori assumptions concerning their energy distribution.[47]

The DOS at the quasi Fermi level $\left(E_{Fn}\right)$ is given by

$$g\left(E_{Fn}\right) = \left(\frac{\chi \varepsilon_r \varepsilon_0}{eL^2 kT}\right)\left(\frac{V}{\{m(V)-1\}}\right). \tag{5.27}$$

The slope $m(V)$ is given by $m(V) = d(\ln J)/d(\ln(V)$ and is found by polynomial fit to the $J-V$ curve. χ is correction factor for the non-uniformity of the internal electric field and its value range from 0-1. ε_r is the dielectric constant, ε_0 = electric permittivity of the free space, L is the thickness, T is the temperature, and k is the Boltzman constant. The position of quasi-Fermi level is found to be

$$\Delta E_{Fn} = \left(E_c - E_{Fn}\right) = kT \ln\left(\frac{eN_c \mu \chi}{L}\right) + kT \ln\left(\frac{V}{J}\right) = kT \ln\left(\frac{eN_c \mu \chi V}{LJ}\right), \tag{5.28}$$

where N_c is the effective density of states in the conduction band and μ is the mobility of the charge carriers at the mobility edge and $\chi = 1$.

In case of exponential distribution of trap states discussed in previous section, when a straight-line fit to the $\log J - \log V$ characteristics is not possible the DOS can then be estimated by using an analysis known as average density of states and is given by

$$N_{t(avg)} \approx \frac{2\varepsilon \Delta V}{eL^2 \Delta E_F}, \tag{5.29}$$

where L is the thickness of the film and ΔE_F is the Fermi level shift $\Delta E_F = (E_{F2} - E_{F1})$ corresponding to a voltage change $\Delta V = (V_2 - V_1)$. ΔE_F is deduced from current-density equations as

$$\Delta E_F = (E_{F2} - E_{F1}) = kT \ln \frac{(J_2 V_1)}{(J_1 V_2)} \tag{5.30}$$

where $(J_2 V_1)$and $(J_1 V_2)$are corresponding point from $J - V$ curve. We have used the differential method to calculate the DOS from $I - V$ characteristics of PF based diodes. This is discussed in detail in Chapter 7.

References:

[1] Jan Kalinoswski, Organic Light Emitting Diodes- principles, characteristics and Processes, New York, Marcel Dekker, (2005).

[2] A. J. Campbell, D. D. C. Bradley, T. Virgili, D. G. Lidzey, and H. Antoniadis, Appl. Phys. Lett., **79**, 3872 (2001).

[3] D. Poplavskyy, J. Nelson, and D. D. C.Bradley, Appl. Phys. Lett., **83**, 707 (2003).

[4] I. D. Parker, J. Appl. Phys. **75**, 1656 (1994).

[5] P. W. M. Blom, M. J. M. de Jong, and S. Breedijk, Appl. Phys. Lett.,**71**, 930 (1997).

[6] P. S. Davids, Sh. M. Kogan, I. D. Parker, and D. L. Smith, Appl. Phys. Lett., **69**, 2270 (1996).

[7] Z. Chiguvare and V. Dyakonov , Physical Review B, **70**, 235207 (2004).

[8] T.van Woudenbergh, P. W. M. Blom, M. C. J. M. Vissenberg, and J. N. Huiberts, Appl. Phys. Lett., **79**,1697 (2001).

[9] M. A.Lampert and P. Mark, "*Current Injection in Solids"*. Academic, New York, (1970).

[10] Roland Schmechel and Heinz von Seggern, Phys. Stat. sol. (a), **201**, 1215-1235 (2004).

[11] I. B.Yaacov and U. K. Mishra, "Unipolar Space Charge Limited Transport" (2004).

[12] K. C. Kao and W. Hwang, "Electrical Transport in Solids, with Particular Reference to Organic Semiconductors", New York, (1981).

[13] M. Pope and C.E. Swenberg, Electronic Processes in Organic Crystals and Polymer, Oxford University Press, Oxford (1999).

[14] P. E. Burrows, Z. Shen, V. Bulovic, D. M. McCarty, S. R. Forrest, J. A. Cronin, and M. E. Thompson J. Appl. Phys. **79**, 7991 (1996).

[15] P. W. M. Blom, M. J. M. de Jong, and J. J. M. Vleggaar, Appl. Phys. Lett., **68**, 3308 (1996).

[16] A. J. Campbell, D. D. C. Bradley, and D. G. Lidzey, J. Appl. Phys., **82**,6326 (1997).

[17] Jie Yang and Jun Shen, J. Appl. Phys., **85**, 2699 (1999).

[18] E. Gray, Brit. J. Appl. Phys., **14,** 374-377 (1963).

[19] A. Rose, Phys. Rev. **97**, 1538 - 1544 (1955).

[20] P. Mark, W. Helfrich, J. Appl. Phys., **33**, 205-215(1962).

[21] N.F.Mott and R.W.Gurney, "*Electronic Processes in Ionic Crystals"* Oxford University Press, New York, (1940).

[22] D.R. Lamb, *Electrical Conduction Mechanisms in Thin Insulating Films* (Methuen, London, (1967).

[23] R.W. Smith, and A. Rose, Phys. Rev., **97**, 1531 - 1537 (1955).

[24] J.S. Bonham, Phys. Status Solidi A, **61**, 1198 (1971).

[25] P. Delannoy, Eur. J. Appl. Math., **7**, 13 (1981).

[26] G.G. Roberts and R.H. Tredgold, J. Phys. Chem. Solids. **25**, 1349 (1964).

[27] M.A. Lampert and F. Edelman, J. Appl. Phys., **35**, 2971 (1964).

[28] A. Rosental and A. Sapar, J. Appl. Phys. **45**, 2787 (1974).

[29] J. Staudigel, M. Sto¨ssel, F. Steuber, and J. Simmerer, J. Appl. Phys. **86**, 3895 (1999).

[30] A.B. Walker, A. Kambili, and S.J. Martin, J. Phys.: Condens. Matter **14**, 12271 (2002).

[31] M. Koehler, I. Biaggio, Phys. Rev. B **68**, 075205 (2003).

[32] A.B. Walker, A. Kambili, and S.J. Martin, J. Phys., Condens. Matter **14**, 12271 (2002).

[33] A. J. Campbell, D. D. C. Bradley, and D. G. Lidzey, J. Appl. Phys. **82**,6326(1997).

[34] Z. Chiguvare and V. Dyakonov, Phy. Rev. B, **70**, 235207 (2004).

[35] Vikram Kumar, S. C. Jain, A. K. Kapoor, J. Poortmans and R. Mertens , J. Appl. Phys., **94**, 1283(2003).

[36] A. Rizzo, G. Micocci and A. Tepore J. Appl. Physc **48**, 3415 (1977).

[37] A. Rizzo C. De Blasi, S. Galassini, G. Micocci, and A. Tepore, J. Appl. Phys.**49**, 3353 (1978).

[38] G.R. Fox and S.B. Krupanidhi, J. Appl. Phys. **74**,1949(1993).

[39] J. G. Simmons, in Handbook of Thin Film Technology, edited by L. I. Maissel and R. Glang (McGraw-Hill, New York, p. 14-1, (1970).

[40] A. Maden, P. G. Le Comber, and W. E. Spear, J. Non-Cryst. Solids., **20**, 239 (1976).

[41] M. Hirose, T. Suzuki, and G. H. Dohler, Appl. Phys. Lett., **34**, 234 (1979).

[42] J. D. Cohen, D. V. Lang, and J. P. Harbison, Phys. Rev. Lett., **45**, 197 (1980).

[43] J. Sworakowski, S. Nespurek J. App. Phys., **51**, 2098 (1980).

[44] Takahiro Matsumoto, Hidenori Mimura, Yasuaki Masumoto, J. Appl. Phys., **84**, 6157 (1998).

[45] K D. Mackenzie, P G. Le Comber, W. E. Spear,, Phil. Mag. B. **46**, no. 4, 377-389. (1982).

[46] W. den Boer, J. Phys. (Paris), Colloq., **42**, C4-451 (1981).

[47] S. Gangopadhyay, S. Iselborn, H. Rubel, B. Schroder, and J. Geiger, Philosophical Magazine, B, **51**, 33-38 (1985).

CHAPTER 6

Raman scattering studies in polyfluorenes

6.1 Introduction

Thermal cycling of PFs results in distinct backbone and side chain conformations that lead to improved optoelectronic properties. In this section we present a detailed temperature dependent Raman scattering studies of semi-crystalline PF cast from different solvents to investigate structural phase transition and conformations. The experimental results are compared with the theoretical Raman spectra which address the nature of conformational isomers in PF8. In this chapter we first mention our absorption results before moving on to the Raman scattering results in details.

6.2 Absorption measurements

The photophysical properties of PFs are known to vary strongly with the morphology of the film.[1,2] The structure of the alkyl side-chains in the 9-position of the fluorene moieties strongly influences the solid-state packing of the polymers. n-Alkyl derivatives display a unique packing behavior in the condensed phase upon thermal treatment, exposing the films to solvent vapors, or treating the polymer with solvent/non-solvent mixtures of increasing non-solvent content.[1, 2, 3]

The structure of PF8 with its numerous crystalline phases and conformational isomer was presented in detail in Chapter 2. Historically, the C_β conformer has been referred to as the β phase; this phase shows a distinct red shift of the absorption and emission peaks

with a remarkably well-resolved vibronic progression both in absorption and emission.[1] PF8 dissolved in toluene shows virtually no β phase chain formation for a freshly spin coated film; aging the solution for a few hours favors formation of the β phase. On the other hand for PF2/6, the optical absorption and emission properties are relatively insensitive to the choice of solvent and the aging process.

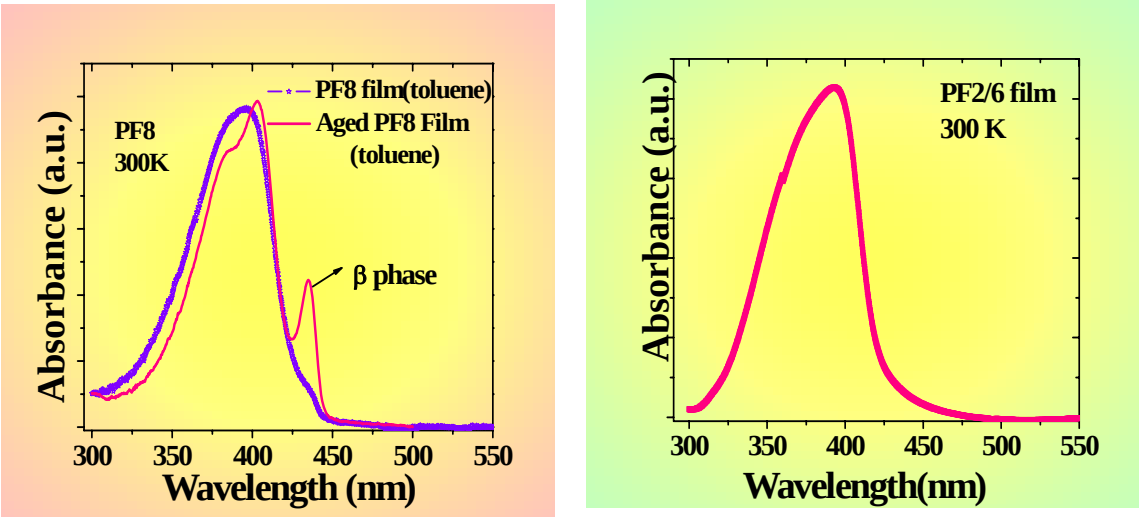

Figure (6.1): (Left) Absorption spectra of a PF8 film and an aged PF8 film. (Right) Absorption spectra of a PF2/6 film.

For our absorption spectra measurements, thin films were prepared by spin coating from toluene solution on to a sapphire substrate. The ultraviolet visible spectra (UV-Visible) absorption spectra were measured on a Shimadzu UV 2401 PC UV visible recording spectrometer. Fig. 6.1 shows the absorption spectra of PF8 and PF2/6 films. For PF8, the film was cast immediately after dissolving the polymer in the solvent and the absorption spectrum was measured, shown by the thick line. At the onset a slight shoulder is seen at 438 nm. The solution was then aged for a few hours and a new film

was cast. The absorption from this film shows a sharp peak at 435 nm, which is a signature of the β phase (shown by thin line). In contrast, the absorption spectrum of PF2/6 does not change as a function of aging indicating an absence of this particular phase. The β phase dominates the emission spectrum of PF8 and is strongly dependent upon the solvent and thermal history of the polymer.

In order to decipher the nature of the β phase we have conducted a detailed Raman scattering study of PFs as a function of solvents and thermal cycling. We point out that the β phase is not really a three dimensional phase but is representative of the C_β isomer. (see Chapter 2 for details)

6.3 Raman scattering of PFs upon thermal cycling

Raman scattering complements the techniques of XRD, PL and PLE by providing a nearly indirect, measure of the local molecular intrachain structure. In Raman scattering both the peak positions and intensities are strongly influenced by the local main chain planarity and side chain conformations. There are many ambiguities regarding chain conformations and crystalline phases in PF. Raman scattering is especially useful for PF8 studies in view of the ambiguities between the proposed families of chain conformational isomers and the various cited structural phases.

The PF8 sample was obtained from American dye Source (BE-129) and used either as received or dissolved in *p*-xylene or toluene and dried. The Raman spectra were collected by an Invia Renishaw spectrometer. The experimental set up was discussed in Chapter 3 in detail.

6.3.1 Raman Spectra: Comparison of PF8 and PF2/6

A Raman spectrum is typically insensitive to large scale changes in the long range order. This is demonstrated in Fig. 6.2 where the individual Raman spectra of PF2/6 and PF8 samples are shown before and after thermal annealing. PF2/6 serves as a reference because it undergoes, on cycling, a large scale transition from a nematic glass to an ordered semi-crystalline state marked by coherence lengths in excess of 40 nm.[4,5] The bottom and top spectra for each of the two samples represent the Raman frequencies from the as-formed bulk material at room temperature before and after thermal cycling, respectively.

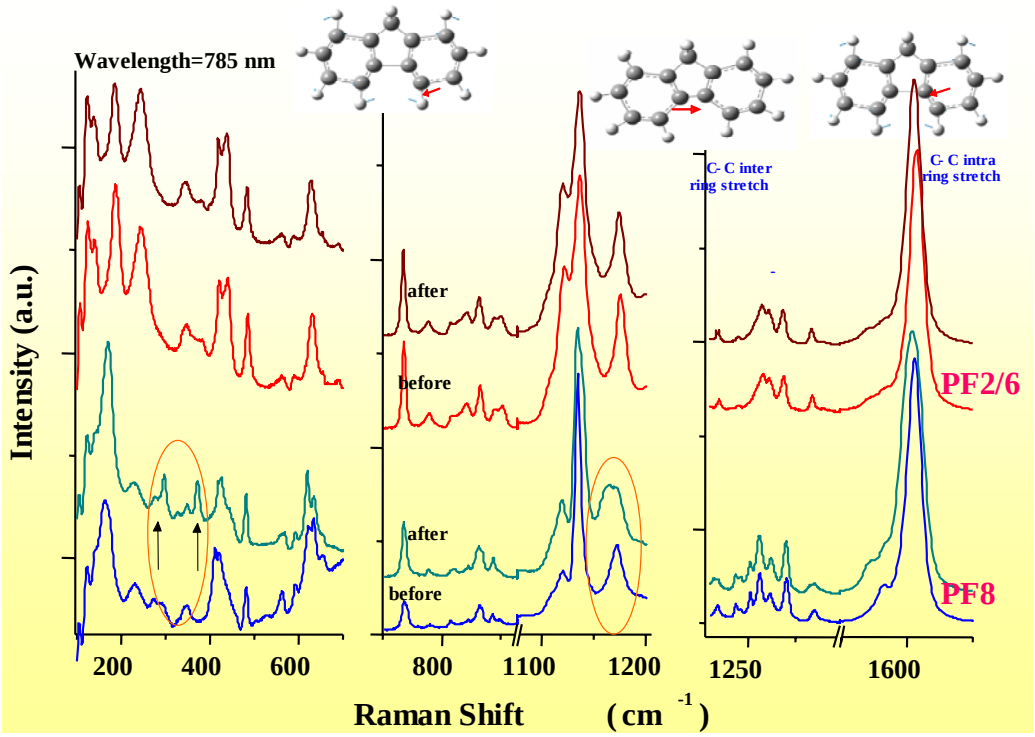

Figure (6.2): Raman spectra of PF2/6 and PF8 bulk samples. For each of the samples, "before" refers to the as-is sample and "after" denotes the sample at room temperature after cycling from the n-LC phase.

The samples were at first heated to ~170^{o}C and then cooled back to room temperature at 5 ^{o}C/minutes for thermally cycled samples. The PF2/6 sample shows only subtle changes upon thermal cycling and qualitatively the spectra look very similar to the as-is PF2/6. The Raman frequency positions do shift slightly with increasing temperature and, during cooling of this sample from the n-LC phase, the Raman frequencies exhibit a net linear shift to higher wave vector indicative of improved long-range order.[4] In a dramatic contrast to PF2/6, the Raman spectra from PF8 exhibit a multitude of distinctive changes, especially in the low frequency region as denoted by the arrows in Fig 6.2.

In review we note that the Raman spectrum of PFs is characterized by numerous intramolecular C-C and C-H stretch and bend modes throughout the 100 to 1600 cm^{-1} region. The low frequency Raman peaks in the range 100-700 cm^{-1} originate mainly from the side chains and thus this region is an extremely sensitive indicator of both side chain composition and ordering. The table 6.1 summarizes the experimental Raman frequencies of the main vibrational modes of PF8 at room temperature.

Virtually all recent temperature dependent studies of the Raman frequencies in PFs focus solely on the intermolecular C-C stretch type modes[6,7] in order to understand the changes in the backbone conformation and crystallographic phases. There has been almost no work that monitors the vibrational frequencies of the side chains. Our work here shows that side chain composition and ordering strongly impact the backbone conformation and the crystallinity. In light of this, the focus of this section is on Raman spectral features originating from the side chains and their sensitivity on thermal cycling. The changes in the Raman spectra for the three PF8 samples studied here, which are cast

from *p*-xylene, $CHCl_3$ (chloroform) and Cl-φ (chlorobenzene), correlate well with the XRD studies.[8]

Table: 6.1 Experimental Raman peaks position of PF8 and their description of the vibrations.

Experimental Raman peak cm^{-1} (PF8)	**Origin of the Raman peak**
150	LAM1 (longitudinal accordion motion)
220	D-LAM (Distorted longitudinal accordion motion)
290*	Under investigation
370*	LAM3 motion of alkyl chains
417	Ring torsion (inter-ring)
480	Ring torsion (out-of plane); C-H bend
735	Ring breathing
865	C-C stretch (bridging C) and C-H bend (in-plane)
1135	C-H bend (in-plane); ring distortion
1232	C-C stretch (inter-ring)
1257	C-H bend (in-plane)
1280/1302	C-C stretch (between monomers)
1350	C-C rock (between monomers)
1420	C-H bend and C-C stretch between adjacent monomers.
1605	C-C stretch (intra-ring)

* Thermally cycled film.

6.3.2 Effect of solvent and thermal cycling - experimental results

(a) Low frequency region (100-700 cm^{-1})

Figure 6.3 to 6.5 show the low frequency region (100-700 cm^{-1}) of the three PF8 samples cast from *p*-xylene, chlorobenzene and chloroform on heating to the n-LC phase and finally cooling to room temperature. The XRD scans are shown for comparison. (XRD data: courtesy Dr. M. Winokur, University of Wisconsin.). For all the samples the top spectrum reflects the room temperature measurement upon cooling from the n-LC phase. All three samples are characterized by an emergence of two new peaks at 290 and

370 cm^{-1}. The 370 cm^{-1} corresponds to a LAM 3 (longitudinal accordion motion) vibration in anti planar n-alkanes. The appearance of this peak in PF8 suggests a large scale increase in the population of an all anti conformation of the alkyl side chains in the presumed M-type crystalline phase of PF8. The origin of 290 cm^{-1} peak is still under investigation.

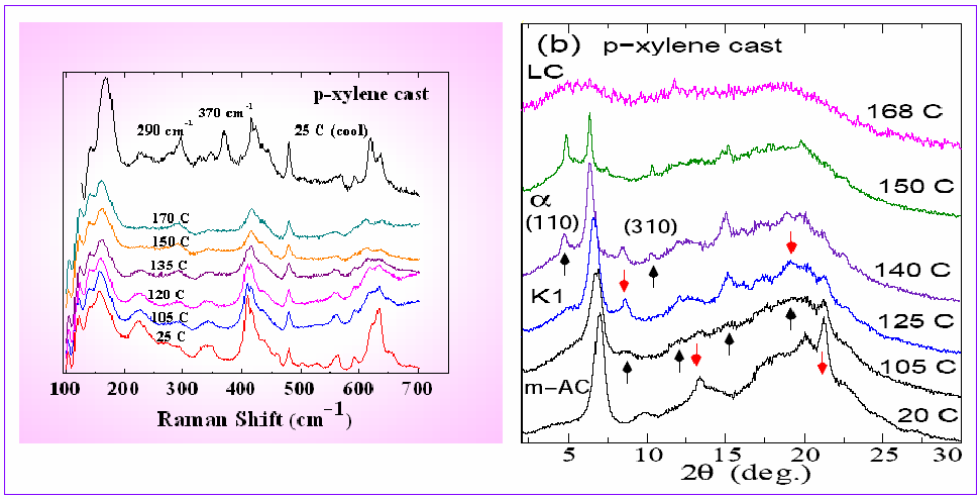

Figure (6.3): Raman spectra and XRD comparison of *p*-xylene cast PF8.

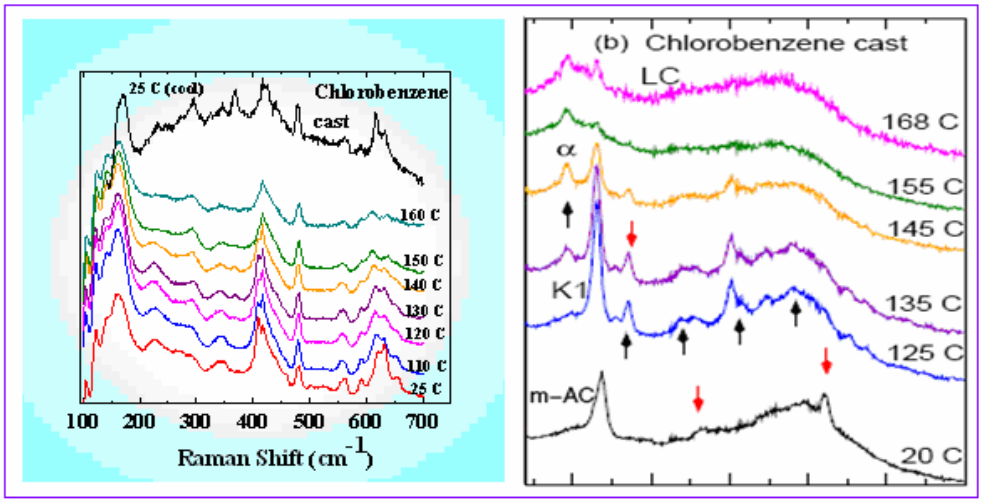

Figure (6.4): Raman spectra and XRD comparison of chlorobenzene cast PF8.

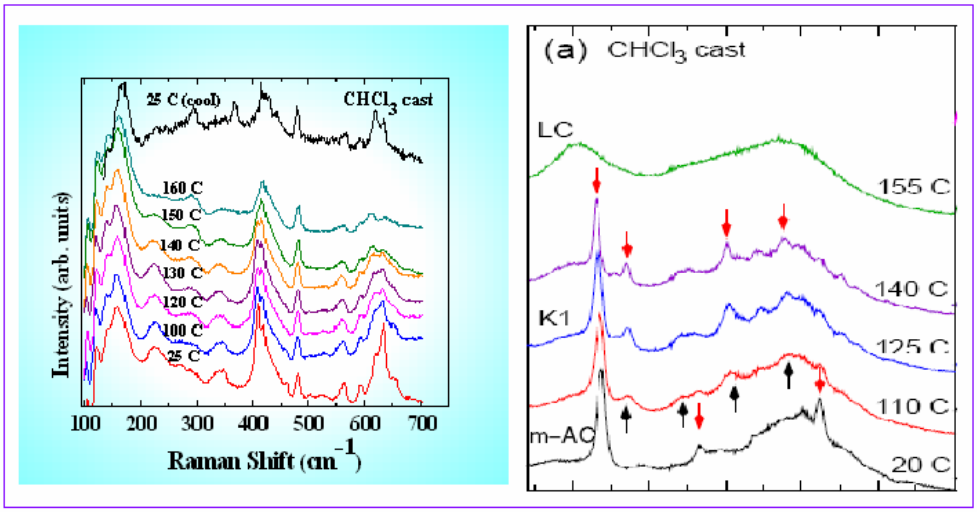

Figure (6.5): Raman spectra and XRD comparison of ($CHCl_3$) chloroform cast PF8.

Initially on heating, up to 120°C, all three samples exhibit similar changes (in peak position and relative intensities) and, in terms of the XRD[8] this correlates with cold-crystallization to the K1 structure. Although subtle, there is at least one Raman band, at 220 cm^{-1}, that directly maps with the changes in XRD. The broad 220 cm^{-1} peak has attributes that parallel the formation of the α′ and α crystal polymorphs as recorded by XRD. In the *p*-xylene cast PF8 the 220 cm^{-1} band disappears first at just above ~135°C while, for the Cl-φ cast sample, the 220 cm^{-1} peak loses intensity at a slightly higher temperature ~140-150°C and finally, in the $CHCl_3$ cast sample, this peak disappears between ~150-160°C. The *p*-xylene cast sample preferentially adopts the α crystal type on cooling from this intermediate temperature regime while the $CHCl_3$ cast sample remains in the intermediate K1 phase up to the highest temperatures and, on cooling, manifests the α′ phase.

The 220 cm^{-1} peak in n-alkanes is described as a disordered-longitudinal accordion motion (D-LAM)[9] and results from the motion of conformationally disordered alkyl

chains having short anti-planar CH_2 sequences. The reduction in intensity of the 220 cm^{-1} peak in all PF samples thus reflects a net reduction in the number of these short anti-planar alkyl segments. We speculate that side chain crystallization occurs best in the $CHCl_3$ sample. A direct consequence is that the K1 phase is retained longer upon heating and samples having this characteristic show preferential ordering to the α′ polymorph.

Thermal cycling from the n-LC mesophase yields an irreversible loss in the intensity of this 220 cm^{-1} peak and, concomitantly, an increase in intensity at 150 cm^{-1}. This Raman shift corresponds to the LAM1 mode and the relative strengthening of this peak may be identified with a net increase in the proportion of all-anti alkyl chains. We discuss this in more details in section 6.3.3.

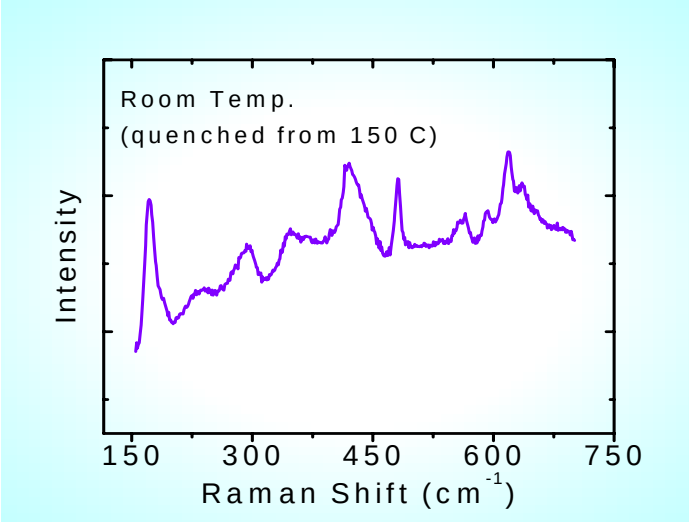

Figure (6.6): Raman spectrum of p-xylene cast sample at room temperature quenched from n-LC phase.

The *p*-xylene sample has a high fraction of C_β chromophores at the onset. Upon thermal cycling from the *n*-LC phase, the Raman band at 370 cm^{-1} is clearly seen. Additionally, there is an enhancement of the 150 cm^{-1} peak. These changes correlate with

the overall crystalline phase, where the sample is in "M" state, which precludes the presence of β conformers. The quenched sample does not show any signature of the LAM3 mode, suggesting suppression of polymer crystallization as shown in Fig. 6.6.

The 600 cm^{-1} region is also highly temperature sensitive in all three samples, especially the *p*-xylene cast sample. The peak broadens upon heating to ~110°C; a temperature correlated with the cold crystallization to the partially ordered K1 state. The 600 cm^{-1} region is characterized by two dominant peaks, near 620 and 633 cm^{-1}, as shown by the arrows in Fig. 6.7

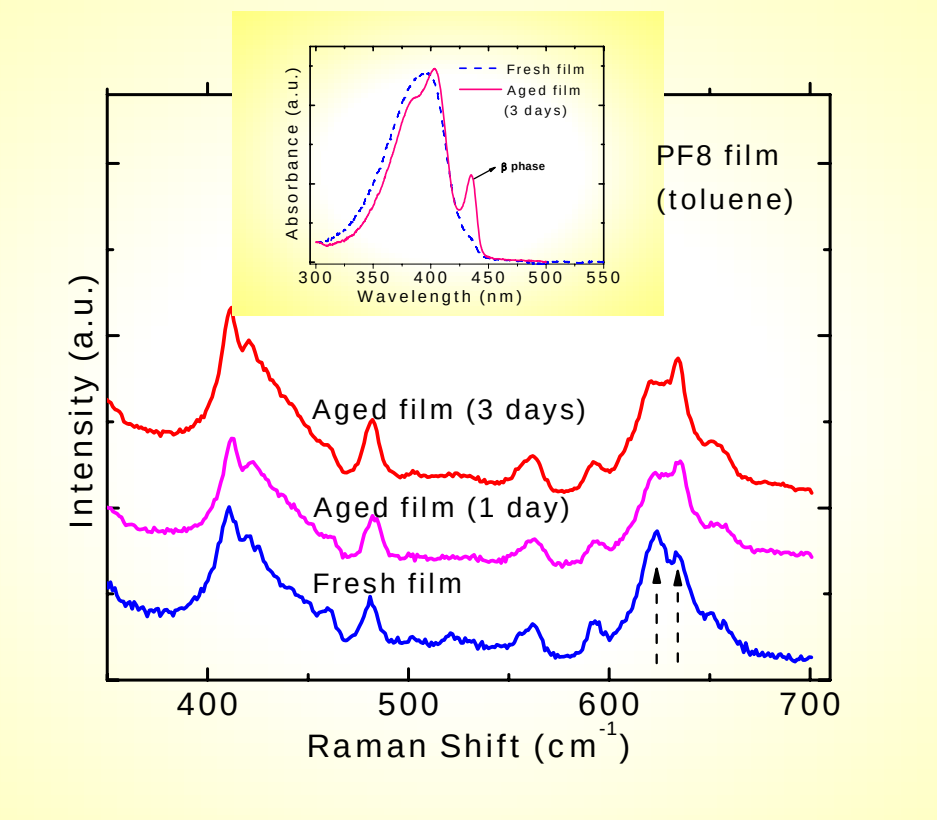

Figure (6.7): Raman spectra of a PF8 film cast from toluene. The films were aged in toluene vapor. The inset shows the absorption spectra from the same films.

Since the PF8 has a mixture of various side chain conformers both peaks in the 600 cm^{-1} region are observed for all crystalline phases. It is mainly the ratio of the relative intensities of these two peaks that change as the polymer goes through various changes in its conformation. The relative ratio of the intensities of the peaks at 620 and 633 cm^{-1} track the presence of the β phase. This can be clearly seen in Fig. 6.7 which is from a PF8 film cast from toluene, where simultaneous optical absorption and Raman spectra were measured. Fresh spin cast PF8 film exhibits only a small fraction of the β phase, as evident from the absorption spectrum (inset, Fig.6.7). Correspondingly, the 620 cm^{-1} Raman peak is higher in intensity. Aging PF8 in toluene vapor is known to enhance the fraction of C_β chromophore.[10] This is clearly seen as a red shift in the absorption spectrum with the appearance of the 435 nm peak. The Raman spectrum shows an enhancement of the 633 cm^{-1} peak with the evolution of the β phase.

In light of this the *p*-xylene sample (Fig. 6.3) has a large fraction of β phase at the onset. The 633 cm^{-1} peak is stronger compared to the 620 cm^{-1} peak, consistent with a higher fraction of *a-g-g* type conformer which is a prerequisite for the β phase. Upon annealing (when PF8 is in M phase) the 633 cm^{-1} peak substantially decreases in intensity indicating a loss in the *a-g-g* type chain conformers. The side chain conformations (*a-a-a* and *a-g-g*) of PF8 will be discussed in section 6.3.3.

(b) Medium frequency region (700-1100 cm^{-1})

The Fig. 6.8 shows the Raman spectra of *p*-xylene, $CHCl_3$ and Cl-φ cast PF8 powder in the 700-1000 cm^{-1} range (a-c) at selected temperatures, where the topmost 25^oC spectrum refers to the thermally cycled sample; (d) shows the Raman spectrum from a thin PF8 film cast from toluene.

The Raman band at 735 cm^{-1} which is due to ring breathing mode also exhibits a similar irreversibility. We note that the symmetry of the chain is reduced with the presence of the β chromophore. A doublet appears at the 735 cm^{-1} Raman peak in all samples at the onset, in correspondence with the high fraction of the β phase initially present. Upon warming to the n-LC state the doublet evolves into a single peak and then remains this way after cooling to room temperature. This is seen in figure (6.8) for the bulk, as-cast samples, and additionally a thin film sample.

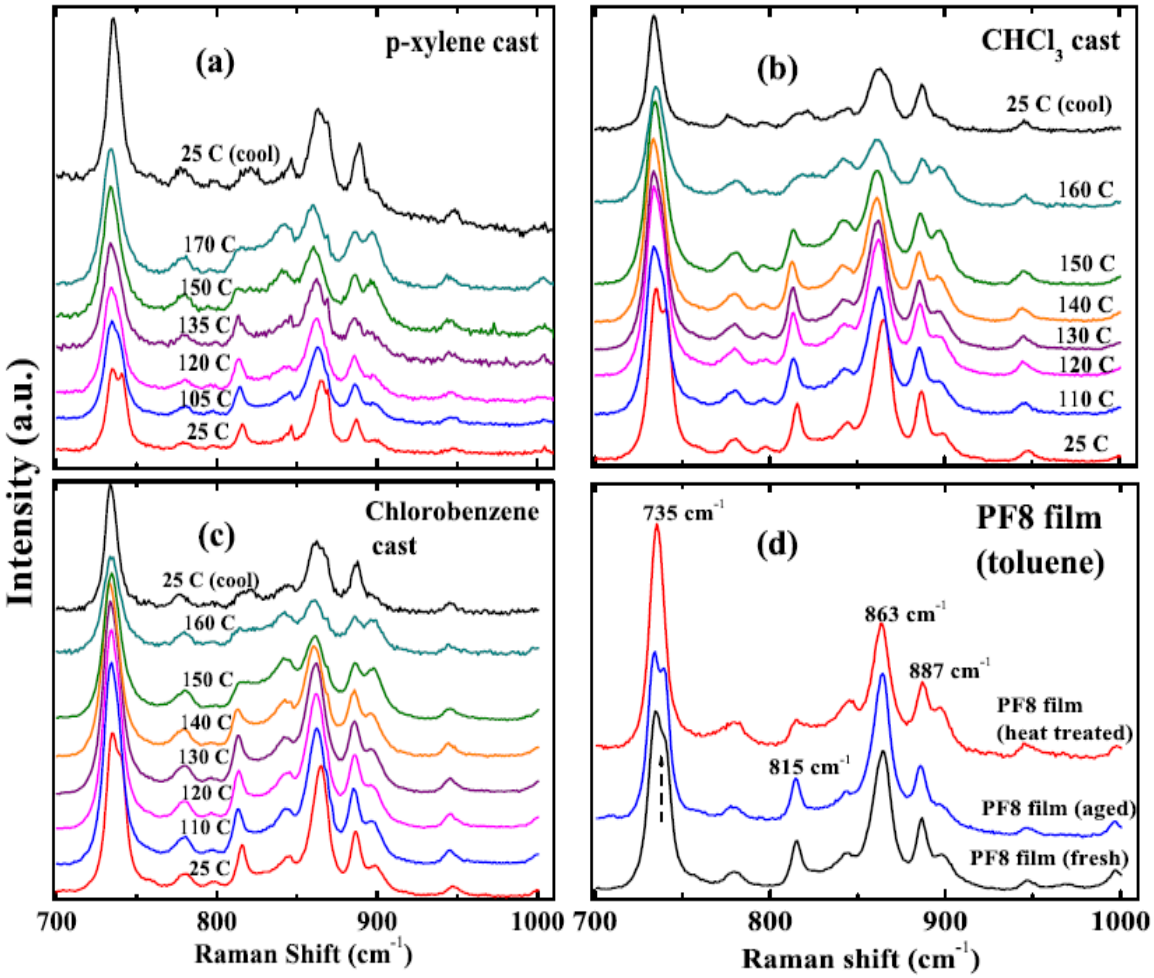

Figure (6.8): Raman spectra of *p*-xylene, $CHCl_3$ and Cl-φ cast PF8 powder in the 700-1000 cm^{-1} range.

Weaker peaks at 815 cm^{-1} and two near 900 cm^{-1}, exhibit sensitivity during heating to the n-LC phase as well [see Fig. (6.8)]. The 815 cm^{-1} band begins to diminish by 140^{o}C in the *p*-xylene sample whereas in the $CHCl_3$ and Cl-φ samples this drop occurs at slightly higher temperatures. We mention that this peak is completely absent in the PF2/6 Raman spectra. Raman peaks in this vicinity arise from the alkyl side chain motions. In n-alkanes the 890 cm^{-1} frequency corresponds to the CH_3 deformation mode and is observed in both Raman and IR spectra.[11]

The ratio of the 890 cm^{-1} to the 900 cm^{-1} peak intensity changes with increasing temperature in PF8 unlike in PF2/6 where the ratio remains a constant throughout thermal cycling. In the three bulk samples (*p*-xylene, $CHCl_3$ and Cl-φ cast PF8) the 900 cm^{-1} peak smoothly gains intensity relative to the 890 cm^{-1} peak on heating to the n-LC phase. Again, after cooling the samples back to room temperature, the 900 cm^{-1} peak loses almost all its intensity. We attribute the 900 cm^{-1} peak to end-gauche type conformers; this typically appears at a slightly higher frequency in n-alkanes.[12]

All C-H modes in the vicinity of 1100 cm^{-1} (from PF8 samples) are temperature sensitive. The 1171 cm^{-1} peak diminishes on heating and becomes unobservable after reaching the n-LC phase. This is shown in figure (6.9-a) for the $CHCl_3$ cast sample. This peak recovers upon returning to room temperature but with evidences of two broad constituents. All PF8 samples, regardless of the solvent used, display the same trend. Additionally, we find that the broadening of the 1135 cm^{-1} peak closely reflects the crystallographic variations.

Figure 6.9 (b-d) plots the full width at half maximum (FWHM) of the 1135 cm^{-1} peak as a function of temperature for the three bulk PF8 samples. They all show a similar

trend: between 70-100°C the FWHM of the 1135 cm^{-1} peak hardly changes despite the onset of cold crystallization and, at higher temperatures, this peak broadens until reaching the n-LC phase. There are sample specific variations in this broadening. For example, in the *p*-xylene cast sample a strong discontinuity is observed in temperature range of 120°C to 140°C. This unique feature appears correlated with the appearance of C_γ type emission in PL and PLE. The broadening occurs more slowly in the other two cases (and also tracks the onset of C_γ type emission in these samples). Upon cooling from 170°C, the FWHM of the 1135 cm^{-1} peak decreases linearly. This effect is associated with a decrease in the intermolecular distance due to thermal contraction (yielding an M-type phase) and, correspondingly, an increase in the intermolecular and intramolecular quasi-elastic constants of this more ordered state.[13]

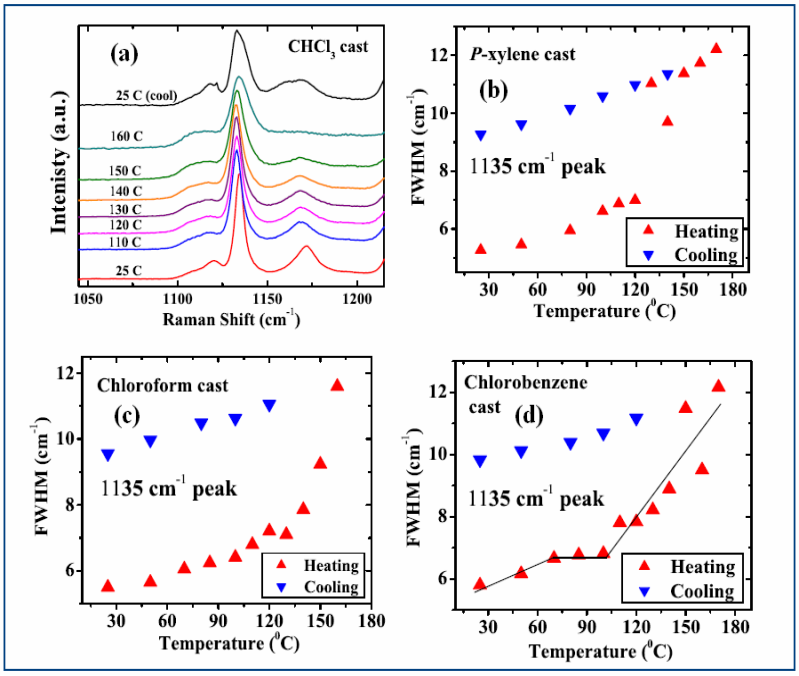

Figure(6.9): FWHM of the 1135 cm^{-1} upon heating and cooling for the three samples casted from p-xylene, $CHCl_3$ and Cl-φ (b-d).(a) shows the Raman spectra of the $CHCl_3$ sample at selected temperatures in the 1100 cm^{-1} region.

(C) High frequency regions (1100-1700 cm^{-1})

The Raman spectrum in the high frequency region 1100-1700 cm^{-1} is shown in Fig. 6.10.

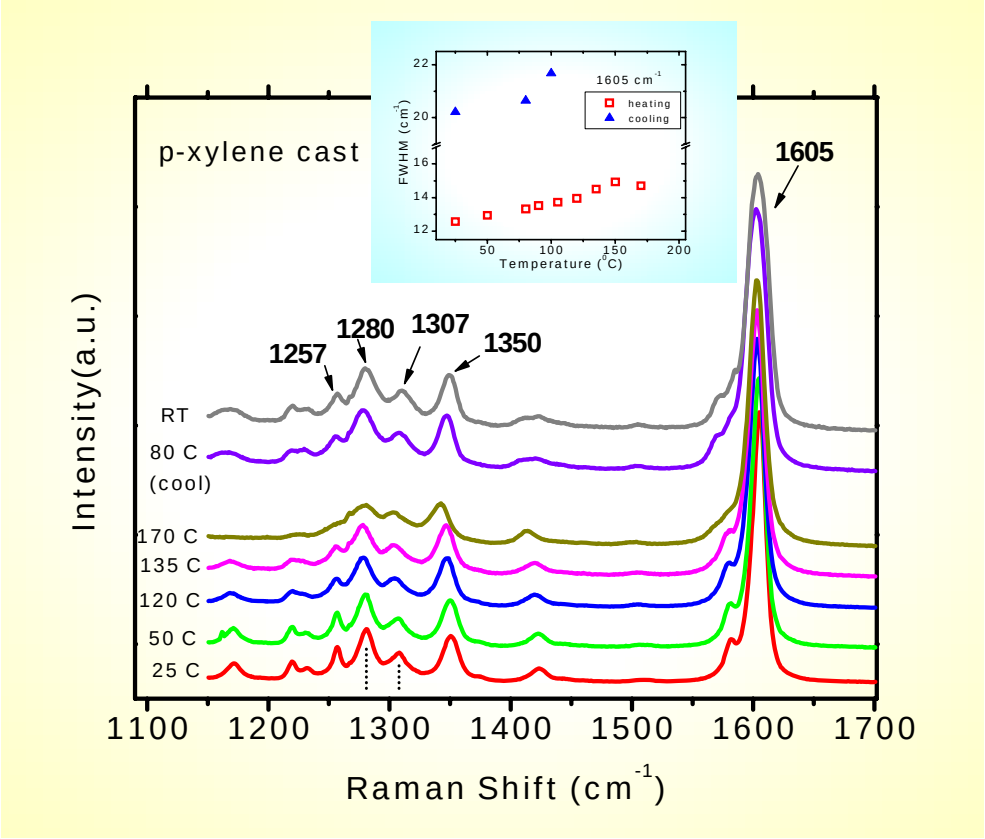

Figure (6.10): Raman spectra of p-xylene cast PF8 sample at selected temperatures. The top two spectra were measured during the cooling cycle. Inset shows the full width half maximum of the 1605 cm^{-1} Raman peak both during the heating and cooling cycle.

The Raman intensity centered near 1600 cm^{-1} arises from an intra-ring C-C stretch mode and is best fit assuming multiple peaks: an overwhelmingly dominant peak at 1605 cm^{-1} and at least one or two weak peaks in the vicinity of 1570-1600 cm^{-1}. The Raman frequencies in the 1250-1350 cm^{-1} region are mainly associated with the backbone C-C stretch modes; the 1307 cm^{-1} peak represents the C-C stretch mode between adjacent

monomer units and the higher frequency peak at 1350 cm^{-1} corresponds to the C-C stretch mode from within the monomer unit.

The C-C stretch mode between adjacent monomers split into two bands, appearing at 1280 and 1307 cm^{-1}, and are shown by dotted lines. Frequencies in the 1100-1200 cm^{-1} region (in figure 6.2) are sensitive to side-group substitution; the 1120 and 1135 cm^{-1} peaks mainly arise from the C-H bending modes (either local or between phenyl units). The 1257 cm^{-1} corresponds to a C-H bend type motion and its intensity depends upon the backbone torsional angle.[14] The weak peak at 1420 cm^{-1} corresponds to a combined C-H bend and C-C stretch between adjacent monomers.

The 1600 cm^{-1} broadens significantly upon crystallization of PF8 (inset Fig. 6.10). At the onset the FWHM of the peak is 12 cm^{-1} which in the annealed sample goes up to 20 cm^{-1}. Theoretical gas phase calculations unfortunately do not track this as a function of the torsional angle, suggesting that the broadening observed in the experiment is a consequence of the changing intermolecular and intramolecular force constant when the polymer is in the M phase.

Both solvent and thermal history plays a role in determining the crystalline phases in PF8. From the above discussion of Raman scattering, it is seen that PF8 samples cast from various solvents appear in a metastable structure at room temperature, which is comparable to that of recent work of XRD.[8] The progression towards the well-ordered α crystal phase is extremely variable; PF8 cast from *p*-xylene is marked by the M phase at RT when cooled slowly. This phase is intermediate between the α and α' and presumably corresponds to the C_γ type family.

6.3.3 Comparison of experiment with theoretical modeling

Theoretical Raman spectra of the fluorene oligomers were performed using hybrid density-functional theory in the GAUSSIAN03 program.[15] Details of our computational methods is found in Ref.[16] The Raman frequencies were calculated from fluorene monomers for two limiting conformations of the *n*-octyl side chains: an all *anti*-alkyl side chain (*a*-*a*-*a*) and an *anti*-*gauche*-*gauche* (*a*-*g*-*g*) side chain conformation Fig.6.11.

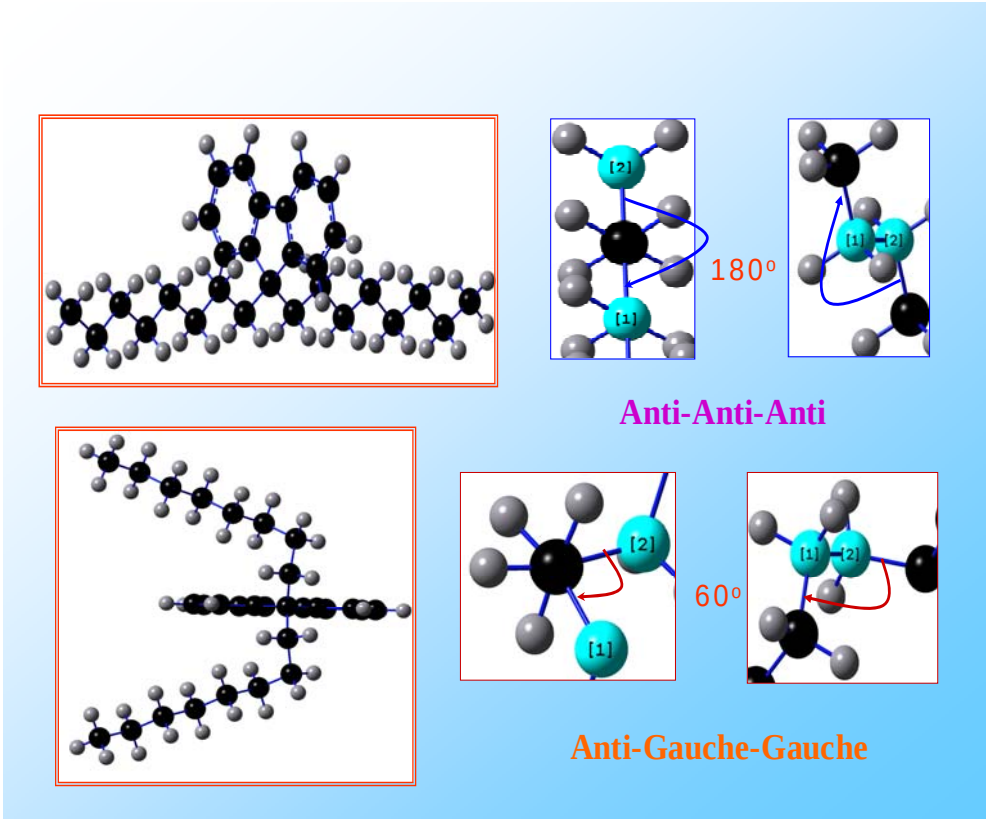

Figure (6.11): Two different side chain conformations of PF8 [Courtesy C. Volz].

Vibrational frequencies of a fluorene dimmer and trimer (with no side chain substitution) were calculated by varying the torsional angle between the monomers as test cases for conformational isomers of PF8. All calculated frequencies reported here are unscaled, normalized to the C-C intraring stretch frequency at 1600 cm^{-1}, and have been

broadened with a Lorentzian line shape of full width at half maximum (FWHM) of 10 cm^{-1}.

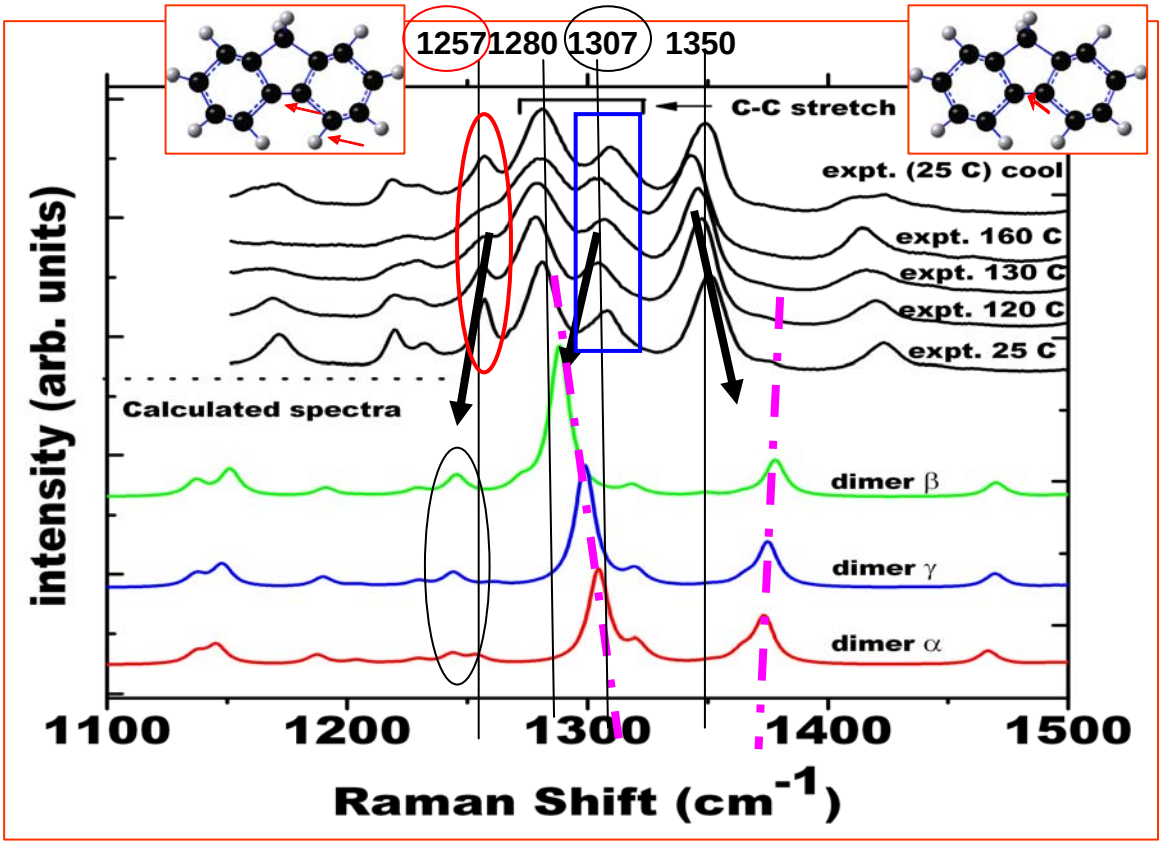

Figure (6.12): Comparison of experimental and calculated Raman spectra.

Fig.6.12 shows the experimental Raman spectra of PF8 at different temperatures. The top spectrum taken at RT after cooling the sample from the *n*-LC phase is representative of the α crystalline phase. The 1257 and 1280 cm^{-1} peaks originate from a combination of C-H bending and C-C stretching motion of the bond connecting the two phenyl rings within the monomer. The intensity of the 1257 cm^{-1} peak is highly sensitive to temperature and tracks the transformation of C_β chromophore.

The 1200-1400 cm^{-1} region is very sensitive to the backbone torsion angles and thus changes in the Raman spectrum in this region represent the conformational isomers. The C-C stretch mode between monomers split into two peaks at 1280 cm^{-1} and 1307 cm^{-1} in PF8. The peak position of the latter, in particular, tracks the changes in the C_β chromophore upon annealing. In Fig. 6.12 the bottom three spectrum shows our calculated Raman spectra for optimized dimmer with varying torsion angles ($C_{\alpha,}$ C_β, and $C_{\gamma,}$ isomers). The C-C stretch mode between the adjacent monomers (~1307 cm^{-1}) softens by almost 16 cm^{-1} for the C_β dimmer. We point out that the C_β conformer has a torsional angle of 165^o; hence, we expect a smaller shift in the Raman frequency from the C_β to the C_α or C_γ conformers compared to our theoretical calculations where the β phase was held at 180^o.

The as-is PF8 sample has a high fraction of the C_β conformer, which was ascertained by the presence of the 438 nm peak in the absorption spectrum of a thin film of the sample. In Fig. 6.13 the peak position of the 1307 cm^{-1} as a function of heating and cooling shows that with increasing temperatures the Raman frequency positions typically decreases due to a decrease in the intermolecular and intramolecular quasielastic force constants. A striking feature is the enhancement of the frequency position of this peak by more than 3 cm^{-1} at 130^{o}C. This reflects a transformation of the C_β conformers to the C_α and C_γ conformers, consistent with the theoretical calculations where the 1307 cm^{-1} peak position is significantly enhanced for the α conformer compared to the planar β conformer in a dimer or trimer. (Fig. 6.12 shows only for dimer).

Upon cooling one observes a linear increase in the frequency positions, typically observed in crystalline solids. Owing to a long-range three-dimensional ordering,

hardening of frequencies in PF8 upon cooling reflects the contraction of the ordered (semi) crystalline phase.

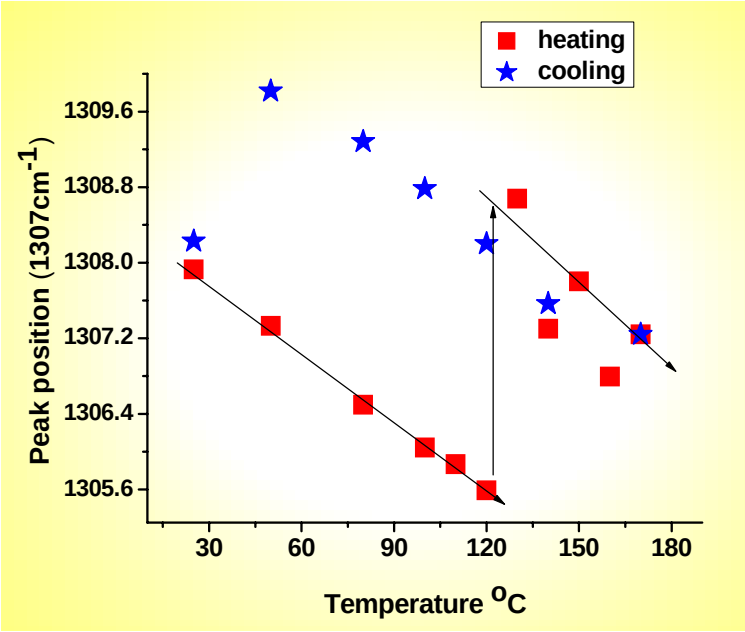

Figure (6.13): the peak position of the 1307 cm^{-1} as a function of heating and cooling.

Additionally, the 1307 cm^{-1} appears at a slightly higher frequency upon cooling it back to room temperature [Fig. 6.13] consistent with our calculations where the C_γ chromophore has a higher frequency compared to C_β.

The 1257 cm^{-1} peak is highly sensitive to temperature, which is again a manifestation of transformation of the conformers. The peak intensity is normalized to the 1600 cm^{-1} peak (I_{1257}/I_{1600}); this ratio decreases with increasing temperatures and upon cooling the sample back to RT, the intensity is ~ 26% less compared to the as-is sample, shown in Fig. 6.14. Our calculated I_{1257}/I_{1600} ratio in the dimer and trimer (Fig. 6.15) as a function of the torsional angles shows a similar trend; a 30%-35% difference is observed between the C_γ and C_β chromophore.

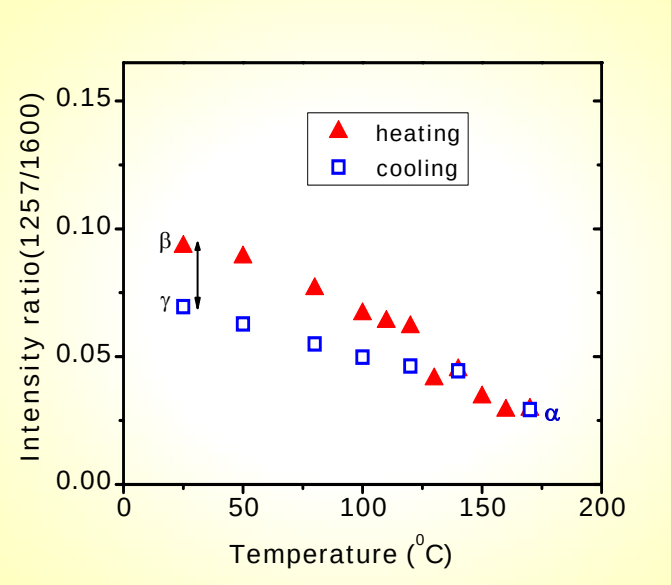

Figure (6.14): Intensity ratio of the 1257 cm^{-1} to the 1600 cm^{-1} peak vs temperature both during the heating and cooling cycle.

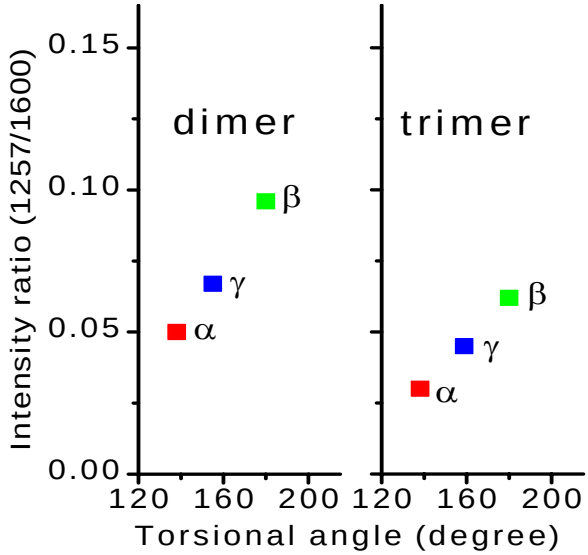

Figure (6.15): calculated I_{1257}/I_{1600} ratio of a dimer and a trimer for varying torsional angles. [Courtesy C. Volz]

The experimental result is interpreted as a transformation of the C_β chromophore to C_γ or C_α upon heating the sample. Upon cooling, the polymer chains most probably have

a large fraction of the C_γ chromophore observed from the experimental and calculated I_{1257}/I_{1600} ratio.

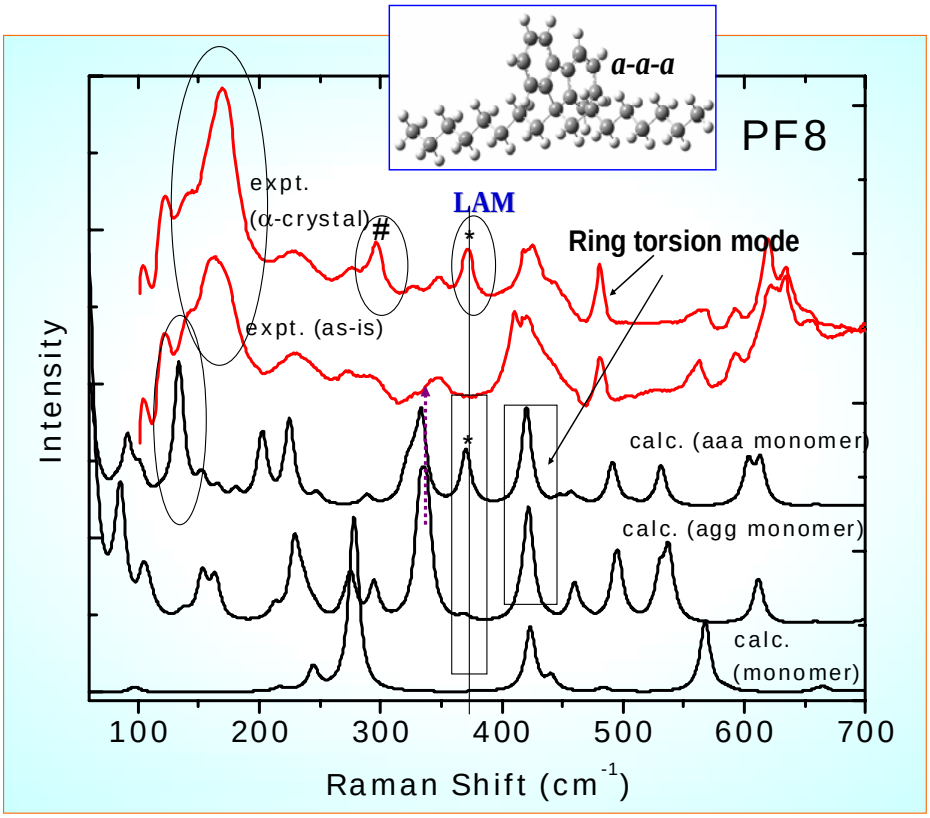

Figure (6.16): Raman spectra of as-is and α crystalline PF8 in the low frequency region (top two). The bottom three spectra are the calculated Raman spectra of a fluorene monomer, and fluorine monomer with *a-g-g* and all *a-a-a* chain conformations. (inset shows the monomer with *a-a-a* conformation).

Side chain conformation as a function of the crystalline phase can be further probed by studying the low frequency region (100–700 cm^{-1}) of the Raman spectra. Fig. 6.16 (top two spectra) shows the experimental Raman spectra of the as-is and the α crystalline sample (thermally cycled) of PF8 in the low frequency region. The bottom three is the

theoretically calculated spectra of fluorene monomer and fluorene monomer with *a-a-a* and *a-g-g* side chain conformation.

The 420 cm^{-1} peak observed in the calculations is the ring torsional mode (as deciphered from the displacement pattern), which is observed at a slightly higher frequency ~ 480 cm^{-1} in the polymer. This peak is seen at 480 cm^{-1} in all PFs with varying side chains and is almost temperature insensitive, making it a viable candidate for the ring torsional mode. Strong LAM (longitudinal accordion motion) modes in *anti* planar *n*-alkanes occur at low frequencies; in nonadecane LAM1 and LAM3 modes appear at 125 and 342 cm^{-1}, respectively.[11] The calculated spectrum of the *a-a-a* conformer clearly shows the LAM3 mode at 370 cm^{-1}, which is totally absent in the *a-g-g* conformer. The appearance of the 370 cm^{-1} peak and the enhancement of the 150 cm^{-1} region in the α crystalline phase of PF8 is a clear indication of all *anti* conformation of the alkyl side chain in this phase. These results establish a connection between side chain ordering and the local conformations.

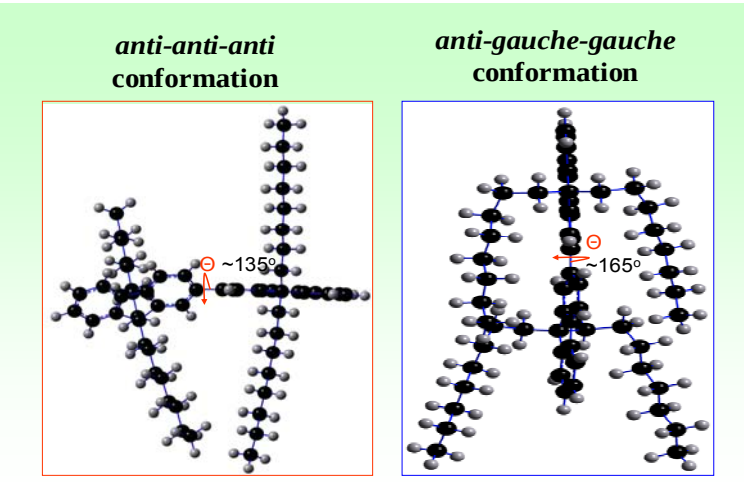

Figure (6.17): Coformations in PF8, an all *anti*-alkyl side chain (*a-a-a*) (left) and an *anti-gauche-gauche* (*a-g-g*) side chain conformation (right) [Courtesy C. Volz].

The work by Chunwaschirasiri *et al.*[17] shows that the presence of the C_β conformer is possible only when the alkyl side chains adopt an *a-g-g* type conformation. Based on this and from theoretical vibrational spectra calculations, we now have an insight as to why the β phase is incompatible with the α crystalline phase. This is a direct consequence of the conformation of the alkyl side chains, which adopts an *a-a-a* conformation in the α crystalline phase of PF8.

In conclusion, we have shown experimental evidence of the incompatibility of the C_β chromophore with the overall α crystalline phase in PF8. This is attributed to a large scale increase in the population of *anti* planar conformation of the alkyl side chains. These studies were based on a combined theoretical vibrational spectra calculations of single chains in conjunction with experimental Raman scattering studies. Such studies are an important step towards developing a universal picture of structure-property relationship in CP that mainly derives from chain morphology at short length scale.

References:

[1] U. Scherf and E. J. W. List, Adv. Mater., (Weinheim, Ger.) **14**, 477 (2002).

[2] D. Neher, Macromolecule. Rapid commun., **22**, 1365 (2001).

[3] M. Grell, D.D.C. Bradley, X. Long, T. Chamberlin, M. Inbasekaran, E.Woo, M. Soliman, Acta polym., **49**, 439 (1998).

[4] B. Tanto, S. Guha, C. Martin, U. Scherf, M. J. Winokur, Macromolecules, **37**, 9438 (2004).

[5] G. Lieser, M. Oda, T. Miteva, A. Meisel, H. G. Nothofer, U. Scherf, Macromolecules , **33**, 4490 (2000).

[6] H. Liem, P. Etchegoin, K. S. Whitehead, D. D. C. Bradley, J. Appl. Phys, **92**, 1154 (2002).

[7] M. Ariu, D.G. Lidzey, D.D.C. Bradley, Synth. Mat., **111**, 607 (2000).

[8] B. Tanto, S. Guha, M. Arif, and M.J. Winokur, unpublished.

[9] R. G. Snyder, J. Chem. Phys., **76**, 3921 (1982).

[10] H. Cheun, B. Tanto, W. Chunwaschirasiri, B. Larson, and M.J. Winokur, Appl. Phys. Lett., **84**, 22 (2004).

[11] G. Zerbi, and R. Magni, M. Gussoni,; K. H. Moritz, A. Bigotto, J. Chem. Phys., **75**, 3175 (1981).

[12] M. Maroncelli,, and S. P. Qi, H. L. Strauss, R. G. Snyder, J. Am. Chem. Soc., **104**, 6237 (1982).

[13] Bar-Cohen, Y. Keter, "Raman Spectra of Molecules and Crystals." , New York, (1972).

[14] M. Arif, C. Volz, and S. Guha, Phys. Rev. Lett., **96**, 025503 (2006).

[15] GAUSSIAN03, Gaussian, Inc., Pittsburgh, PA, (2003).

[16] C. Volz, M. Arif, and S. Guha**,** The Journal of Chemical Physics **126**, 064905 (2007)

[17] W. Chunwaschirasiri, B. Tanto, D. L. Huber, and M. J.Winokur, Phys. Rev. Lett., **94**, 107402 (2005).

CHAPTER 7

OLED structures: electronic spectroscopy and current-voltage characterization

7.1 Device fabrication process

A key issue in fabricating OLEDs on transparent substrates like glass or plastic is how to protect them from moisture and oxygen. Since the whole device fabrication process involves techniques like shadow masking, ITO patterning, substrate cleaning, spin coating, and thermal evaporation, care should be taken at every single step of device fabrication. The basic requirements for making good OLEDs are: first, a high level of impermeability is needed because organic polymers are very sensitive to moisture and oxygen; second, the deposition temperature must be low because OLEDs cannot withstand high temperatures. In the next section we discuss our fabrication process.

7.1.1 Steps involved in device preparation

The steps involved in making high-quality OLEDs are: (1) cleaning of glass slides; (2) pattering ITO substrates; (3) cleaning of ITO coated substrate; (4) spin coating of polymer layer; (5) deposition of top metal contacts and (6) encapsulation of the final device.

(1) Cleaning glass slides

(a) The glass substrates were cut in 1in.x1in. dimension. To clean dirt and residue on glass slides a bath of soapy water was prepared and then using lint-free wipe and

cotton swab the glass slides were gently rubbed on the surface. They were then rinsed thoroughly in DI water and blow dried with nitrogen.

(b) The glass slides were then solvent cleaned using acetone. Solvent can clean oils and organic residues which appear on glass surfaces. But sometimes solvent like acetone leave their own residue, due to which they have to be cleaned with aqua regia solution.

(c) Aqua regia solution was prepared as HCl : HNO_3 : H_2O = 3:1:3 and then diluted 5-10 times by adding DI water. The glass slides were then dipped in diluted aqua regia solution for few hours.

(d) Finally the glass slides were rinsed in DI water and then blow dried with nitrogen gas.

(2) Creation of Patterned ITO substrates

After cleaning glass slides, Indium-tin-oxide (ITO) was deposited on top of cleaned glass substrate using pulsed laser deposition (PLD) or sputtering. The schematic of the PLD system is shown in Fig. 7.1. For patterning ITO a (1 in. x 1 in.) shadow mask was used. The shadow mask contains 5 strips (two of them are 100 μm and three of them are 200 μm widths).

An ITO target was loaded inside the vacuum deposition chamber which was ablated using a KrF (248 nm) excimer laser. The cleaned glass slide was used as the substrate. The beam was then focused on to the target with a certain angle of incidence forming a plume. The laser, operated at a pulse rate of 20Hz, and produced an energy of 300 mJ. Films were grown from 15000 laser beam shots in complete vacuum with base pressure of 10^{-2} to 10^{-5} Torr in an oxygen environment with a substrate temperature of 100-400^{o}C. Patterned ITO was also deposited on cleaned quartz and glass slides using sputtered

deposition. Deposition parameter that was used for ITO growth is: Temperature 400^{o}C, Gas flow: O_2 =10 sccm, Ar =20 sccm, Pressure 4 mtorr, Power 200 Watt, and Deposition time = 20 mins.

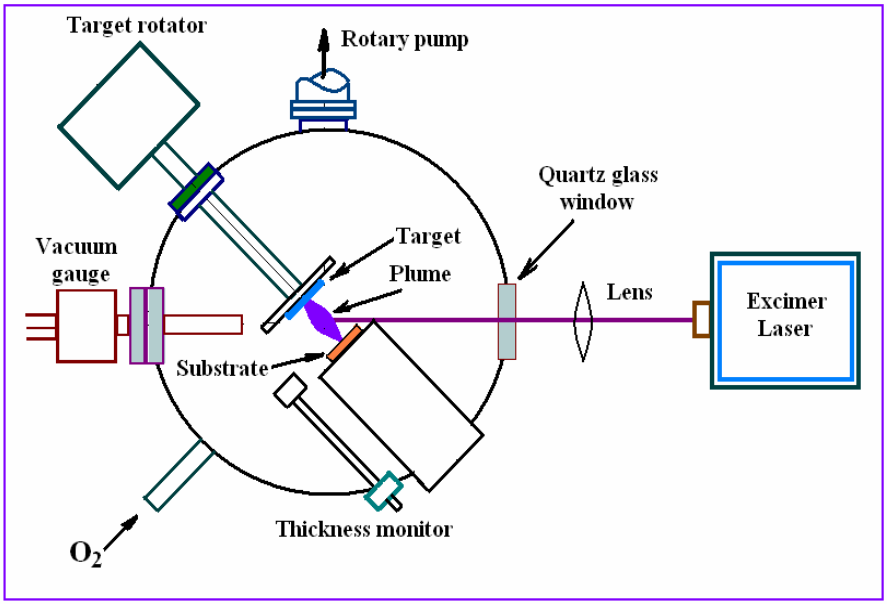

Figure (7.1): Pulsed laser deposition system [system in Missouri State University].

(3) Cleaning of ITO coated substrate

Since the ITO grown on glass surface is quite rough it requires partial etching to smooth down the surface. Figure 7.2 shows the AFM topography image of ITO surface grown by sputtering and pulsed laser deposition. The surface roughness for sputtered ITO was approximately 2nm and for PLD grown ITO was approximately1 nm.

(a) The resistivity of the ITO strip was first measured before cleaning. The non-ITO sides of glass slides were then marked. (b) For partial etching the patterned ITO samples were at first cleaned in a 1:10 aqua regia and water mixture for few minutes. The residue was then removed or diluted by rinsed DI water for 10 minutes. (c) The samples were then bathed in isopropanol for few seconds before ultrasonicating in acetone for 5

minutes. (d) Finally the samples were again bathed in isopropanol for 2 minutes and then blow dried and placed into plastic container inside the glove box. (The samples were handled with latex gloves during the whole cleaning process).

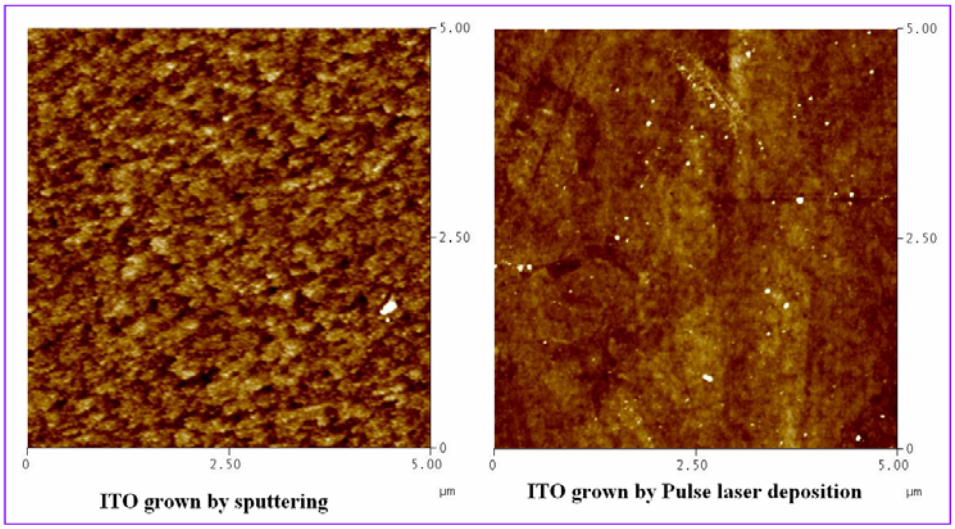

Figure (7.2): AFM image of surface spikes or roughness on ITO surface grown by sputtering and pulsed laser deposition.

(4) Spin coating of (PEDOT-PSS): Hole transport layer

PEDOT-PSS or (BAYTRON P-industrial name), an aqueous dispersions of the conductive polymer, poly(3,4-ethylenedioxythiophene)/poly(styrenesulfonate) with a solid content of approximately 1.5%- 2.5% was filtered twice to remove residual gel particles or dried particles using a syringe equipped with 0.45 µ 25 PVDF multi grade glass fiber filter before spin coating. PEDOT-PSS was then spin coated on cleaned ITO substrate using a spin coater inside the glove box.

Recipe: 0.5 ml solution was spin coated in (1 cm x 1cm) substrate area with (a) 250 rpm for 1 second; (b) 500 rpm for 1 second; (c) 4000 rpm for 30 second. This recipe

gives approximately 70-80 nm thick layers of PEDOT-PSS (measured using a Dektak surface profilometer). The PEDOT-PSS layer was then baked at 60-70^{o}C for 10 minutes in an oven positioned inside the glove box. Fig. 7.3 shows a schematic of the patterned ITO on a glass slides (left) and PEDOT-PSS spin coated on top of patterned ITO (right).

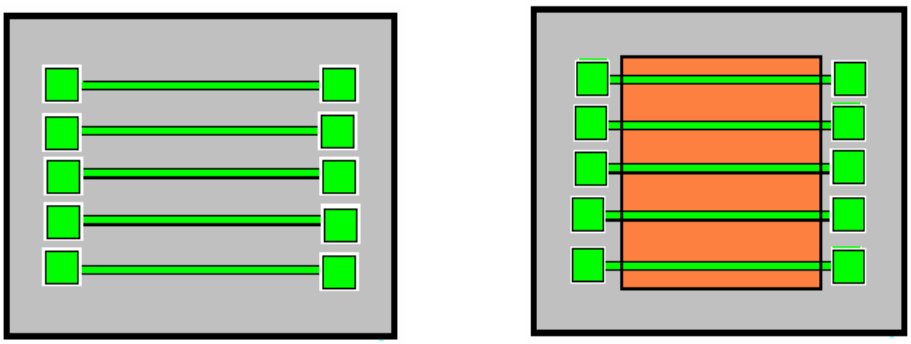

Figure (7.3): (Left) patterned ITO deposited on a glass substrate (Right) PEDOT-PSS deposited on top of ITO using spin coating.

(5) Spin Coating of PF layer

Fig. 7.4 shows a schematic of the spin coater system that was used for spin coating PEDOT-PSS and PFs. (a) The PF solution was at first prepared with a concentration of 10 mg in 1 ml of toluene solvent. (b) The solution was then filtered once with a Fisher brand 0.45 μm PTFE filter. (c) Approximately 6-8 drops of PF from a pipette was then spin coated on the area of the device (1 cm x 1cm) with spin speeds of 250 rpm for 1 sec; 500 rpm for 1 sec; and 2500 rpm for 30 sec. (d) The polymer layer was then baked in the oven at 60-75^{o}C for half an hour.

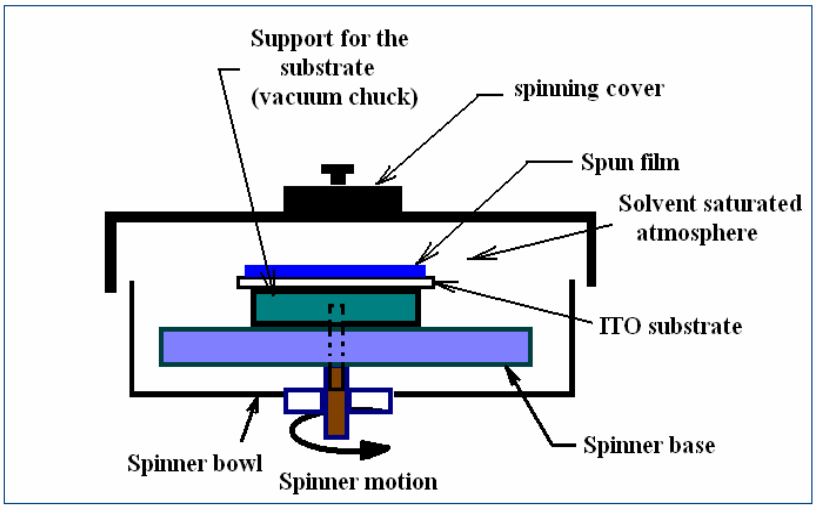

Figure (7.4): Spin coater system.

(6) Making top metal contact (using thermal evaporation)

Before making the top contact the spin coated sample was transferred to Box B of the glove box system (Fig. 3.13) where the thermal evaporation system is located. The top metal contact (Al or Ca) was deposited using a thermal evaporator with a shadow mask at a base pressure of 5-7 x 10^{-6} mbar using the same shadow mask that was used for the ITO growth. Fig. 7.5 shows the schematic of the metal deposition system located inside the glove box.

The basic metal growth procedure using thermal evaporation involves selecting an appropriate boat (for our device Al and Ca metal was used as source and tungsten boat for loading both metals) and then increasing the current driven through that boat slowly while monitoring the thickness. When a steady rate of 1-3 Angstroms/s was achieved, the substrate shutter was opened to start deposition. When desired thickness was achieved, the shutter was closed, and the source current was shut off. The growth of the next layer was then done without opening the chamber. The Ca layer was capped with Al to avoid

oxidation. Fig. 7.6 shows the subsequent steps in our OLED preparation: (left) schematic of the PF layer on PEDOT-PSS and (right) patterned metal layer on the polymer.

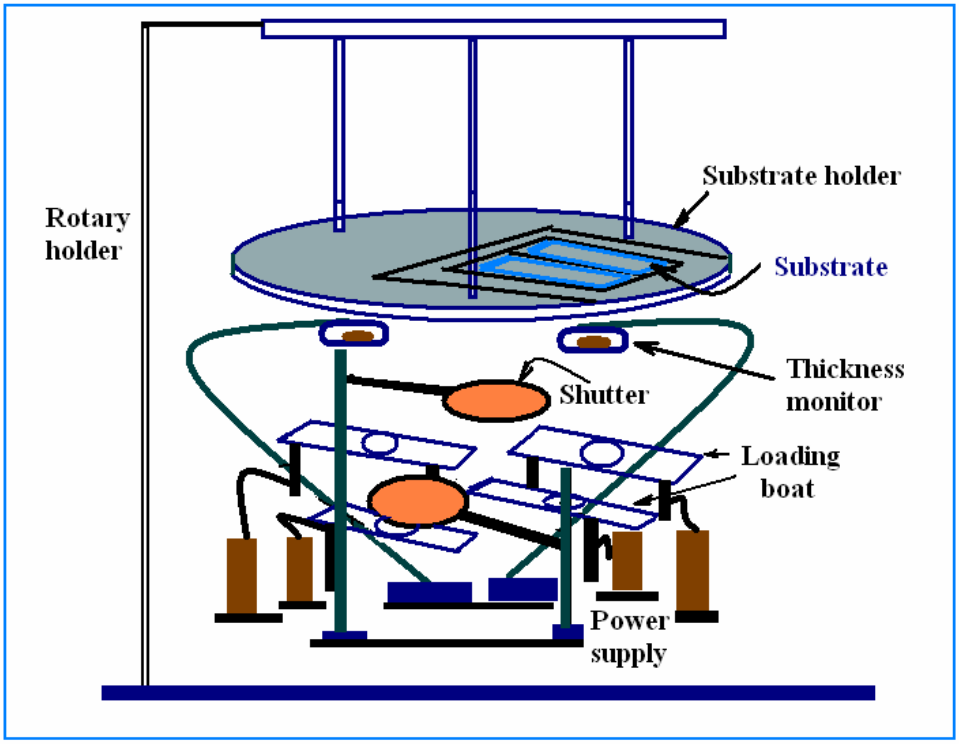

Figure (7.5): Schematic of metal deposition by thermal evaporation.

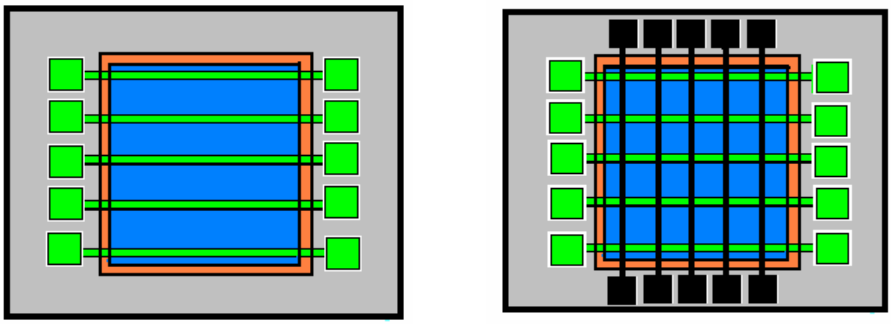

Figure (7.6): (Left) Polyfluorene (blue) deposited on top of PEDOT-PSS layer. (Right) Top metal contact (black) deposited on top of polymer layer as in pattern.

(7) Encapsulation of device

Before doing any characterization in air the devices were encapsulated with a cover glass to increase their longevity and enhance performance. A cover glass was at first cleaned and then epoxy (AC A1430-B, UV curable adhesive) was put around the edges. The cover glass was cleaned using the same cleaning procedure as our substrates. The cover glass with epoxy was then flipped and pressed carefully on the top of the device area to make sure that a complete seal is achieved. The sample is then placed under an ultraviolet curing lamp, which is turned on for 5-7 minutes to fully cure the epoxy. It is then removed from the nitrogen environment for all necessary characterization. Fig. 7.7 shows the photograph of the UV lamp and the sample underneath the UV lamp during the curing process of the epoxy. Since the shadow mask contains a total of five strips the whole sample contains 25 devices. Each cross section represents one device. The circle in Fig. 7.8 represents cross sectional view of each device structure. A flow diagram of the entire device fabrication process is shown in Fig. 7.9.

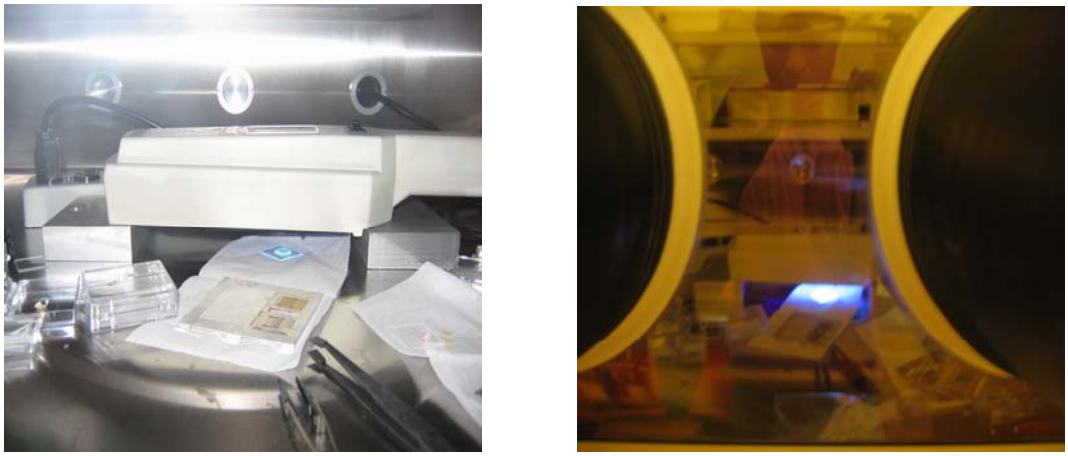

Figure (7.7): Encapsulation and curing of the device inside the glove box using UV lamp.

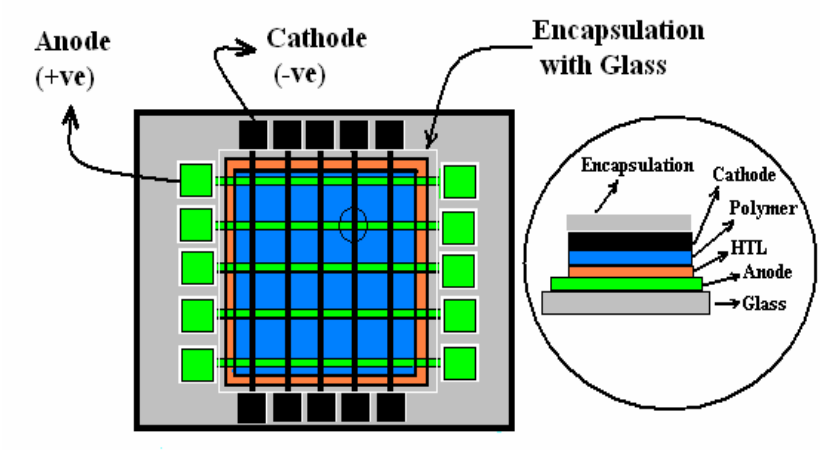

Figure (7.8): Encapsulated device structure of polyfluorene based LED.

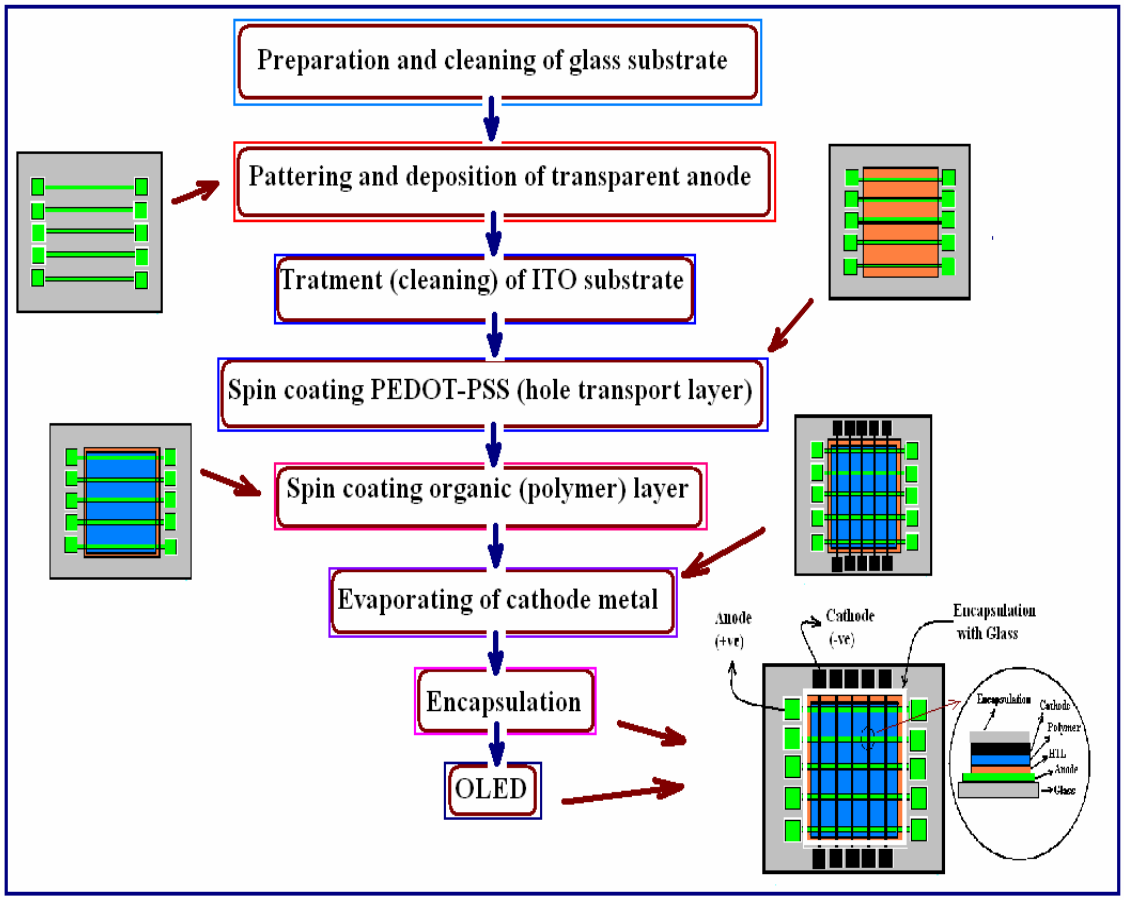

Figure (7.9): Flow diagram of the OLED fabrication process.

7.2 Emission characteristics of PF based LEDs

7.2.1 PL spectra measurements

PL measurements were carried out from our PF based LEDs. Fig. 7.10 shows the PL spectra at room temperature from PF2/6 and PF8 based LEDs with as-cast films. In both cases a distinctive Franck-Condon vibronic structure is resolved in the PL spectra, as indicated by the series of peaks corresponding to the singlet exciton decay with creation of zero (0-0) one (0-1) and (0-2) phonons.

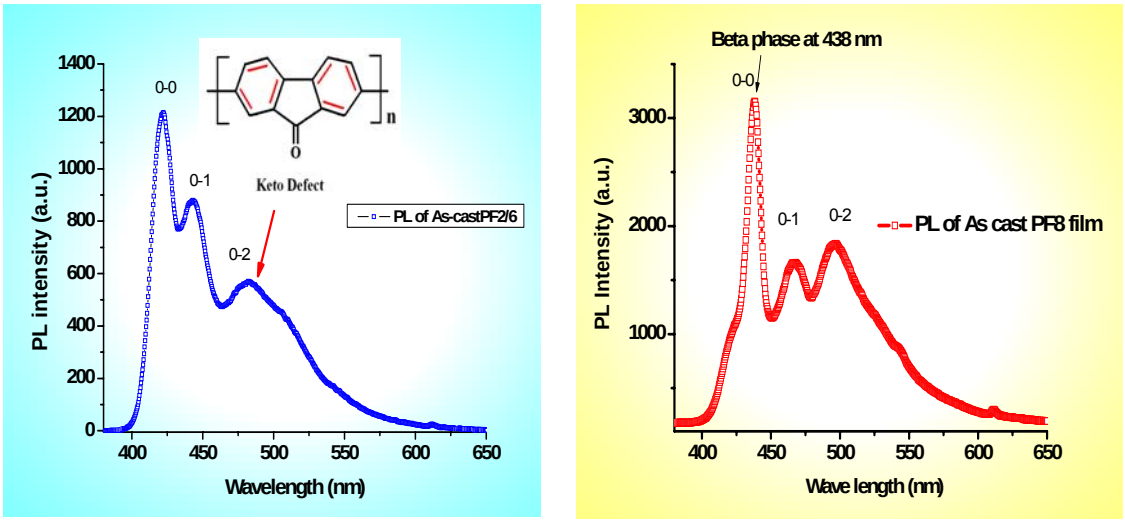

Figure (7.10): PL of as-cast PF 2/6 (left) and PF8 (right).

Although PFs show great promise as blue emitting materials in LEDs, many of the PF polymers developed, e.g., PF2/6, have suffered prominent spectral abnormality from an unwanted green emission band shown in Fig. 7.10 along with the desired blue emission. On the other hand, PF8 which has received extra attention because of its mesomorphic behavior and several crystalline phases show the signature of β phase at

438 nm. Suppression of the β form can be achieved in solvent casting e.g., from chloroform or by variations in the thermal processing like heat treatment or annealing at liquid crystallization temperature as described in the previous Raman scattering section. Fig. 7.11 shows the PL spectra of a PF8 film before and after annealing. It is clearly seen that the β phase disappears in the annealed sample.

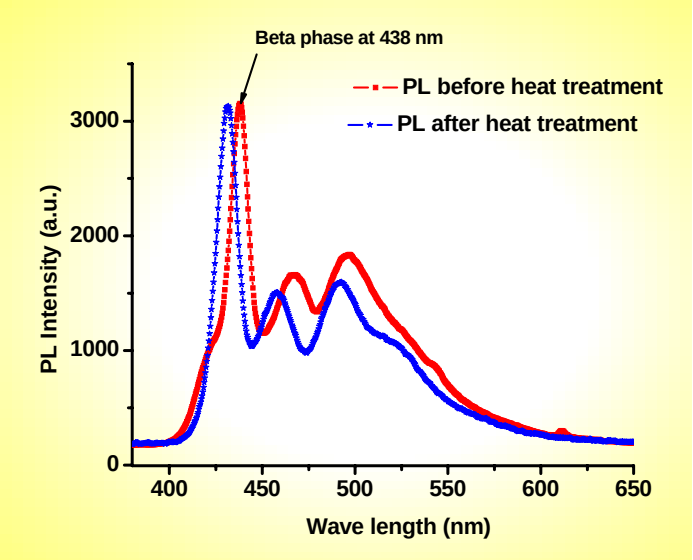

Figure (7.11): Photoluminescence of PF8 before and after heat treatment.

The optical properties of PF2/6 are relatively insensitive to the exact crystallographic state, thermal history, or molecular weight. Thermal cycling of PF2/6 does not show any significant changes in the PL spectra as shown in Fig. 7.12; variation in relative intensities is related to the thickness variation.

The next Fig. 7.13 shows the PL spectra from PF2/6-based LEDs fabricated inside the glove box and out side under ambient condition. Since the PL was measured from two different devices, the differences in the relative vibronic intensities seen in Fig. 7.13 most

probably arise due to difference in thickness of the film. By taking the relative ratio of the 0-0 to 0-1 peak intensity it is seen that the film prepared inside the glove box is thicker.

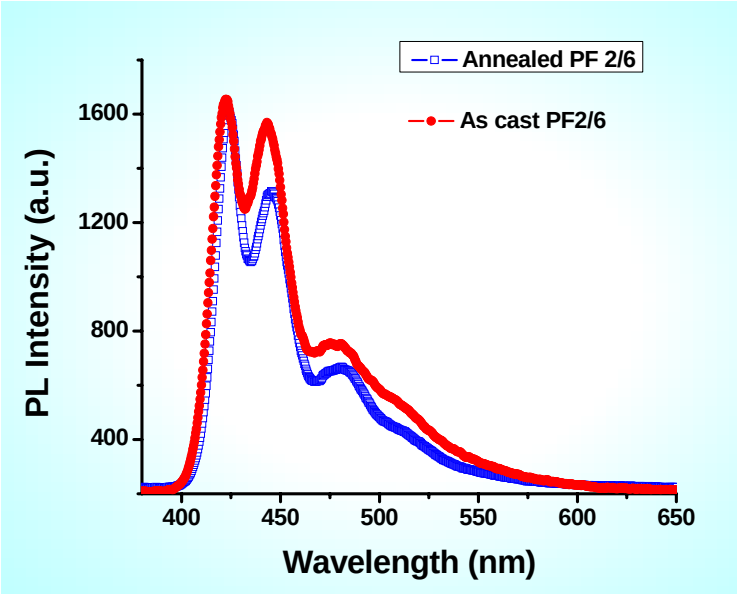

Figure (7.12): photoluminescence of As-cast film and annealed PF2/6.

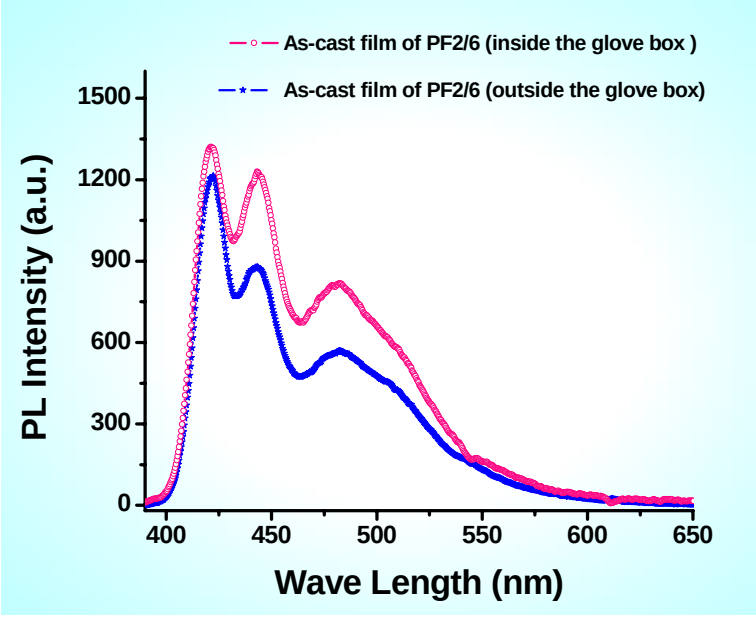

Figure (7.13): PL of As-cast PF2/6 film prepared inside and out side the glove box.

7.3.2 Electroluminescence and turn on voltage of LEDs

PF based LEDs were characterized using $I-V$ measurements to find out the turn on voltage for both PF8 and PF2/6, which are shown in figure 7.14 and 7.15.

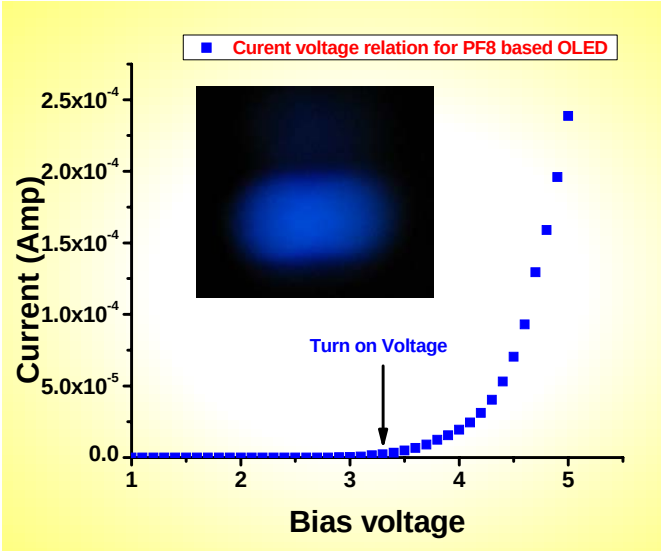

Figure (7.14): $I-V$ characterization of PF8 based light LED. (Inset is the light emission)

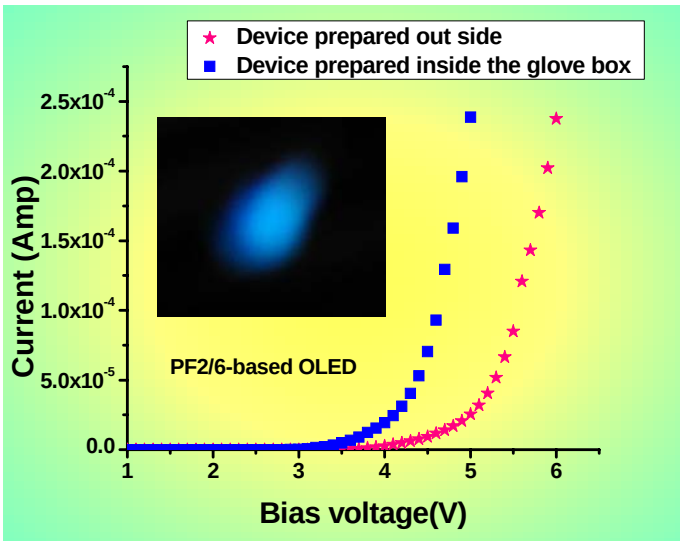

Figure (7.15): $I-V$ characterization of PF2/6 based LED prepared inside and outside the glove box. (Inset is the light emission from the device prepared inside)

EL results from the radiative decay of singlet excitons formed by a recombination of bound electron-hole pairs.[1,2] The EL spectra were measured from both PF8 and PF2/6-based LEDs. For PF8, two different types of LEDs were fabricated; one in which the PF8 film was cast from an as-is toluene based solution (slightly aged) and for the other, the spin coated film was thermally cycled. For the latter, the PF8 film was slowly heated in an oven to its *n-LC* temperature at ~160°C and then cooled back to RT before depositing the top Ca/Al electrode to induce the α crystalline phase.

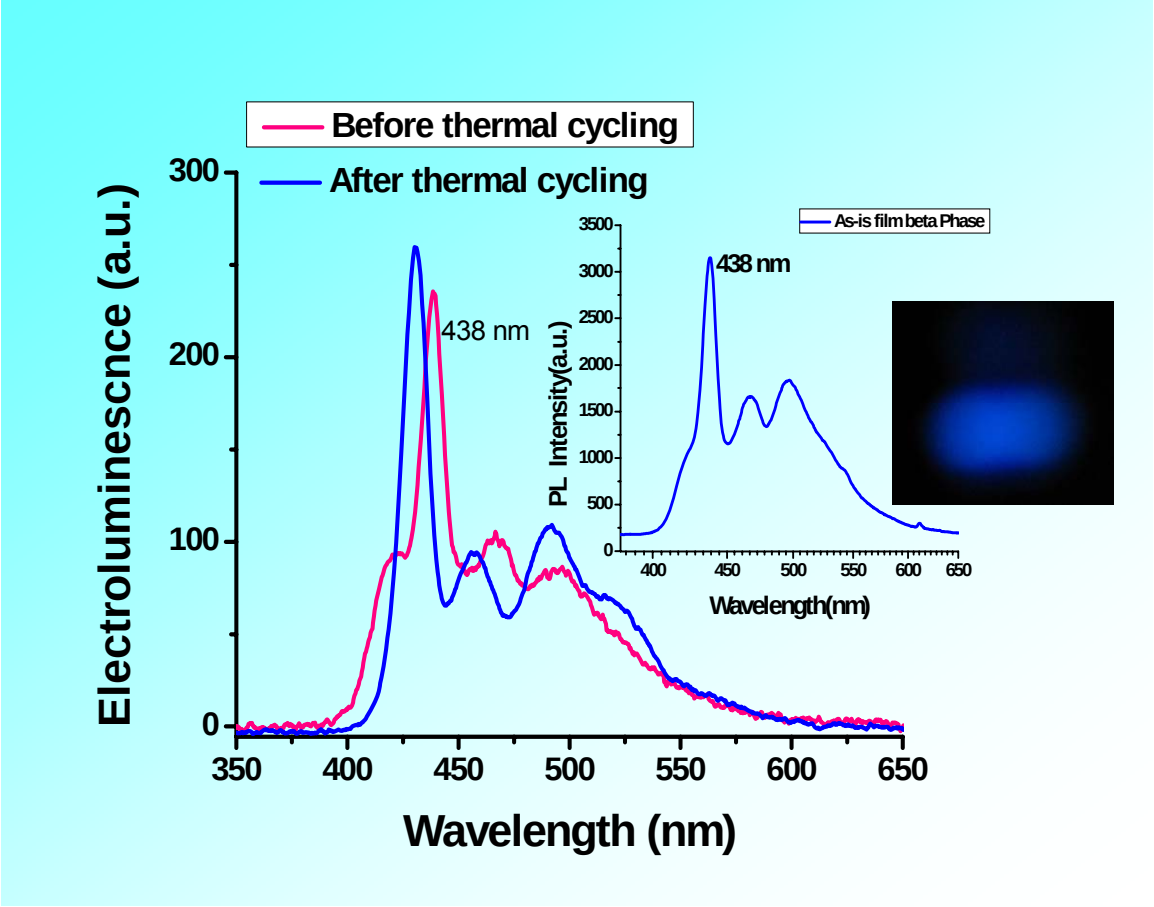

Figure (7.16): EL spectra from a PF8 LED. The red spectrum is from an as-is PF8 film and the blue spectrum is from a thermally cycled film. The inset shows the PL spectrum of the as-is PF film and blue light emission.

Fig. 7.16 shows the EL spectra from both as-is and annealed PF8. The as-is film has a higher fraction of the β conformer and thus results in a red-shifted spectrum. The 438 nm peak is the signature of this phase. The inset shows the PL spectrum of the as-is PF8 film from the same device region where EL was measured. As shown in the previous chapter thermal cycling of PF8 from various solvents results in a crystalline phase and this crystalline phase is incompatible with the β phase. EL spectrum of the heated film clearly shows the absence of the β phase, consistent with our PL spectrum of annealed PF8.

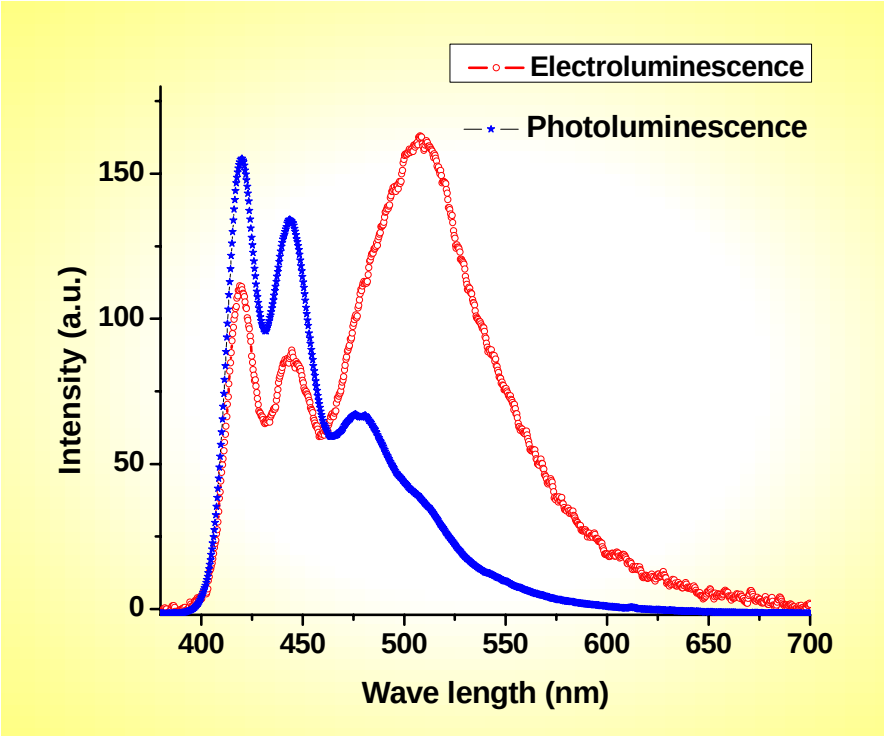

Figure (7.17): EL and PL spectra from a PF2/6 OLED.

Fig. 7.17 shows the EL and PL spectra from a PF2/6 LED. The PL spectrum was measured from the same device as the EL. It can be clearly seen that different energy

levels play a role in the PL and EL processes. Compared to the PL spectrum, the EL spectrum shows a huge greenish emission. This strong green emission at ~520 nm in the EL is most probably excimeric in nature. The Ca (capped Al) top electrode of the PF2/6 device may play a further role due to diffusion of Ca atom in the undesired greenish emission as the recombination most probably takes place closer to the metal electrode.

Fig. 7.18 shows the EL spectra from PF2/6 prepared inside and outside the glove box. The EL spectrum showed a substantial reduction of the green band emission from the device, which was prepared outside the glove box. The green band emission around 500 nm shows a complex features due to various possible excitations. These include excimers, aggregates and the keto defects.[3,4] For devices prepared outside incorporation of excess oxygen in the polymer film may help in the reduction of excimeric emission.

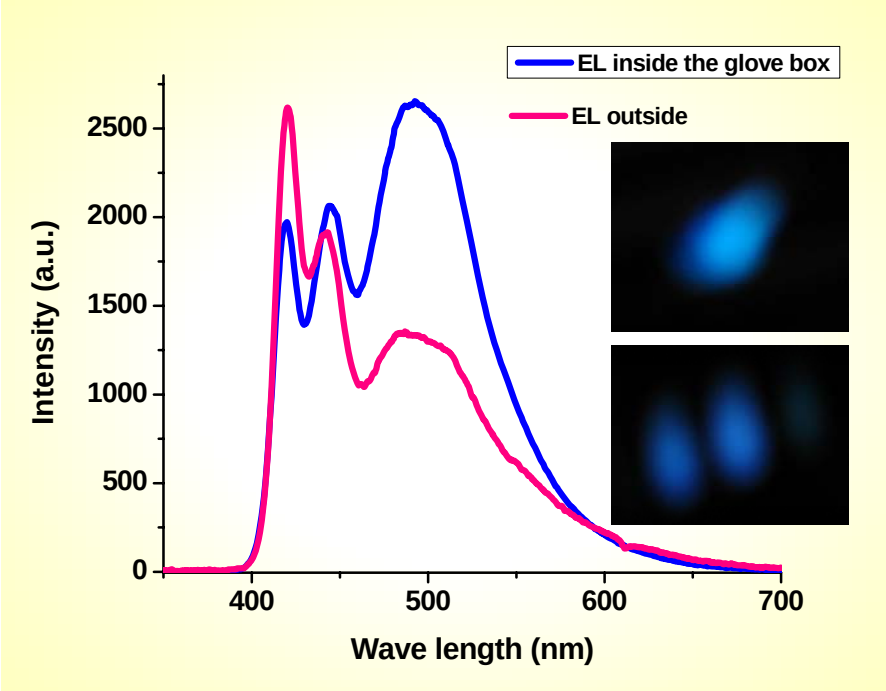

Figure (7.18): EL spectra of PF2/6-based OLED prepared inside and outside the glove box. Inset shows the corresponding emission.

Excimers form between two fluorenone units on adjacent chains or chain segments.[5] It is defined as a complex between an excited state of a molecule and a ground state of the same molecule which typically results in the emission of light at a lower frequency than that of the isolated molecule without affecting ground state spectral features. Keto defects emission is also clearly observed on the single-molecular level in coexistence with polymer-backbone emission. So it could be both keto and excimeric defect which is responsible for green emission[6,7]

Several approaches and methods have been demonstrated to help control the undesirable green emission, for modifying charge injection and mobility in the emissive layer and to improve thermal properties of the polymer. However, the nature of the green emission remains controversial and the mechanism that stabilizes the blue emission is not fully understood.

Absolute efficiency of PF2/6-based diode

The absolute efficiency of PF2/6-based LED was measured using the FOIS-1 fiber optic integrated sphere which accepts light energy from 200-1100 nm and gives absolute intensity values as a function of wavelengths, expressed in $\mu W/cm^2/nm$. Our absolute efficiency measurements of PF2/6 based diode shows intensity in the range of 0.2-0.3 $\mu W/cm^2/nm$ from a device area of (2mm x 2mm) compared to 3-4 μW for standard PF2/6-based device.

7.3 SCLC in polyfluorene based light-emitting-diode

It is believed that organic materials, in general, lack durability against high current density due to their low thermal stability. A major focus has been on the mechanism of injection of charge carriers in organic thin films under steady state condition without

damaging the structure. The efficiency and lifetime of OLEDs and devices based on LED structures are strongly affected by charge transport and injection.[8] Since conjugated polymers used in optoelectronic devices are quasi one dimensional and highly disordered with strong electron-phonon interaction, charge carriers in these materials are free polaron or trapped polarons and bipolarons.[9]

Appropriate metal contact with the polymer for efficient charge injection of both types of carriers and their subsequent transport into the polymer emitting layer play an important role in device performance. A clear understanding of charge injection, trapping and their transport are of paramount importance for OLED performance and their future application in flexible displays.

There are several experimental methods that have been suggested to study the transport properties and defect states in organic materials. Some of them include thermally stimulated currents,[10] photoinduced absorbtion,[11] impedence spectroscopy,[12] and $I-V$ in the space-charge-limited regime.[13] Among these methods SCLC based model is a simplified scheme to study the transport properties which yield information about energy and density of traps as well as charge carrier mobilities.

The variation of current with voltage applied gives information about the energy and density of trapping levels as well as their distribution with quasi Fermi energy level. The theory for nonlinear SCL conduction process in thin films was developed by Rose[14] and Lampart,[13] as described in Chapter 5. After the first studies of SCLC by Rose a comprehensive theory on the basis of regional approximation method was developed by Lampert et al.[15,13] to find out the role of traps, their concentration and distribution in energy on injected current flowing in the insulator in response to an applied voltage.

Many models have been worked out by assuming the following distribution of traps in energy: a set of traps characterized by a single energy,[16] two sets of traps distributed in energy,[17] exponential distribution,[18] double exponential distribution,[19] uniform distribution,[20] and Gaussian distribution.[21]

Shallow trapping with a single trap level in naphthalene and anthracene[22,18] crystal was clearly observed in $I-V$ characteristics, which is distinguished by four different regions discussed in details in Chapter 5. The one carrier SCLC with discrete set of shallow traps relies on the idea that the energy level of any given trap has a precisely defined value. For single-crystalline materials of high chemical and structural purity this is a good approximation for current injection. On the other hand, electron or hole traps in amorphous insulators and semiconductors do not have a uniquely defined environment because of the large structural disorder. As a result isolated discrete energy levels for traps in these materials do not provide an adequate model. In this section we have extensively studied charge carrier injection and transport using combined models of SCLC and TCLC for one carrier (hole only) PF based diodes.

7.3.1 Experimental details

The details of experimental device fabrication process have been discussed in the beginning of this chapter. Table 7.1-7.4 summarizes the details of our devices fabricated for this work. Thermal cycling (annealing) was done in a mini oven located inside the glove box. The dielectric constant of PF2/6 and PF8 layer was measured as 2.75 and 3.3 respectively, by capacitance-voltage method from a Al/(PF)/Al structure using an HP 4284A-LCR meter. The $I-V$ measurements were carried out in a manual probe station using a Keithly 236 source meter.

Table: (7.1) Fabrication details for PF2/6-based LEDs.

Sample (PF2/6)	Device Representation	Thickness (PEDOT)	Thickness PF2/6
A	ITO/PEDOT-PSS/[PF2/6(without anneal)]/PEDOT-PSS/Al	70-80 nm	90-100 nm
B	ITO/PEDOT-PSS/[PF2/6(annealed at 155^{o}C)]/PEDOT-PSS/Al		
C	ITO/PEDOT-PSS/(PF2/6)/Al		
D	ITO/PEDOT-PSS/(PF2/6)/Ca-Al		

Table (7.2): Fabrication details for PF8-based LEDs.

Sample (PF 8)	Device Representation	Thickness (PEDOT)	Thickness PF2/6
E	ITO/PEDOT-PSS/[PF8(without anneal)]/PEDOT-PSS/Al	70-80 nm	25-30 nm
F	ITO/PEDOT-PSS/[PF8(annealed at 155^{o}C)]/PEDOT-PSS/Al		

For thickness dependent SCLC measurements the PF2/6-based hole only devices were fabricated using the same fabrication procedure mentioned earlier. The device structure was (**ITO/PEDOT-PSS/[PF2/6(different thickness)]/PEDOT-PSS/Al)**. Five different samples were fabricated by varying the thickness of the PF2/6 layer as shown in table 7.3. The thickest sample (sample 1) (600nm) was grown from a solution of 60 mg of PF2/6 in 1 ml. of toluene solvent. The solution was then gradually diluted by adding toluene, four more samples were fabricated with different thicknesses. The samples 2, 3, 4 and 5 were 280, 200, 100 and 60 nm thick respectively. Thicknesses of all the samples were measured by Dektak surface profilometer. Two additional samples were fabricated with the structure: Al/(PF2/6)/Al, shown in the table 7.4.

Table (7.3): Samples used for thickness dependent measurements.

Sample	Device Representation	Thickness PF2/6 (nm)	Thickness (PEDOT) (nm)	Thickness (Al) (nm)
1	ITO/PEDOT-PSS/[PF2/6]/PEDOT-PSS/Al	600	70-80	100
2		280		
3		200		
4		100		
5		60		

Table (7.4): PF2/6-based MIM structure.

Sample	Device Representation	Thickness PF2/6 (nm)	Thickness (PEDOT) (nm)	Thickness (Al) (nm)
a	**Al/(PF2/6)/Al**	100	70-80	100
b		200		

Energy level diagram of the devices

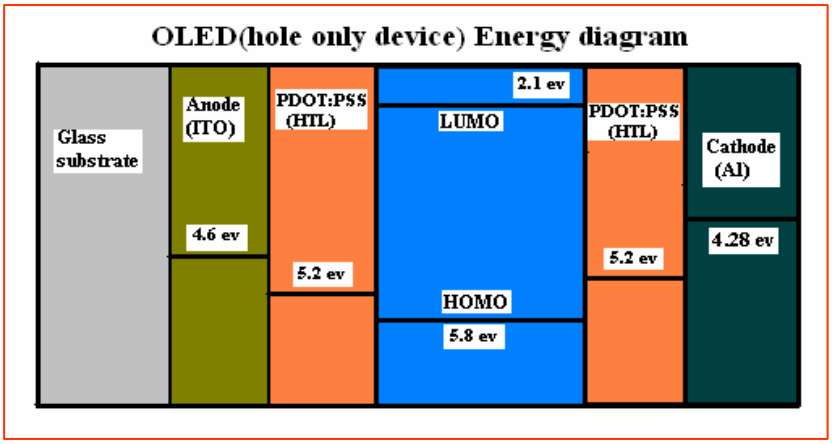

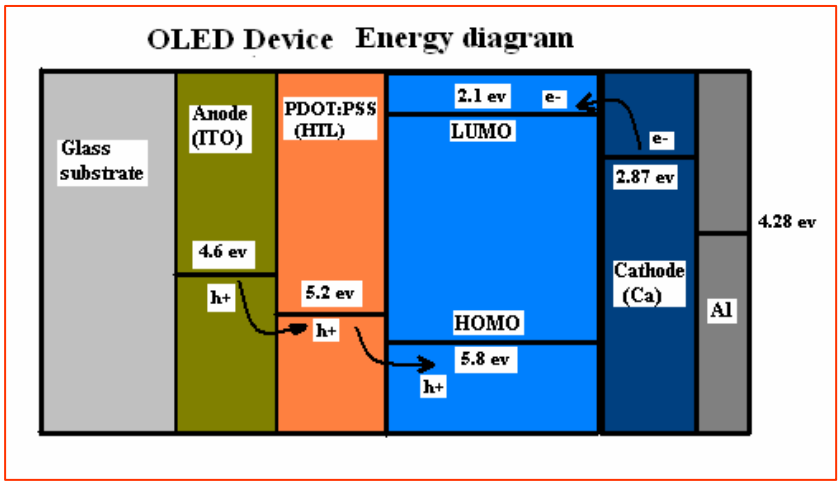

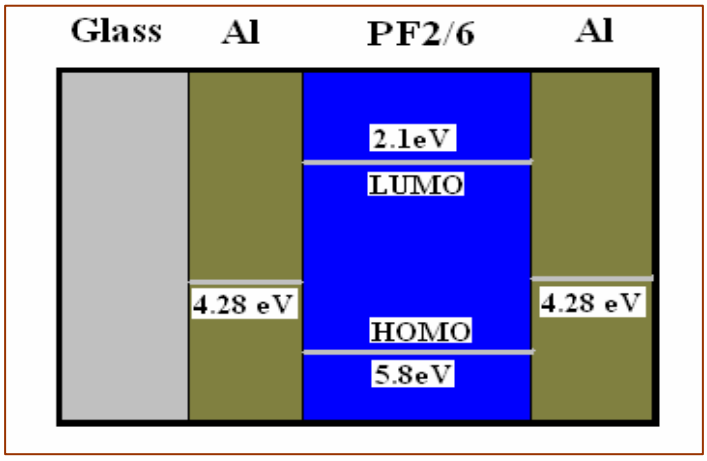

Figure (7.19): Energy level diagram of PF2/6-based hole only, OLED and MIM structure.

7.3.2 Experimental Results

(a) Current-Voltage relation for PF2/6 based diode

Fig.7.20 shows the current density (J) vs. voltage (V) of Sample A for many successive bias sweeps. The very first measurement clearly shows all four regions, characteristic of a one carrier discrete set of traps. The first region (a) is Ohmic, where the current density is proportional to the voltage, next region (b) is the SCLC trap-limited where the current density is directly proportional to the square of the voltage. The third

region (c) is the trap-filled limit where current increases nearly vertically and the onset of the trap-filled voltage V_{TFL} gives the density of traps N_t. The final region (d) is the trap-free SCLC which is similar to region two but the current is only limited by the space charge and free from the influence of traps. Since Sample A is a hole only device the trap-limited current arises from shallow hole traps. This is similar to what is seen in pure organic crystals like naphthalene and anthracene. [22, 18]

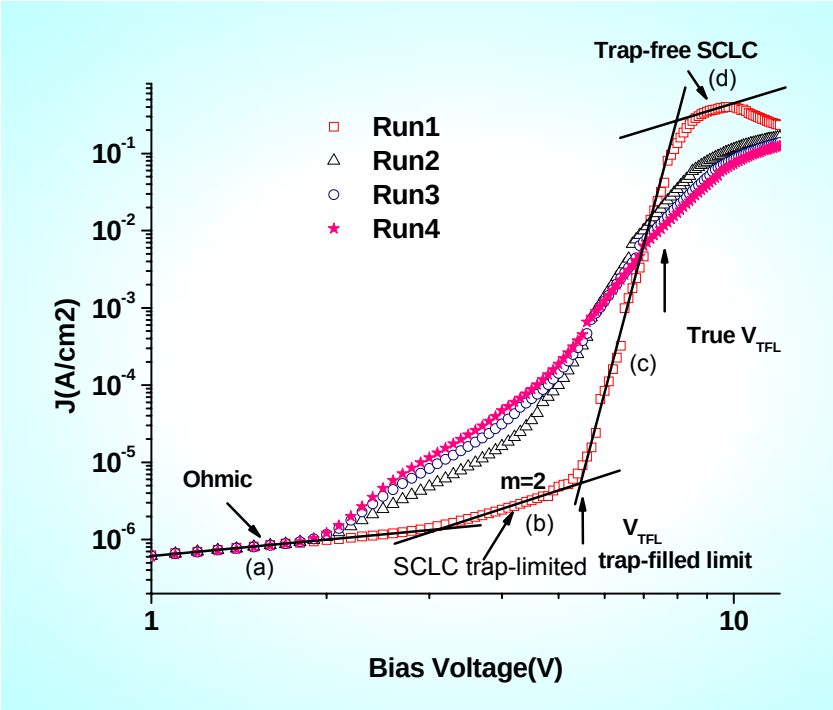

Figure (7.20): Experimental observation of discrete shallow trap from PF2/6-based diodes.

The $J-V$ characteristics of Samples C and D shows a similar behavior to Sample A. Although Ca provides a very low barrier for electrons, the device is predominantly hole-like. This is most probably due to the fact that the PLD grown ITO provides a better Ohmic contact with the polymer compared to Ca.

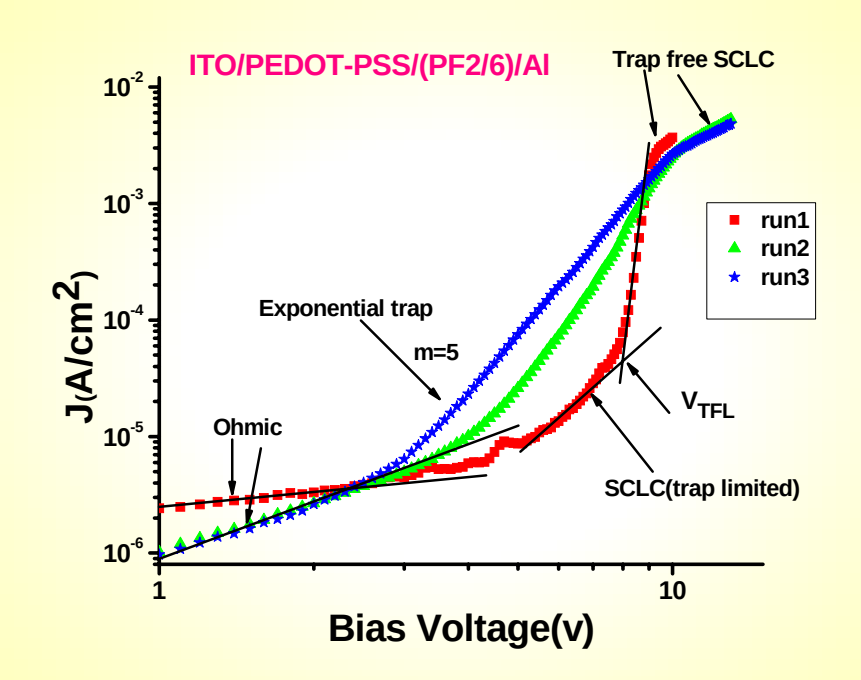

Figure (7.21): $J-V$ characteristics of sample C [ITO/PEDOT-PSS/ (PF2/6) /Al].

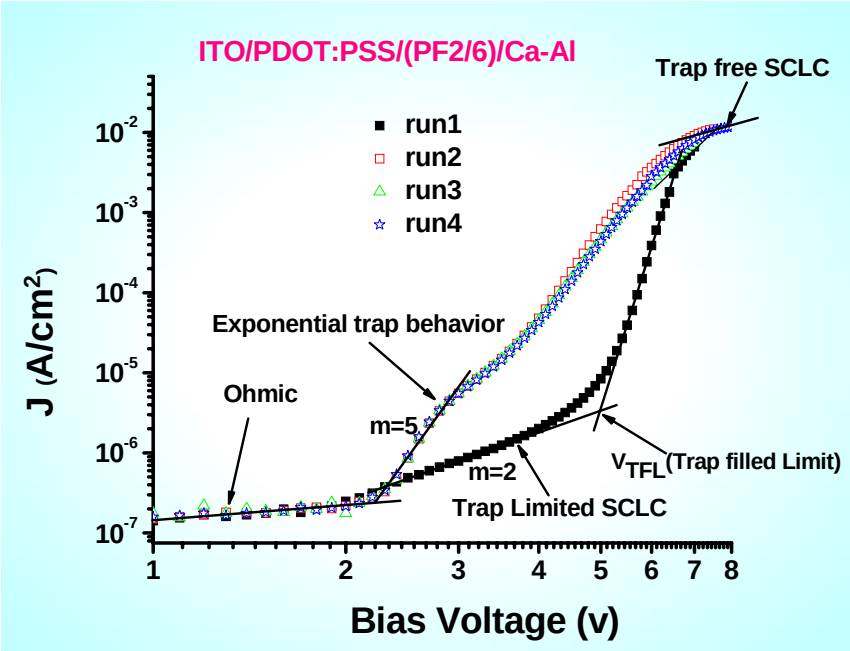

Figure (7.22): $J-V$ characteristics of sample D [ITO/PEDOT-PSS/(PF2/6)/Ca-Al].

Discrete-trap SCLC behavior is observed in the very first run of $I-V$ for all sets of PF2/6 based devices, after which subsequent bias sweeps show a distribution of trap energies as shown in Figs. 7.20-7.22. The density of traps N_t, their energy levels and the mobility of carriers are obtained from the $I-V$ characteristics.

One can extract all the relevant parameters from the four regions. By fitting region (d) with $J \propto V^2$, we extract the value of μ from Eq. 5.10 (Here we assume field-independent mobilities). This is then substituted in the trap-limited region (b) to obtain the value of θ using Eq. 5.11; we evaluate E_t from Eq. 5.12. We use N_v = 3x10^{21}cm^{-3}. The hole mobilities are in the range of 10^{-5} to 10^{-7} cm^2/Vs. The trap densities are of the order of 10^{17}cm^{-3} and the average trap energy of PF2/6 from the three devices is ~ 0.5 eV. This agrees with other works: TSC measurements yield a lower value for the effective trap depth (0.24 eV) in doped PF2/6, which is expected with increasing dopant concentrations.[23]

For all the PF2/6-based hole only devices the very first set of $J-V$ measurement shows a shallow discrete-trap SCLC behavior, after which the $J-V$ characteristics resemble that of an exponential set of traps distributed continuous in energy with $J \propto V^m$ The slope of the trap-limited region increases till m = 6, after which the $J-V$ characteristics does not change for subsequent measurements. These additional traps are created by the injected carriers at high fields. We verified this by sweeping the voltage of a new device (in Sample A) just below the trap-filled voltage and repeated the measurements several times; The $J-V$ characteristics does *not* change at all as shown by the open symbol in the Fig. 7.23 as long as the voltage is below V_{TFL}. Again, after

running the device once until trap-free SCLC, subsequent runs show the characteristics of a distribution of traps with m>2.

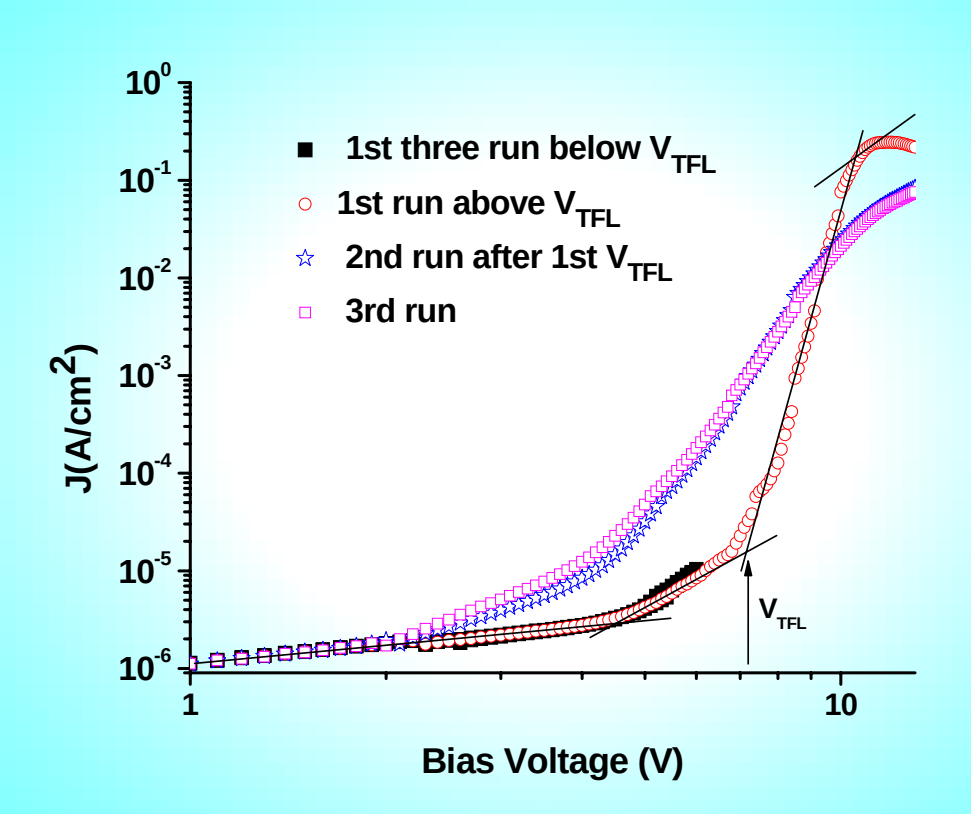

Figure (7.23): $J-V$ from a second device of sample A. The dark square symbols denote three successive $I-V$ sweeps below V_{TFL}; 'o' shows the very first run till trap-free SCLC voltages. Successive sweeps are shown by the three different open symbols.

The transition region from V_{TFL} to trap-free SCLC for the sample A is not perfectly vertical due to the generation of additional traps Moreover, the decrease in current at higher fields (trap-free SCLC region) suggests both emptying of traps[22] and additional creation of defects. In Table 7.4 the various parameters E_t, N_t, μ etc. are tabulated.

Table (7.5): Hole mobility, trap density, and energy of the traps obtained from shallow-trap *J- V* characteristics.

Sample	Mobility $cm^2/V.sec$ μ	Density of traps (N_t) $/cm^3$	Trap energy Et (eV)
A	1.8×10^{-5}	1.8×10^{17}	0.52±0.03
C	2.5×10^{-7}	2.1×10^{17}	0.35±0.03
D	1.9×10^{-6}	1.5×10^{17}	0.47±0.04

Detrapping effect by photoexcitation

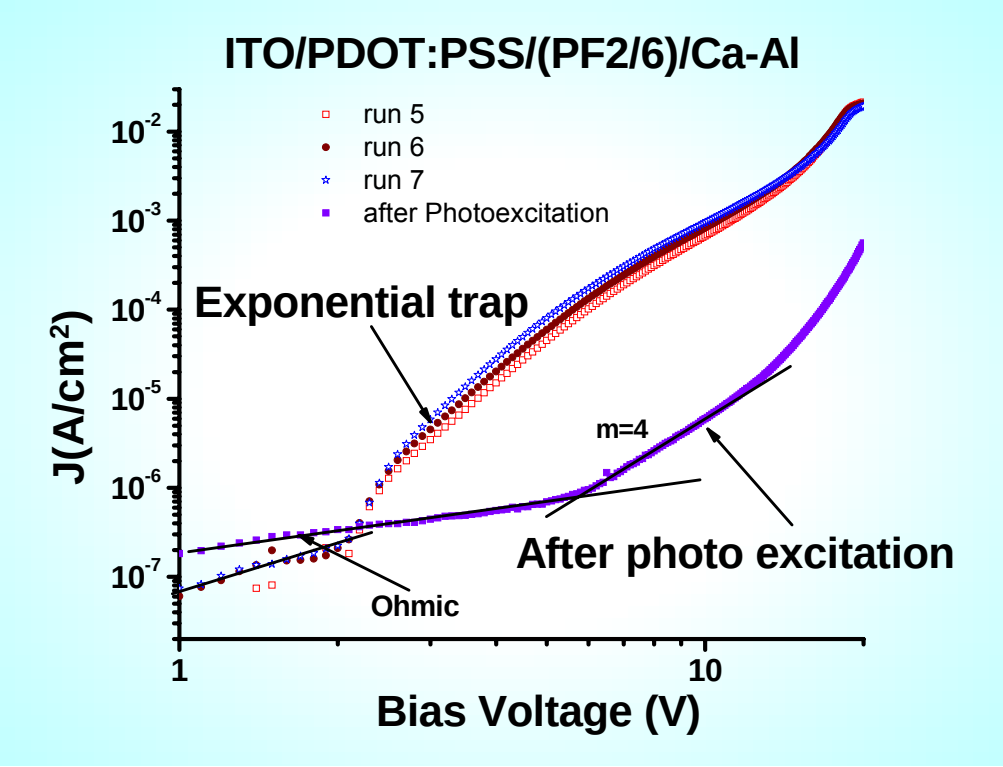

Figure (7.24): Successive $J-V$ curves after running the device many times. The bottom curve was taken after photoexcitation.

Fig. 7.24 shows the effect of detrapping by photoexcitation. The 457 nm line of an Ar+ laser was used as the excitation source. In the figure run 5, 6 and 7 indicate $J-V$ characteristics before photoexcitation. The sample was illuminated for ~15 min; remeasuring the current for a forward bias sweep shows the Ohmic and the SCLC region quite clearly as shown by the solid lines. Although the $J-V$ characteristics after photoexcitation reflect emptying of traps, it does not revert back to the initial shallow trap behavior. Since the trap states are more localized compared to the transport states, transitions from a localized trap state to the continuum are typically forbidden in organic semiconductors because of the selection rules.[24] The incident light generates excitons (both singlet and triplet), where the triplet excitons are also effective as detrapping agents.[22]

Typically free carriers are generated by autoionization, which then recombine with the trapped charges resulting in a detrapping process.[24] After photoexcitation, the Ohmic region extends for higher bias values, suggestive of the introduction of free charge carriers by the photoexcitation process. Without photoexcitation the lifetime of trapped charges is several hours.

To find out the density and distribution of trap energy states which are created at high fields with subsequent measurements, we have calculated DOS using the differential method[25] as described in Chapter 5. Figure 7.25 shows the calculated DOS [$g(E_{Fn})$] for three different situations: (a) the very first bias sweep, which resembles the first run shown in Fig.7.22, (b) after several bias sweeps when the traps are already filled, and (c) after photoexcitation when the traps are emptied. Initially the DOS is ~7 x 10^{17} $cm^{-3}eV^{-1}$ at ~ 0.5eV. Since the DOS calculation provides the distribution of traps with respect to

the quasi Fermi energy level, traps created at high fields with several bias sweeps show their distribution as ~2 x 10^{18} $cm^{-3}eV^{-1}$ at energy of 0.35-0.4 eV. After photoexcitation the DOS remains at ~2 x 10^{18} $cm^{-3}eV^{-1}$ with a shift of the quasi-Fermi level to ~0.5 eV, similar to the first run, suggesting partial emptying of traps. Since the DOS values remain higher compared to the very first run even after the traps are emptied, it is a clear indication that additional traps are created at higher voltages. Generation of trap states has also been observed in pentacene single crystals by bias- stress.[26]

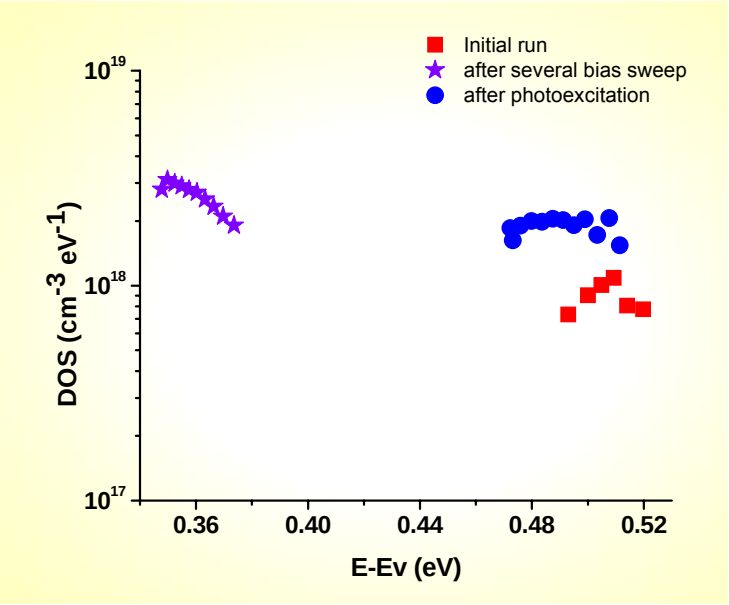

Figure (7.25): DOS distribution as a function of the quasi-Fermi level for the initial, trap-filled, and after photoexcitation bias sweeps in Sample D.

Temperature-dependent $J-V$ measurements yields alternate methods to estimate N_t and E_t by determining θ as a function of temperature. Unfortunately, since the shallow-trap behavior is seen only in the first bias sweep and driving the device above V_{TFL} results in exponential trap levels, discrete trap SCLC model cannot be used to extract θ as a

function of temperature. However, temperature-dependent $J-V$ measurements allow us to estimate the density of traps induced at higher voltages. The temperature-dependent $J-V$ characteristic was measured after running a device from sample A to higher voltages for a few times ensuring a steady state conditions.

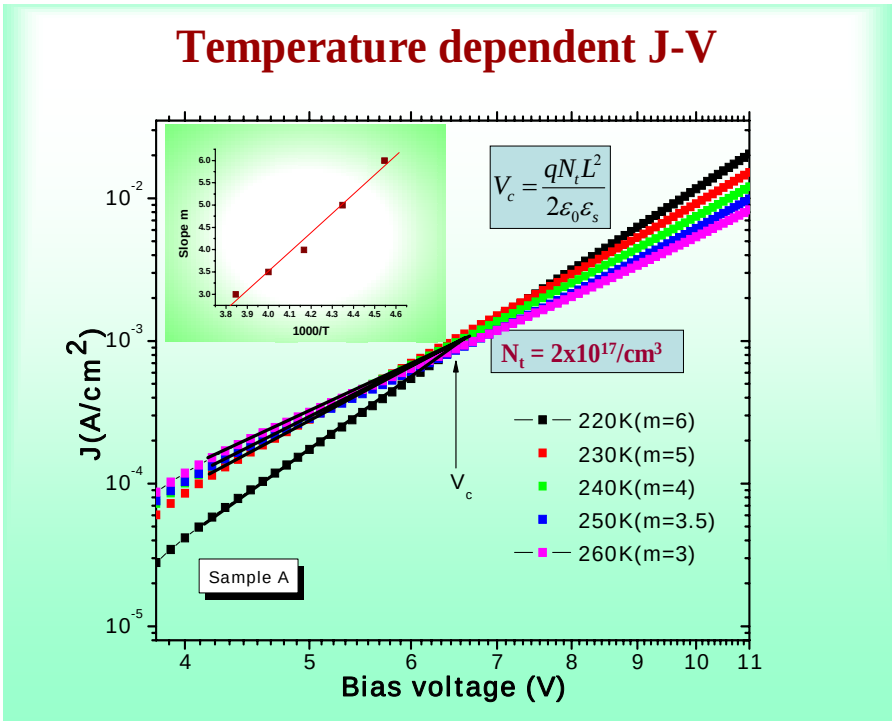

Figure (7.26): Temperature dependent $J-V$ for hole only device (Sample A). The inset shows change in slope with temperature.

In Fig. 7.26 only a section of $J-V$ characteristics measured at various temperatures is shown. SCLC theory predicts the intersection of the curves at different temperatures, which is clearly seen in Fig 7.26. At the cross-over voltage V_c the current is temperature independent, denoting that the activation energy is zero. This voltage is related to density of traps. Using V_c = 6.5 V, we obtain N_t as 2 x10^{17} cm^{-3}. The inset of Fig. 7.26 shows

that *m* (obtained by fitting only a narrow region of the *J-V* curve) increases as a function of inverse temperature, as predicted by the SCLC theory.

(b) Current-Voltage relation for annealed PF2/6 based diode

Fig. 7.27 is the $J-V$ characteristics of a PF2/6 based diode annealed at 155^{o}C, showing excellent agreement with one carrier SCLC for single discrete traps. The $J-V$ characteristic of the annealed PF2/6 sample was fitted with one carrier discrete set of shallow trap behavior. From trap-free SCLC, trap-filled limit and trap limited SCLC hole mobility, trap concentration and the energy of the trap level was calculated which are summarized in Table 7.6.

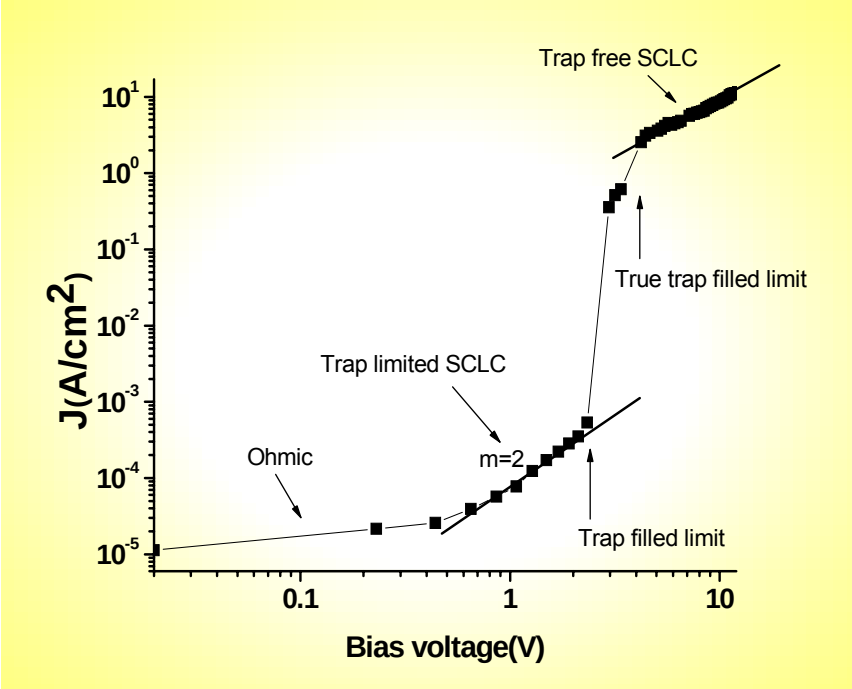

Figure (7.27): $J-V$ characteristics for annealed PF2/6 based diode shows single set of shallow trap behavior. Sample E.

Subsequent bias sweeps in the annealed sample B does not introduce additional traps, as shown in Fig. 7.28. Most likely this reflects that the additional trap states arise from structural disorder due to injected carriers at voltages higher than V_{TFL}. The annealed sample is in the hexagonal phase where the polymer chains adopt a specific orientation preventing such disorders.

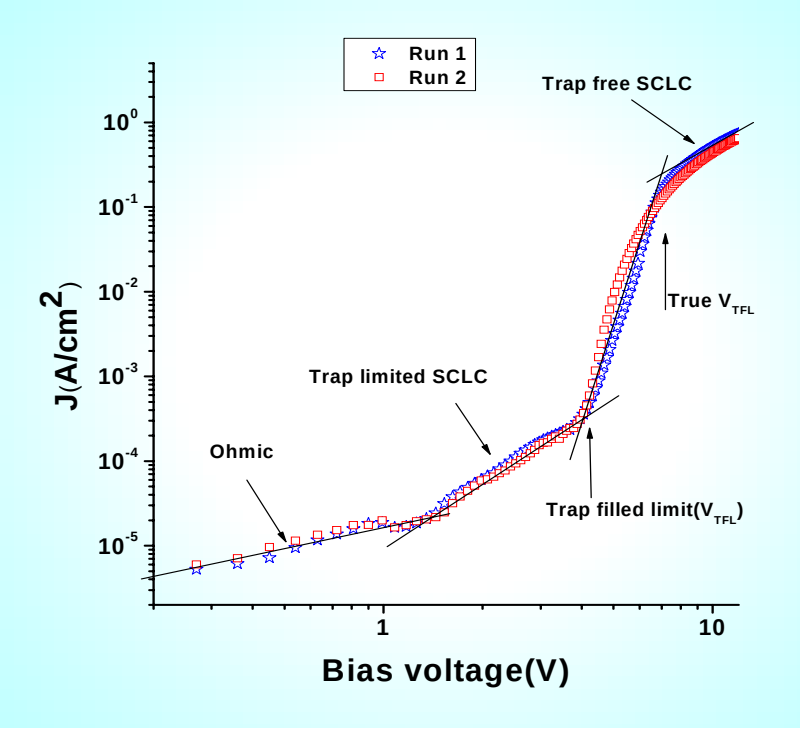

Figure (7.28): $J-V$ for thermally annealed PF2/6 with three subsequent run shows no additional creation of traps (Sample B).

(c) Current-voltage characterization of PF8 diodes

The $J-V$ characteristics of PF8-based hole only diodes show SCLC with a distribution of traps as discussed in Chapter 5. There are three regions here; the first region is the Ohmic where carrier trapping is low enough not to have a significant effect

on the current and thus the major contribution is due to thermally generated free carriers in the polymer.[27] The ohmic region is then followed by TCL current with the steeper slope (m>2) and finally the trap-free SCLC region. If more than one exponential distribution of traps is present in the material then the $J-V$ characteristics shows multiple TCL regions with slope m > 2.

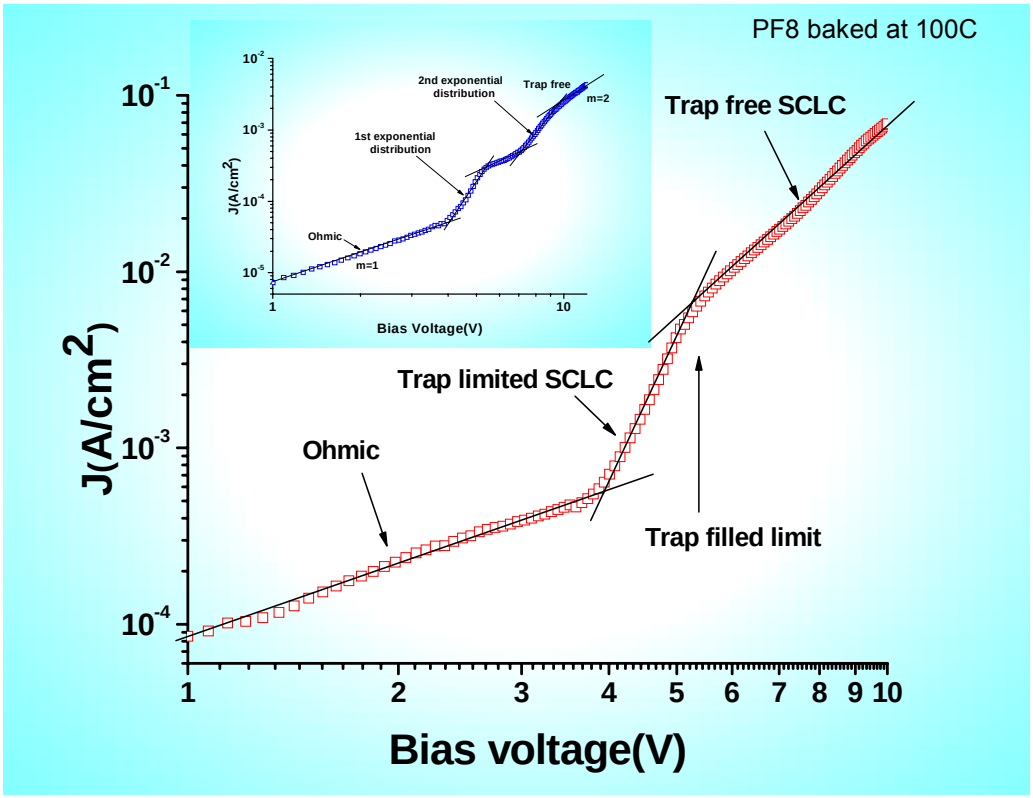

Figure (7.29): Current voltage characteristics of PF8 with exponential distribution of traps in (Sample E). The inset shows a multiple distributions of traps.

Fig. 7.29 shows the current voltage characteristics of PF8 from sample E with a distribution of traps where the trap charge limited current shows an average slope of m = 9, suggesting the presence of traps which are distributed exponentially within the forbidden energy gap. By fitting trap free region with $J \propto V^2$, we extract the value of μ

~1 x10^{-7} cm^2/Vsec and from the trap-filled limit the density of traps was calculated as 1.64 x10^{18} /cm^3. Fig. 7.29 inset shows $J-V$ behavior with the presence of multiple distribution of traps. Table 7.6 summarizes the transport parameters of PF2/6 and PF8-based hole only device.

Table 7.6: Comparison of mobility, trap energy level, and trap concentration of PF8 and PF2/6 based diodes.

PF Sample	**Treatment**	**Nt(/cm^3)**	**Mobility (cm^2/Vsec)**	**Avg. E_t(eV)**
PF 2/6	Without treatment	1.1 x10^{17}-1.8 x10^{17}	4.0 x10^{-5}-2.6 x10^{-7}	0.45±0.05
	Thermally cycled	0.7 x10^{17}-3.1 x10^{17}	2.3 x10^{-4}-2.1 x10^{-5}	0.40±0.03
PF 8	With and without treatment	1.6x10^{18}-3x10^{19}	2.1x10^{-6}-1.1x10^{-7}	0.2-0.35

7.4 Thickness dependent SCLC

The electronic properties of organic semiconductors are profoundly different from covalently or ionically-bonded inorganic semiconductors.[28,22] Due to the weak van-der-Waals bonding, the surface of organic semiconductors is characterized by an intrinsically low density of dangling bonds. Owing to the weak bonding the surface of organic semiconductors can be heavily damaged by the contact fabrication processes, which may result in traps at the surfaces.[29]

From our results in the previous section we have shown that PF2/6 based diodes can be modeled with discrete set of shallow traps and this behavior is seen only in the very

first bias sweep; subsequent measurements shows exponential set of traps distributed continuous in energy. A question which arises here is what is the origin of these traps? Are these at the surface of the polymer-metal contact or deep inside the bulk of the material? To answer these questions one needs to look at the thickness dependent charge transport behavior.

In this section, we have investigated the effect of surface and bulk traps on the PF2/6 based diodes using thickness dependent SCLC measurements. We show that a detailed knowledge of traps is a key factor to understand charge transport in blue-emitting polymers.

7.4.1 Experimental Results

$I-V$ measurements were done for five different thicknesses of sample 1 to sample 5. Fig. 7.30 shows the thickness dependent SCLC of PF2/6-based as-is hole-only device. The top contact (Al) was negatively biased and the bottom ITO contact, which is the hole injector was positively biased. The $J-V$ characteristics of all the samples show distinct four regions (1) Ohmic (2) trap-limited SCLC (3) trap-filled limit and finally (4) trap-free SCLC. The density of traps was calculated from true V_{TFL}. Fig. 7.31 shows an exponential dependence of the trap concentration with increasing thickness, consistent with the SCLC model.

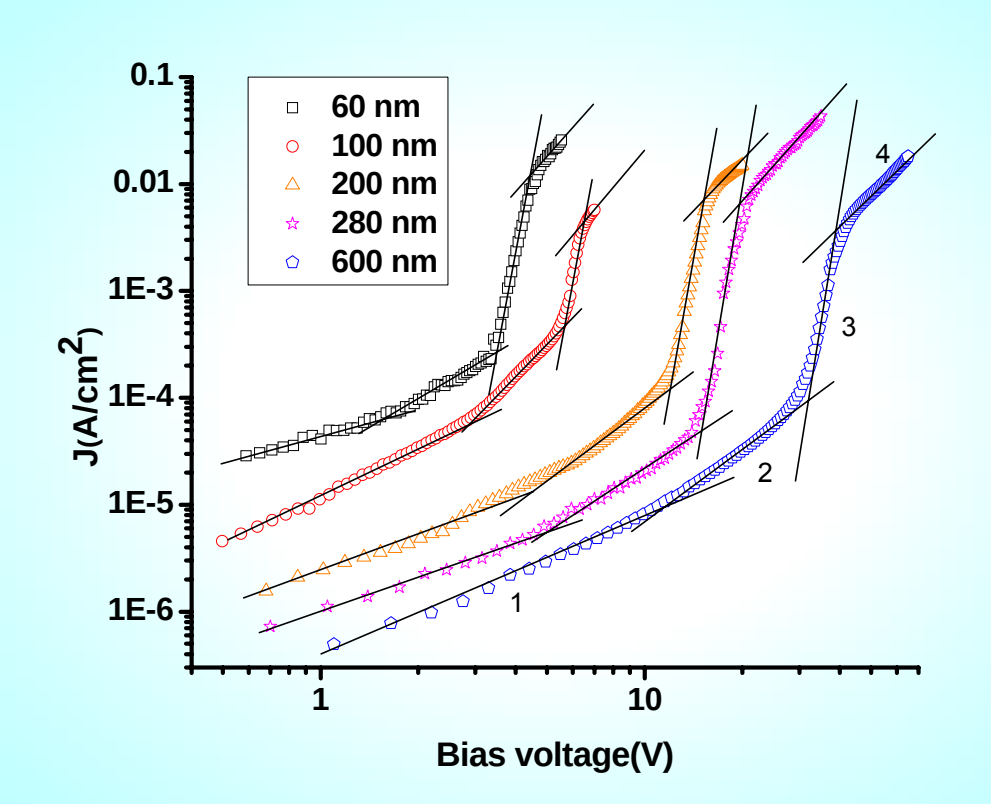

Figure (7.30): SCLC for hole only device (sample 1 to sample 5) with different thickness.

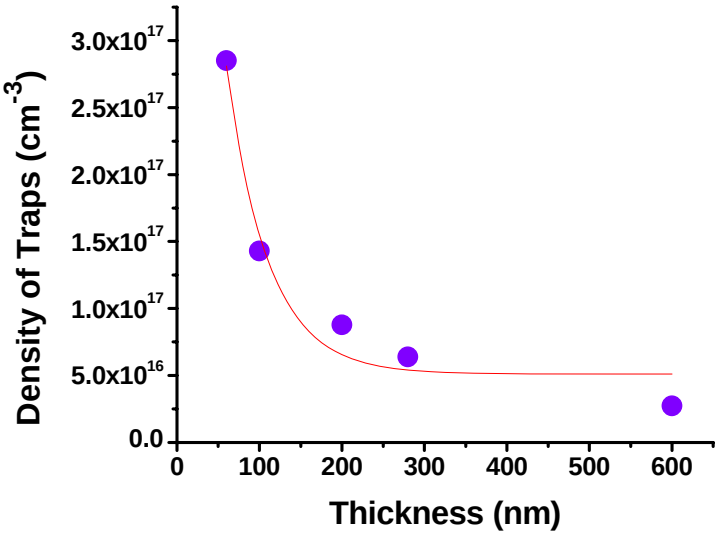

Figure (7.31): Density of traps (N_t) calculated from V_{TFL} with different thickness of the film.

The value of the true V_{TFL} was obtained from the intersection of the vertical line joining trap free SCLC and is found to scale linearly with the thickness as shown in Fig. 7.32.

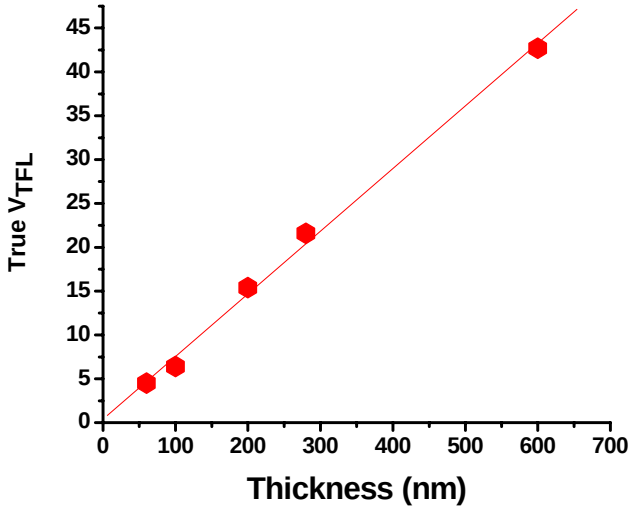

Figure (7.32): V_{TFL} scales linearly with thickness.

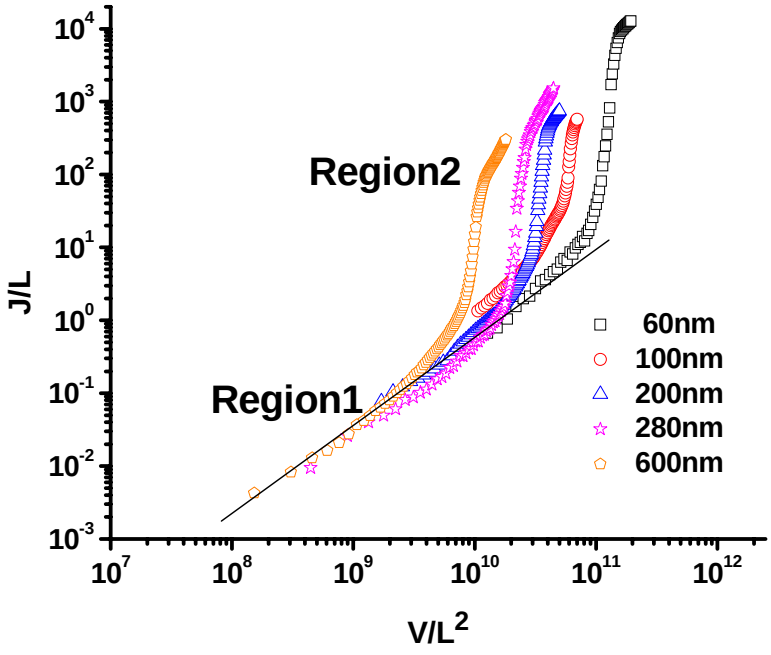

Figure (7.33): A scaling law plot (J/L) vs (V/L^2) with different film thickness L.

For SCLC conduction in a homogeneous material, a scaling law $J/L = f(V/L^2)$; is obeyed.[13] This form of the thickness dependence is valid only if the Fermi-level position and the DOS distribution are the same in all films, independent of their thickness. Our J/L data (Fig. 7.33) shows two different sections. It is noted that the overlapping of the data in the Ohmic region is much better compared to the SCLC region, which shows a systematic variation with the thickness. Similar thickness dependent scaling law for inorganic materials is seen for diamond film[30] and for sputter deposited SiH film.[31,32]

Fig. 7.34 shows the $J-V$ characteristics of sample 5 and sample 2 for two different thicknesses is sweeped from reverse to forward bias. Current in the reverse bias condition indicates that ITO makes an Ohmic contact with the polymer layer. Typically for devices with a Schottky contact, the current in the reverse bias is much smaller than the forward bias current.[33]

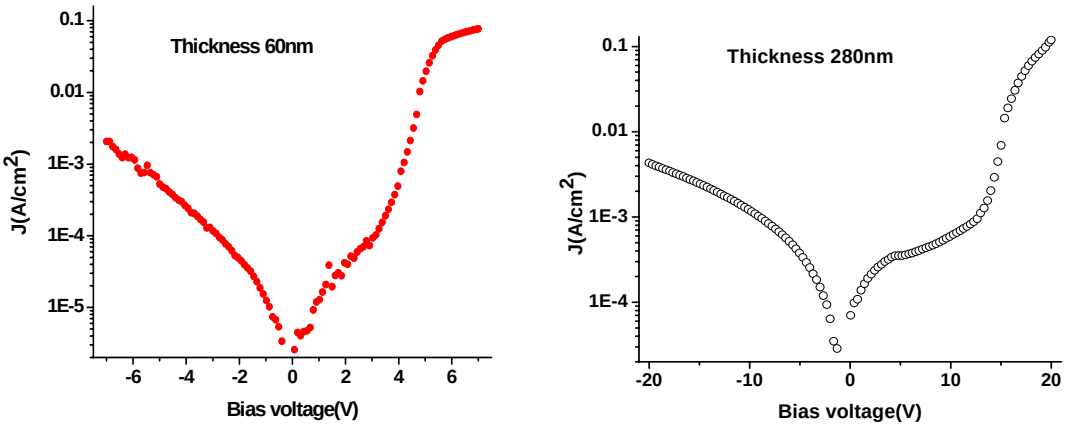

Figure (7.34): J-V of thermally cycled PF2/6 based diode of Sample with 60nm (sweeping voltage -7V to +7V) and 280 nm (sweeping voltage -20V to +20V).

Fig. 7.35 shows the DOS values at the Fermi level ($E_V - E_F$) from 0.35-0.45 eV for various thicknesses. The DOS varies from $2\text{x}10^{17}$ to $4\text{x}10^{18}$ $cm^{-3}eV^{-1}$ and then saturates

for higher thicknesses. This implies that defects created for thin interface layers (L≤200nm) most probably arises from the surface of the organic-metal layer and dominates the DOS of the whole film. For thicker sample it is predominantly the bulk traps that dominate. The influence of the interfacial layer with an increased DOS will of course be reduced if sufficiently thick samples are used, as observed from our DOS calculation. The DOS was normalized with respect to sample 1 (600nm). Our normalized DOS shows that for an interface layer of 60 nm, the DOS value is ~ 20 times larger than that in thicker films.

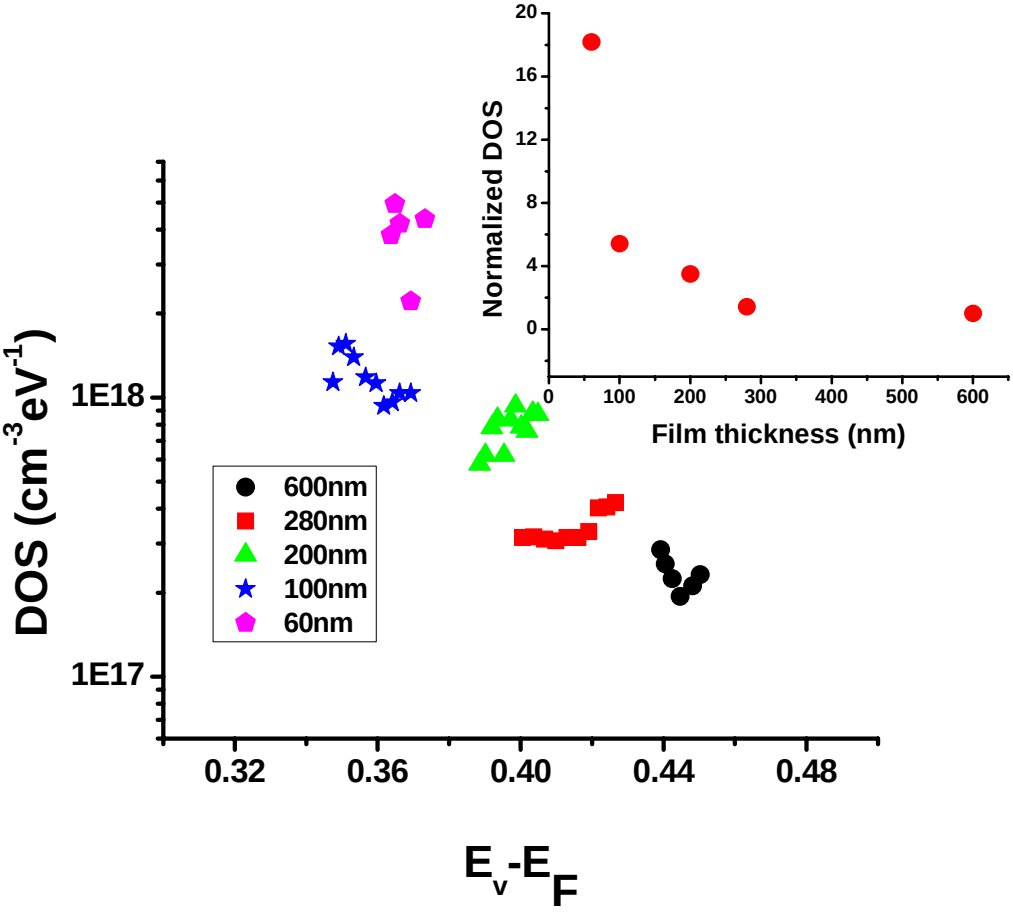

Figure (7.35): DOS calculation from the trap limited SCLC for different thickness of the film and the inset shows normalized DOS with thickness.

Discrete trap SCLC from PF2/6 was verified from another device Al/(PF2/6)/Al for two different thicknesses. Fig. 7.36 shows the $J-V$ characteristics from these two samples. Replacing the anode (ITO and PEDOT) with an Al electrode also shows single carrier shallow trap SCLC behavior. This clearly indicates that shallow trapping with discrete trap energy originates from the PF2/6 layer and not from the PEDOT-PSS layer.

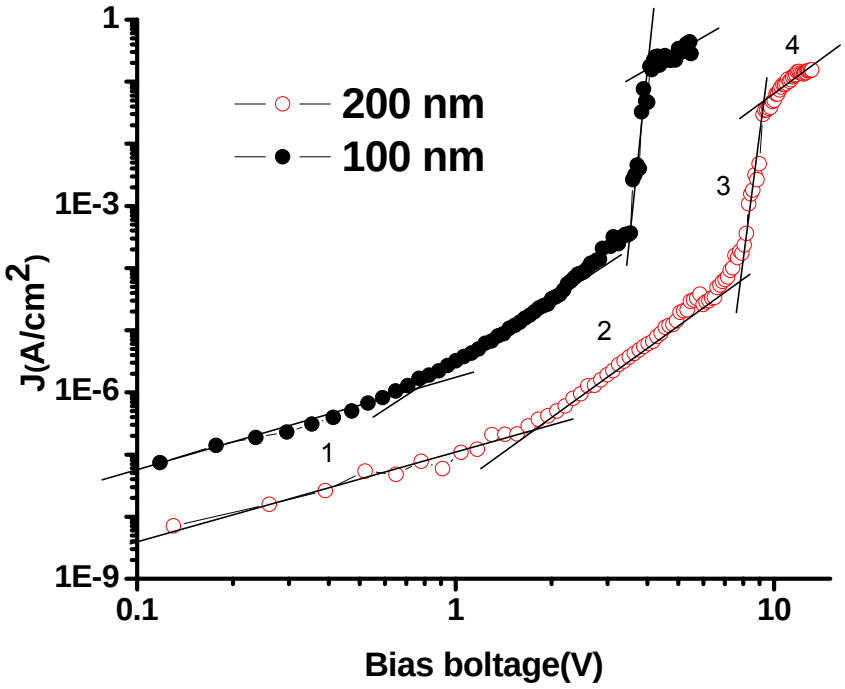

Figure (7.36): SCLC of Al/(PF2/6)/Al structure with two different thicknesses.

Temperature dependent conductivity measurements

The temperature dependent dc conductivity was measured for two different thicknesses. Fig. 7.37 shows the temperature dependent $I-V$ for the 600 nm thick sample from 290K to 420K. The inset figure shows the conductivity measurements as a function of temperatures. At low temperatures very weak temperature dependence is

observed. In the high temperature range, the temperature dependent conductivity fits with a variable range of hopping mechanism described by the following equation:

$$\sigma(conductivity) = \sigma_o \exp\left[-\frac{B}{T^{1/4}}\right]; \quad B = \frac{4E}{k_B T^{3/4}}, \tag{7.1}$$

where σ is the conductivity, σ_o is the exponential term, and E is the activation energy for hopping conduction. The calculated activation energy is in the range of 70-100 meV.

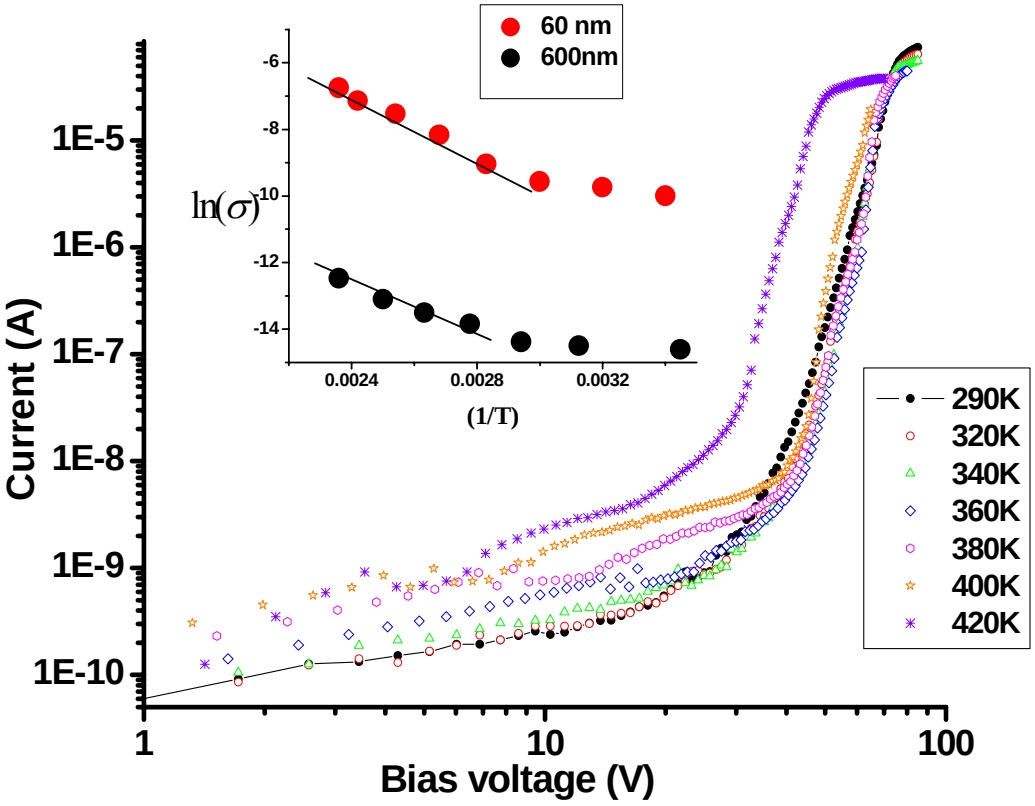

Figure (7.37): $I-V$ characteristics with different temperature and the inset show the conductivity with respect to temperature.

7.5 Discussion of Results

The single trap level SCLC model for charge injection believed to be applicable only for crystalline materials of high chemical and structural purity is an excellent model for PF2/6. The charge injection in this blue-emitting polymer with a high level of molecular disorder is for the first time successfully modeled by discrete energy levels for traps. These unexpected findings suggest that charge injection and transport occur through regions of ordered chain segments in the polymer. The topography and phase images of PF2/6 film from AFM measurements from the annealed sample indicates the presence of ordered segments, shown in Fig. 7.38.

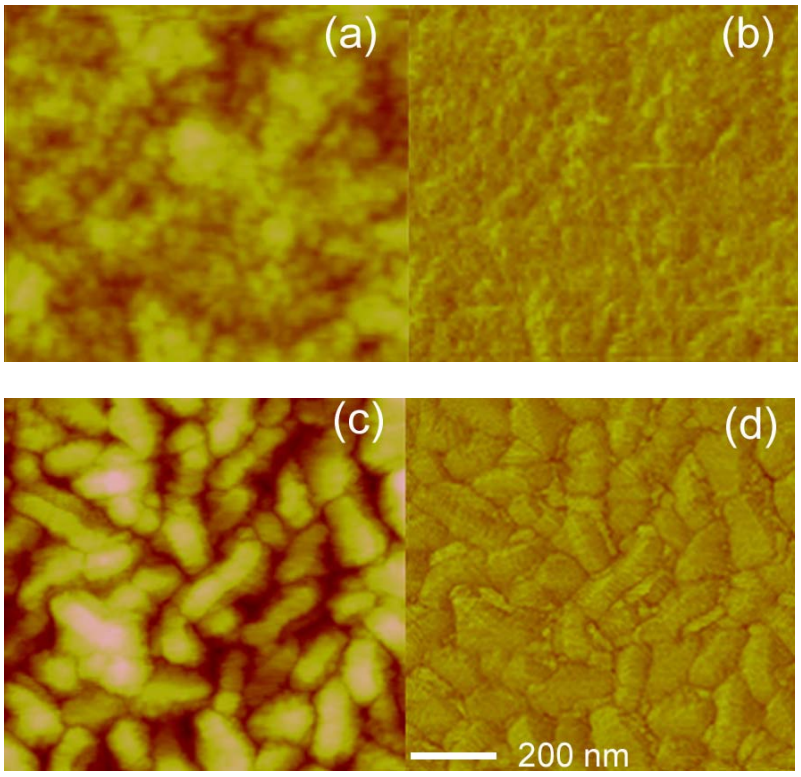

Figure (7.38): AFM image of PF2/6 polymer film (a), (b) represents the topography and phase images of as-is sample and (c), (d) for annealed sample.[34][Courtesy:Mengjun Bai]

Our atomic force microscopy studies from annealed PF2/6 films show average footprint area of ~ 10^4 nm^2. Although PF2/6 has a high degree of interchain disorder, the as-is polymer shows regions of structural ordering that resembles the hexagonal phase.[54] We speculate that these ordered segments are most probably responsible for charge transport by a percolative method as schematically shown in Fig. 7.39.

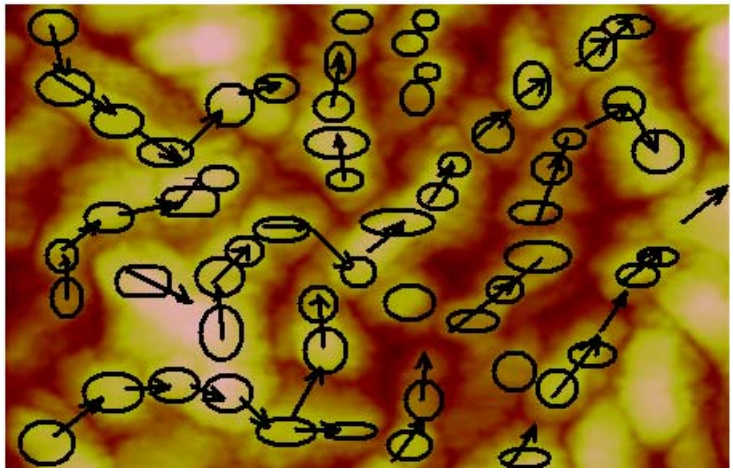

Figure (7.39): Schematic of the transport mechanisnm through the ordered segments.

The origin of the initial set of traps in PF2/6 based hole only device could be structural or chemical defects, which typically give discrete trap states. Although we do not thermally treat the PF2/6 film, it shows a signature of the hexagonal phase at room temperature.[35] The defects may occur at the grain boundaries in the polycrystalline layers or at the interface, resulting in shallow trap SCLC. The exponential set of traps that are created may also arise from hydrogen and oxygen-induced defects [36] PF2/6 is known for its fluorenone defects at the bridging carbon atom,[37] application of high voltages may create more of these defects.

For PF2/6 based diode since the injected carriers beyond the trap-filling voltage create a continuum of trap states, subsequent sweeping of the bias yields a higher current, representing a distribution of traps. The density of trap states calculated from experimental results clearly shows that additional trap states are created at higher voltages. The life-time of the trapped charges is many hours, which can be detrapped by photoexcitation.

Thermal annealing of PF2/6 forms an ordered hexagonal phase; devices fabricated from this phase also show discrete traps under SCLC with no additional generation of trap states at higher voltages and improves the mobility of the carriers by more than one order of magnitude compared to the un-annealed sample.

Although there are different transient techniques like time-of-flight (TOF) or transient electroluminescent for studying charge transport in conjugated organic materials but most of the CPs contain trap states with characteristic trapping times long enough not to affect transient mobility measurements; the trapping times are usually small to impact steady-state currents.[38] OLEDs are normally operated in steady state or quasi steady-state regime; hence the results of transient mobility measurements do not have a direct relevance to the real device performance. Additionally in the TOF technique mobilities are measured from films much thicker (1 μm) than those normally used in OLEDs (100 nm). Since the film preparation method for thick films is very different from that of thin films, the resulting morphology can give rise to different charge transport characteristics compared to thin films. Our calculated mobilities of PF2/6 from one carrier SCLC closely resemble that of values available in the literature done by Pool-Frenkel model of hole mobilities for green emitting PF copolymers.[38]

SCLC measurements of PF8, on the other hand, are much more sensitive to the processing conditions. In the alpha crystalline phase, PF8 shows a presence of discrete single and multiple set of traps of exponential distribution with energy 0.2-0.3 eV and trap density ~ 10^{18} /cm^3. The hole mobility is obtained as in the range of 10^{-6}-10^{-9} cm^2/Vs. which is similar to the values obtain by K. Mura et.al. for F8BT (PF8 based copolymers).[39] These values of hole mobilities are two-three orders of magnitude lower than PF2/6 and other green emitting PF copolymers. This may arise due to the complex structural phase present in PF8 polymer which impacts the injection of carriers. Therefore the hole current in PF8 most probably arises due to injection limited rather than space charge limited.

The thickness dependent SCLC measurements reveal the presence of both surface and bulk traps. The bulk density of deep traps is usually assumed to be uniform throughout the material. In real materials, however, many more traps per unit volume are likely to be present close to the sample surface than in the bulk which depends on the interface formation and thickness of the polymer film. These surface traps can have different physical origins.[29]

In OLED fabrication, generally the top and bottom contacts are prepared in a different way and in that case surface traps present in contact may differ considerable from the other contact and even for contacts prepared in identical way the density of traps at the surface may differ considerably depending on parameters which are not under experimental control.[40,41] Our observation of $J-V$ characteristics for thickness dependent SCLC from PF2/6 based hole-only devices show that the defect states are not only located on the surface but also extends into the bulk with a likely scenario that the

traps exponentially decrease from the surface. For thicknesses below 200 nm surface traps are dominant over bulk traps. As mentioned earlier discrete set of shallow traps is seen only in the very first bias sweep and subsequent runs induce a distribution of traps. The origin of these additional distribution of traps most probably arise at the interface because for thinner film, higher currents will more likely damage the interface bonding during contact formation than in thicker film.

Thickness dependent SCLC measurements also show that for thinner films both single and multiple set of discrete set of traps are likely to be present; subsequent measurements induce additional set of traps which may be avoided by either thermal cycling the film or making a device using a thicker film. Fig.7.40 shows the $J-V$ characteristics for three different thickness of as-is PF2/6 with subsequent bias sweeps. These measurements along with our DOS calculations show that with increasing thickness the SCLC is dominated by the presence of bulk traps.

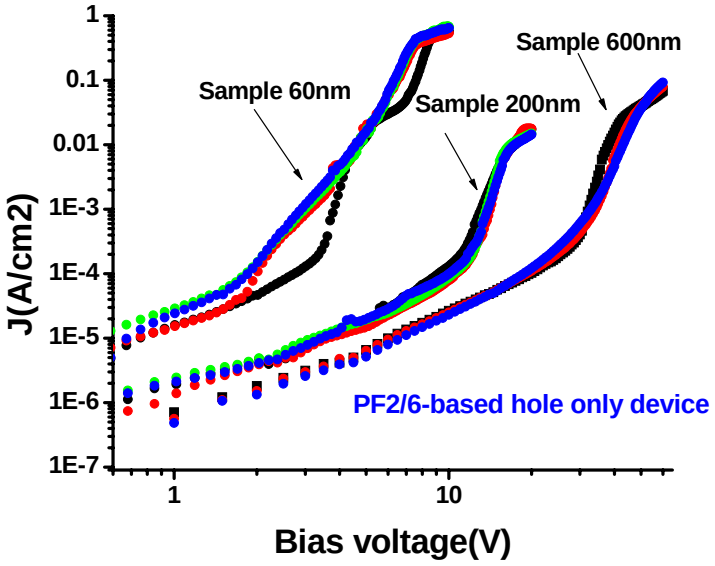

Figure (7.40): $J-V$ characteristics of three different thickness of the film with subsequent run.

In conclusion our SCLC studies of PF2/6 and PF8 shed new light on the mechanism of charge injection and transport in polymers where the transport mainly occurs through regions of ordering. The SCLC model with discrete shallow and distribution of trap levels may be applied to other amorphous polymers with regions of ordering to study charge transport. The thickness dependent SCLC measurements show the influence of both surface and bulk traps on charge transport. For device fabricated from very thin film (≤100nm), the total amount of surface traps dominate over the total amount of bulk traps and which subsequently changes the behavior of the $J-V$ characteristics. The temperature dependence of $I-V$ and dc conductivity suggests thermally assisted variable-range hopping transport mechanism instead of band transport in these materials.

7.6 Raman scattering from polyfluorene – based LEDs

7.6.1 Introduction

The physical and chemical properties of conjugated organic polymers with π-electrons have been interpreted in terms of self-localized excitations, which are quasi particles with structural changes over several repeating units. These excitations may be classified into solitons, polarons, bipolarons, and excitons, according to their charge and spin.[42] A deep understanding of creation, transport, and decay processes of these excitations is important for conjugated polymer (CP) devices. Self localized excitations are generated through photo-irradiation above the band gap of a CP. On the micro to millisecond time scale, photo generated excitations are expected to be polarons, bipolarons, and triplet excitons.[43] Fig. 7.41 shows the schematic of the energy-level of self-localized excitations.

Unlike traditional semiconductors, charge carrier injection in CPs can also induce structural deformation that results in self-localized excitation states within the band gap. In CPs with a nondegenerate ground state both doubly charged (spinless) bipolarons and singly charged polarons coexist.[44] Doping or injected charges result either in the formation of polarons or bipolarons. In the alkyl thiophene systems it is seen that chemical doping results in localized polarons, whereas photoexcitations give rise to delocalized polarons.[45] Recently infrared (IR) spectroscopy in poly(3-hexythiophene) (P3HT)-based field-effect transistors (FETs) has been effectively used to study charge injection; increased gate voltage results in an enhanced absorption which can be directly correlated to polarons and bipolarons.[46]

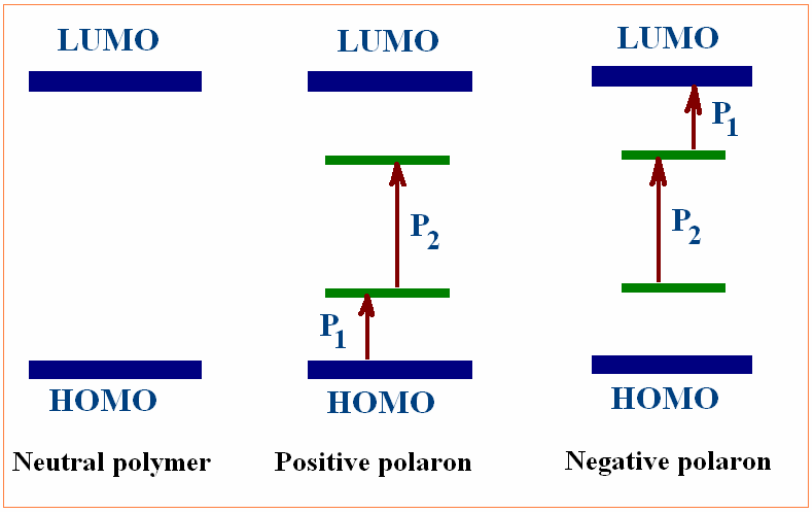

Figure (7.41): The energy-levels of self localized excitations: neutral polymer, positive polaron and negative polaron.[47]

Raman scattering has played a significant role in deciphering backbone and side chain morphologies in PFs. A combined theoretical and experimental Raman scattering study in PF8 has resolved the issue of the beta phase by focusing on the vibrations of the

alkyl side chain which was discussed in detail in Chapter 6.[48] Enhanced interchain interaction (by the application of hydrostatic pressure) in PF2/6 shows an antiresonance effect in the Raman spectra indicative of a strong electron-phonon interaction between the Raman phonons and the electronic continuum that arises from defect states.[49]

Quantum mechanical interference between a discreet state and a quasicontinuum manifests itself as asymmetries in the scattering cross sections near a resonance with a characteristic line shape. Such effects have been observed in inorganic semiconductors, for example in *p*- and *n*-doped Si,[50,51] and more recently in organic semiconductors.[46,51 ,52] In this section we present our Raman scattering results from PF2/6-based LED structures in the presence of photogenerated charge carriers by applying an external bias.

7.6.2 Experimental details

Single layer PF2/6-based LED structures were fabricated by spincoating PF2/6 from a toluene solution (10mg/ml) on a patterned indium tin oxide (ITO) layer; the fabrication steps are similar as described in details at the beginning of this chapter. The thickness of the PF2/6 layer was ~100 nm and the device area was 2-4 x10^{-4} cm^2. The 785 nm line of a diode laser (~5 mW) was used as the excitation source and the devices were probed from the ITO side as shown in the inset of Fig.7.42. *p*-doping was achieved by adding F4-TCNQ (purchased from TCI) and 10 mg of PF2/6 in 1 ml of *p*-xylene (Sigma-Aldrich). The weighed polymer and dopant were dissolved in *p*-xylene at ~ 65^{o}C using a similar procedure outlined by Hwang and Khan.[53] Five different doping concentrations from 1 wt % to ~ 35 wt % were used. *p*-doped LED structure was fabricated using 25 wt % film.

7.6.3 Experimental Results

Fig. 7.42 shows the Raman spectrum of PF2/6 layer from an LED structure in the 1000-1700 cm^{-1} region. The bottom most spectrum is the first measurement from the film without the application of any external bias. The origin of the Raman peaks was discussed in chapter 6. Here we briefly mention them again. The 1100 cm^{-1} region arises from the in plane C-H bends and ring distortion type motion. The 1200-1300 cm^{-1} region originate from the backbone C-C stretch type motion.[54] The C-C stretch modes between adjacent monomers split into two peaks at ~1280 and 1304 cm^{-1}.[48] The 1342 cm^{-1} Raman peak corresponds to the C-C stretch frequency within the monomer unit. The strong 1605 cm^{-1} peak corresponds to the C-C intraring stretch mode.

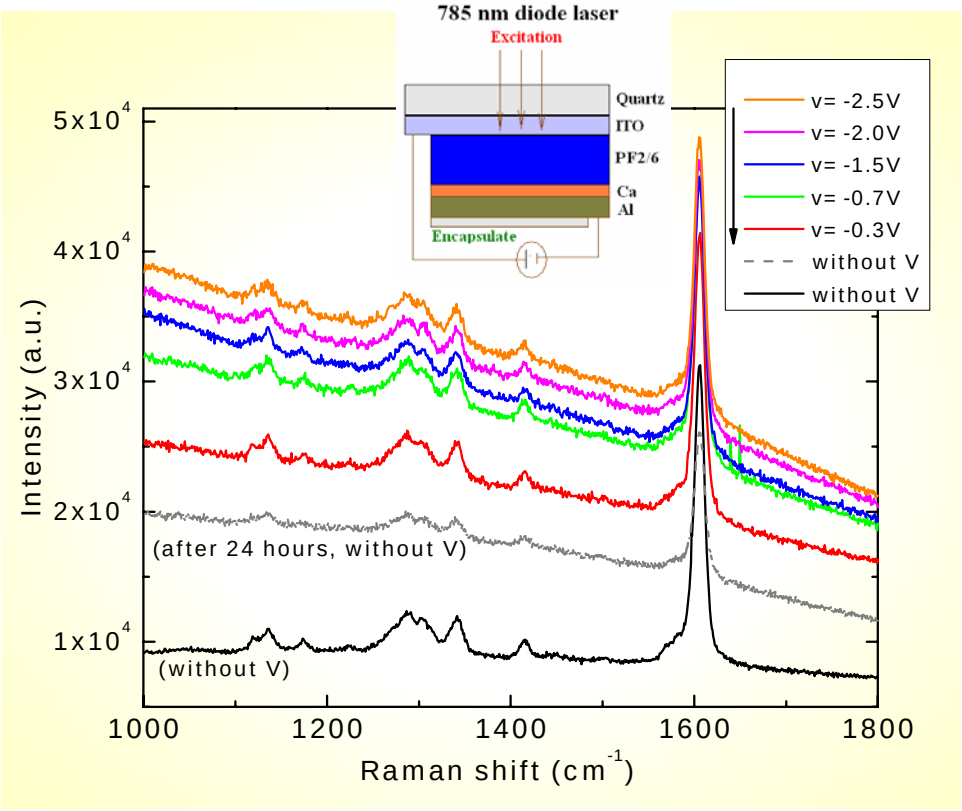

Figure (7.42): Raman spectra of PF2/6 from a LED structure at selected values of the bias voltage. The inset shows the schematic of the PF2/6-based device.

Prior to the application of an external voltage, the sample was illuminated with a UV lamp for ~60s and then switched off. Since the polymer is all sealed with an epoxy the probability of photo-oxidation and thereby damaging the sample is very small. This was also checked by measuring the PL; no oxygen defect related emission was observed in the PL after photoexcitation. Photoexcitation results in excitons that dissociate to generate free carriers (most likely polarons here) in the presence of an external bias. This is also seen as an enhanced current through the device. Increasing background in the Raman spectra is clearly seen with increasing external bias as shown in Fig.7.42. The individual spectra are not shifted vertically; the increase in the background is a real effect. No significant changes in Raman peak positions or relative intensities are observed with the application of external bias. The second spectrum from the bottom was measured from the device without any voltage after 24 hours. It is clearly seen that the background is lower but not the same as the first Raman spectrum, indicating long lifetimes for the accumulated charges.

Fig. 7.43 shows the Raman spectra from *p*-doped PF2/6 films; the bottom most spectrum is from an undoped film. The asterisks represent Raman peaks from the dopant molecule. The incident laser power and integration times were the same for all films. The 35 % doped film clearly shows a broad electronic background centered at 0.198 ± 0.0016 eV. Single-layer LED structures were made with the 25% *p*-doped PF2/6 film. The doping density was calculated from MIS structure using $C-V$ method for both as-is and 25 wt % doped PF2/6 sample. The doping density for as is sample was 2.25 x 10^{18} cm^{-3} where as for 25 wt % doped sample it was 5.5 x10^{19}-1.1 x10^{20} cm^{-3}. The current density versus voltage is shown for an udoped PF2/6 and the *p*-doped PF2/6 diode in Fig. 7.43

inset (b). The latter shows almost two orders of magnitude higher current densities. Fig. 7.43 inset (a) shows the Raman spectra from the doped device for selected bias voltages (without any photoexcitation). The Raman background decreases with increasing bias voltages and the effect is completely reversible.

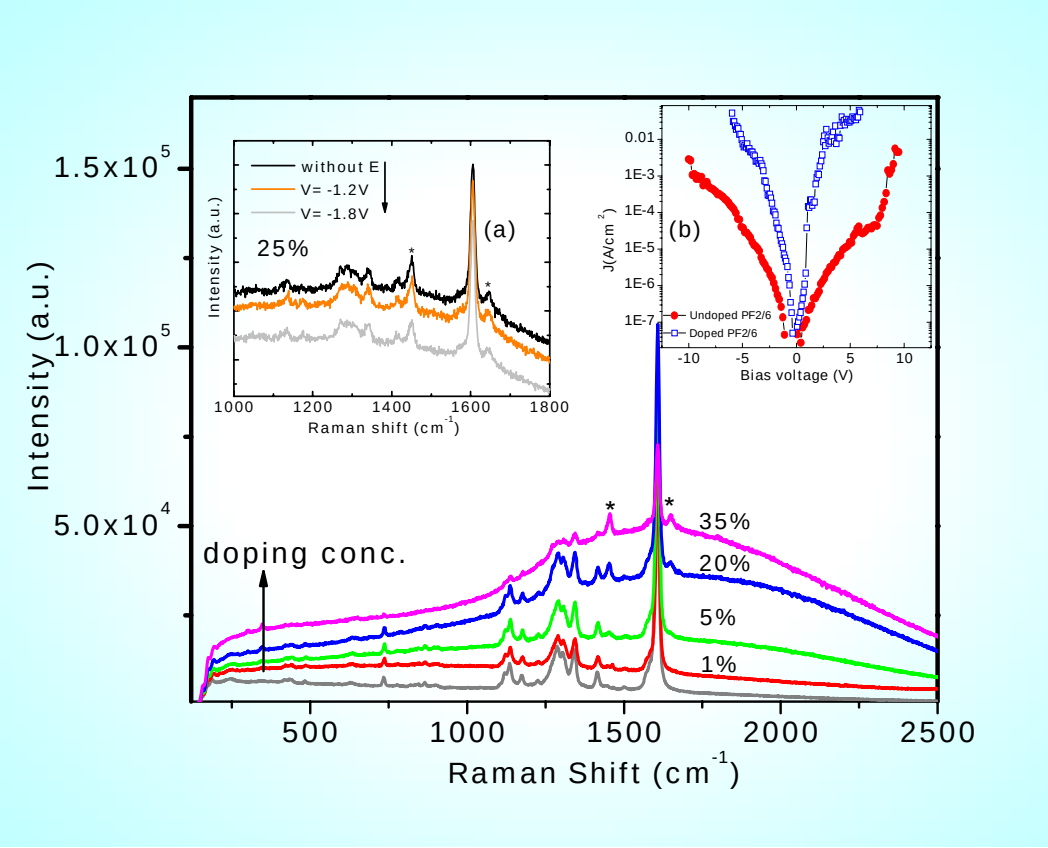

Figure (7.43): Raman spectra of a *p*-doped PF2/6 and an undoped PF2/6 film. (a) Raman spectra of *p*-doped film from a light-emitting diode structure at selected values of voltages. (b) Current density versus voltage of undoped and *p*-doped PF2/6-based diodes.

For the photogenerated carriers an increasing Raman background by the application of an external bias (as seen in Fig. 7.42) is accompanied by an asymmetry of the Raman

peaks, characteristic of a Breit-Wigner-Fano (BWF) resonance. This asymmetry is more pronounced for the Raman peaks in the 1300 cm^{-1} region but since the 1605 cm^{-1} is the strongest we do a complete analysis for the latter Raman peak. To determine the asymmetry and the linewidth as a function of increasing voltage, we fit the 1605 cm^{-1} Raman peak with BWF line shape, which is given by [49,55]

$$I(\omega) = I_0 \frac{[(\omega - \omega_0)/q + \Gamma]^2}{(\omega - \omega_0)^2 + \Gamma^2}, \tag{7.2}$$

where ω_0 is the discrete phonon frequency and Γ is the width of the resonant interference between the continuum and discreet scattering channels. The asymmetry parameter (*1/q*) depends on the average electron-phonon matrix element *M* and the Raman matrix elements between the ground and excited states of the phonon and charge carrier.[51] The broadening parameter is given by

$$\Gamma = \pi M^2 D(\omega). \tag{7.3}$$

In Eq. 7.3, $D(\omega)$ is the combined density of states for the electronic transitions. For nonzero density of states the spectral function $I(\omega)$ will reveal an antiresonance when

$$q = -(\omega - \omega_0)/\Gamma \tag{7.4}$$

Fig. 7.44 shows the asymmetry parameter of the 1605 cm^{-1} Raman peak of the undoped film versus bias voltage. The peak has a very small asymmetry at the onset (without any bias). Since the current is symmetrical about zero voltage (Fig. 7.43 (b)), forward or reverse bias shows the same behavior in the Raman spectrum for the range of voltages used in this work. With increasing external bias both the background and the asymmetry parameter increases. The Fig. 7.44 (a) shows that *1/q* varies linearly with the linewidth as expected from Eqs. (7.2) and (7.3), assuming the average electron-phonon

matrix element and the Raman matrix elements between the ground and excited states are roughly constant. *1/q* values are plotted for the 1605 and the 1342 cm^{-1} Raman peaks of the doped films. The 1342 cm^{-1} peak show a positive asymmetry signaling that the peak of the electronic continuum lies above its frequency. Since the continuum appears almost right at the peak position of the 1605 cm^{-1} peak (as seen for the 35 % doped film), the asymmetry of this Raman peak decreases upon increased doping (Fig. 7.44 (b)).

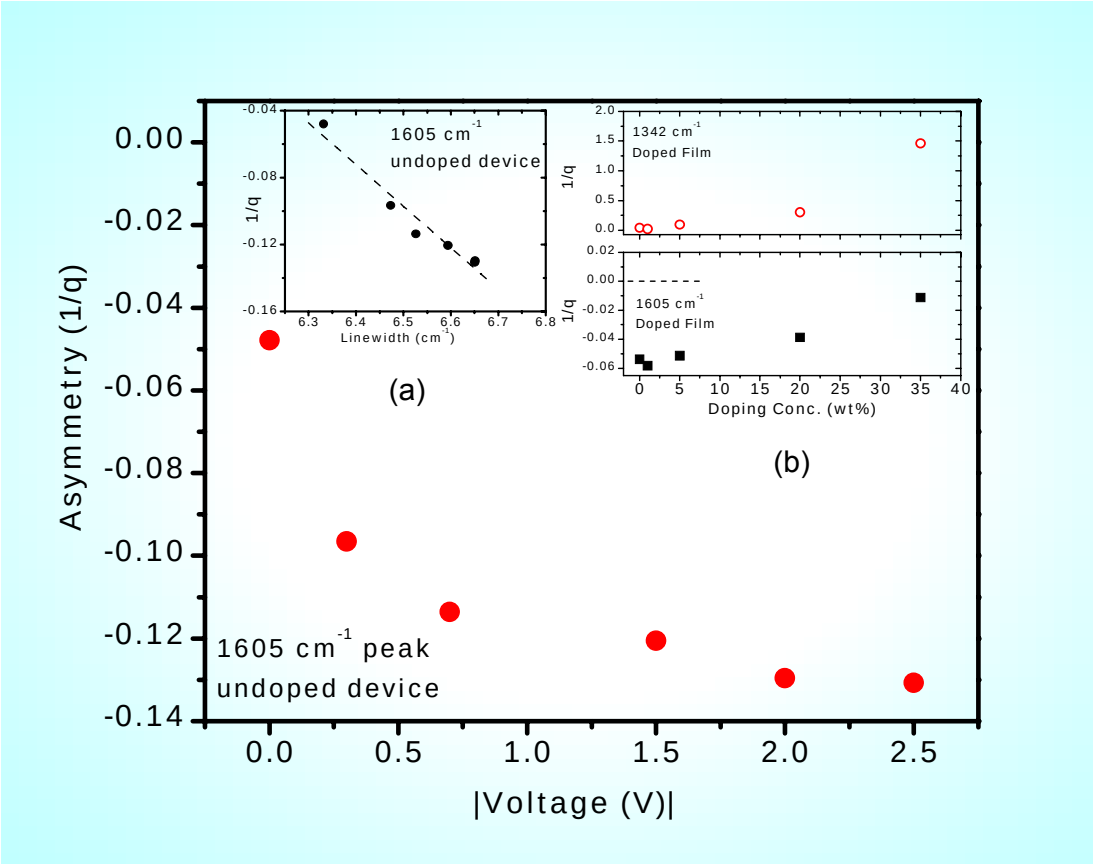

Figure (7.44): Asymmetry parameter (1/q) of the 1605 cm^{-1} Raman peak versus voltage. 1/q is obtained by fits to the Raman peak with a BWF line shape [Eq. (7.2)]. The inset (a) shows the asymmetry parameter to linearly vary with the line width and (b) asymmetry of 1342 cm^{-1} and 1605 cm^{-1} upon increasing doping.

7.6.4 Discussion of Results

Our results clearly show that the doped and photogenerated/injected charge carriers have a different behavior. While doping produces charges of only one polarity, photogeneration produces both positive and negative charges. Since PF2/6 has a nondegenerate ground state photogenerated charges can lead to the formation of either polarons or bipolarons with a certain bandwidth. For low doping concentrations, on the other hand, only polarons are observed.[43] Recent theoretical and experimental works on P3HT-based FETs suggests that charge-induced localized states are most likely bipolarons.[56] Further, photoinduced infra-red active vibrational (IRAV) modes have been used to study the photogeneration and recombination of polarons in CPs, and Fano-type anitresonances in the IRAV modes have been observed.[52]

A single charge carrier added onto a polymer chain forms a polaron with two optically allowed transitions, P_1 and P_2, below the optical gap.[57] In PF8 the polaronic bands appear ~ at 0.3 eV (P_1) and 1.93 eV (P_2).[58] In other polymers like P3HT the P_1 energies are less than 0.2 eV and the bipolaronic absorption is at 0.46 eV.[56] Since the doping here is *p*-type, for low doping concentration one would expect P^+ polarons and thus the BWF interaction arises from the P_1 bands of P^+ type polarons. Moreover, the broad band centered at 0.198 eV for the higher doped samples is in agreement with the P_1 band in PFs. The BWF interaction in the doped films clearly arises from this polaron band. The sign of the asymmetry parameter accurately predicts the energy of the electronic continuum: *1/q* values for the 1342 and 1605 cm^{-1} peaks are positive and negative, respectively, further indicating that the center of the continuum lies between these two discreet Raman modes. Further, the lowering of the overall Raman background

in the 25% doped sample with the application of an external bias (Fig. 7.43(a)) may suggest two possible scenarios: the applied voltage changes the polaronic energy level thereby reducing the BWF effect and/or the injected negative charges result in polaronic absorption of the opposite polarity.

The enhancement of the Raman background with an external bias upon photogeneration of carriers also arises from the P_1 band, since the asymmetry of the 1605 cm^{-1} peak is slightly negative. Typically photoexcitation gives rise to delocalized polarons,[52] and thus the Fano-resonance effect in the photogenerated case is stronger than in doping, which further manifests itself as a higher asymmetry of the Raman peaks. Unlike the doped films no real broad band absorption in seen in the Raman spectra, which points in the direction that the polaron band merges with the extended states. These transitions are expected to be of second order.[56] We point out that the asymmetry parameter of the 1605 cm^{-1} peak is smaller compared to the backbone C-C stretch frequencies in the 1250-1350 cm^{-1} region. For the same value of current and voltage, the C-C stretch mode at 1340 cm^{-1} shows an asymmetry value of ~ -0.3 compared to ~ -0.13 for the 1605 cm^{-1} peak. It is interesting to point out that similar negative values of the asymmetry parameter are observed in alkali-doped C_{60} (M_3C_{60}) for the squashing mode of the fullerene molecule.[55]

In summary, our work demonstrates the potential of near IR Raman spectroscopy for probing electronic excitations in organic light-emitting diode structures. Differences in doped versus photogenerated charges in LED structures are determined by a line-shape analysis of the Raman peaks. Future work involves a more quantitative analysis of the electron-phonon interactions by tuning the BWF resonance effect, which may be

achieved by applying hydrostatic pressure, and changing the incident excitation wavelength.

References:

[1] D. Braun, A. J. Heeger, Appl. Phys. Lett., **58**,1991(1982).

[2] D.D. C. Bradley, Synth. Met., **54**, 401 (1993).

[3] V.N. Bliznyuk, S.A.Carter, J.C. Scott, G. Klarne**r,** R.D. Miller, D. C. Miller, Macromolecules. **32**, 361(1999).

[4] J. Teetsov, M.A. Fox, J. Mater, Chem, **9**, 2117(1999).

[5] M. Sims, D. D. C. Bradley, M. Ariu, M. Koeberg, A. Asimakis, M. Grell, D. G. Lidzey, *Adv. Funct. Mater.*, **14**,765 *(*2004).

[6] Xiao Hui Yang, Frank Jaiser, Dieter Neher, Pa Dreyia V. Lawson, Jean-Luc Bredas, Egbert Zojer, Ronal Gunter, Patricia Scanduicci de Freitas, Michael Forster, Ulli Scherf, Adv. Func. Mater., **14**, No 11,1097-1104 (2004).

[7] Klaus Becker, John M. Lupton, Jochen Feldmann, Benjamin S. Nehls, Frank Galbrecht, Deqing Gao, and Ullrich Scherf, Adv. Funct. Mater., **16**, 364–370 (2006).

[8] A.L. Burin, and M.A. Ratner J. Polym. Sci., Part B: Polym. Phys. **41**, 2601 (2003).

[9] M.N. Bussac and L. Zuppiroli, Physical Review B, **55,** 15587 (1997).

[10] W. Graupner, G. Leditzky, G. Leising, U. Scherf, Phys. Rev. B **54**, 7610(1996).

[11] P.D. twnsend and R.H. Friend, Phys. Rev., B **40,** 3112(1989).

[12] A.J. Campbell, D.D.C. Bradley, D.G. Lidzey, J. appl. Phys., **82,** 6326(1997).

[13] M.A. Lampart and P.Mark, "Current injection in solids", Academic Press, New York, (1970).

[14] A. Rose, Phys. Rev **97**, 1538 (1955).

[15] M. A. Lampert and R. B. Schilling, RCA Report PTR, 2524, 1969 (unpublished).

[16] M. A. Lampert, Phys. Rev., **103**, 1648 (1956).

[17] A. Rizzo, G. Micocci and A. Tepore, Journal of Appl. Phys, **48**, 3415 (1977).

[18] P. Mark and V. Helfrich, J. Appl. Phys. **33**, 205 (1962).

[19] J. Sworakowski and K. Pigon, J. Phys. Chem. Solids **30**, 491 (1969).

[20] J. L. Hartke, Phys. Rev., **125,**1177 (1962).

[21] W. L. Medlin, Phys. Rev., **123**, 502 (1961).

[22] M. Pope and C.E. Swenberg, "Electronic Processes in Organic Crystals and Polymer", Oxford University Press, Oxford (1999).

[23] A. Kadashchuk, R. Schmechel, H. von Seggern, U. Scherf, and A. Vakhnin, J. Appl. Phys. **98**, 024101 (2005).

[24] R. Schmechel and H. von Seggern, Phys. Stat Sol. A, **201**, 1215 (2004).

[25] S. Nespurek and J. Sworakowski, J. Appl. Phys. **51**, 2098 (1980).

[26] D. V. Lang, X. Chi, T. Siegrist, A.M. Sergent, and A. P. Ramirez, Phys. Rev. Lett., **93**, 076601 (2004).

[27] I. Musaa and W. Eccleston, S. J. Higgins, J. Appl. Phys. **83**,5558 (1998).

[28] E. A. Silinsh and V. Cˇ apek, Organic Molecular Crystals: Interaction, Localization, and Transport Phenomena (AIP Press, Woodbury, 1994).

[29] R. W. I. de Boer and A. F. Morpurgo, Physical Review B **72**, 073207 (2005).

[30] Bo Gan et. al.J. Appl. Phy., **89**, 5747(2001).

[31] I. Solomon and R. Benferhat, H. Tran Quoc, Phys. Rev. B **30**, 3422 - 3429 (1984).

[32] S. Gangopadhyay,B. Schröder and J. Geiger, Phil. Mag. B **56**, No 3, 321-333 (1986).

[33] M. Raja, N. sedghi, S. Badriya, S. J. Higgins, G.C. R Lloyd and W. Eccleston, Proceedings of ESSDERC, Grenoble, France, (2005).

[34] M.Yun, S. Gangopadhyay, M. Bai, H. Taub, M. Arif, and S.Guha (Organic Electronics, 2007 in press).

[35] B. Tanto, S. Guha, C.M. Martin, U. Scherf, and M.J.Winokur, Macromolecules, **37**, 9438 (2004).

[36] D. V. Lang, X. Chi, T. Siegrist, A.M. Sergent, and A. P. Ramirez, Phys. Rev. Lett., **93**, 076601(2004).

[37] U. Scherf and E.J.W. List, Adv. Mater., **14**, 477 (2002).

[38] Dimitry Poplavskyy, Wencheng Su, and Franky Do, J. Appl. Phys., **98**, 014501 (2005).

[39] K. Murata, S. Cina, N.C. Greenham, Appl. Phys. Lett **79**, 1193 (2001).

[40] R.W. I. de Boer, M. Jochemsen, T. M. Klapwijk, A. F. Morpurgo, J. Niemax, A. K. Tripathi, and J. Pflaum, J. Appl. Phys. **95**, 1196 (2004).

[41] Reynaert, K. Poot, V. Arkhipov, G. Borghs, and P. Heremans, J. Appl. Phys. **97**, 063711 (2005).

[42] Lewis Rothberg, Bell laboratories, Lucent Technologies, 600 Mountain Ave., Murray Hill, NJ 07974, USA in "Primary Photoexcitations in Conjugated Polymers: Molecular exciton versus semiconductor band model", edited by N.S. Sariciftci, World Scientific, (1997).

[43] P.A. Lane, X. Wei, and Z. V. Vardeny, in "Primary Photoexcitations in Conjugated Polymers: Molecular exciton versus semiconductor band model", edited by N.S. Sariciftci, World Scientific, ((1997).

[44] A.J. Heeger, S. Kivelson, J.R. Schrieffer, and W.-P. Su, Rev. Mod. Phys.,**60**, 781 (1988).

[45] R. Österbacka, C. An, X.M. Jiang, and Z. Vardeny, Science, **287**, 839 (2000).

[46] Z.Q.Li, G.M. Wang, N. Sai, D. Moses, M.C. Martin, M.Di Ventra, A.J. Heeger, and D.N. Basov, Nano Lett. **6**, 224 (2006).

[47] Yukio Furukawa, department of chemistry, School of science, The university of Tokyo, Bunkyo-ku, Tokyo 113, Japan, in "Primary Photoexcitations in Conjugated Polymers: Molecular exciton versus semiconductor band model", edited by N.S. Sariciftci, World Scientific, (1997).

[48] C. Volz, M. Arif, and S. Guha, J. Chem. Phys. **126**, 064905 (2007).

[49] C.M. Martin, S. Guha, M. Chandrasekhar, H.R. Chandrasekhar, R. Guentner, P. Scanduicci de Freitas, and U. Scherf, Phys. Rev. B **68**, 115203 (2003).

[50] L. Pintschovius, J.A. Verges, and M. Cardona, Phys. Rev. B **26**, 5658 (1982).

[51] M. Chandrasekhar, J.B. Renucci, and M. Cardona, Phys. Rev. B **17**, 1623 (1978).

[52] R. Österbacka, X.M. Jiang, C.P. An, B. Horovitz, and Z.V. Vardeny, Phys. Rev. Lett., **22**, 226401 (2002).

[53] J. Hwang and A. Kahn, J. Appl. Phys. **97**, 103705 (2005).

[54] B. Tanto, S. Guha, C.M. Martin, U. Scherf, and M.J. Winokur, Macromolecules **37**, 9438 (2004).

[55] P. Zhou, K.A. Wang, P.C. Eklund, G. Dresselhaus, M. S. Dresselhaus, Phys. Rev. B, **48**, 8412 (1993).

[56] N. Sai, Z.Q. Li, M.C. Martin, D.N. Basov, amd M. Di Ventra, Phys. Rev. B, **75**, 045307 (2007).

[57] K. Fesser, A. R. Bishop, and D. K. Campbell, Phys. Rev. B, **27**, 4804 (1983).

[58] A.J. Cadby, P.A. Lane, H. Mellor, S.J. Martin, M. Grell, C. Giebeler, D.D.C. Bradley, M. Wohlgenannt, C. An, and Z.V. Vardeny, Phys. Rev. B, **62**, 15604 (2000).

CHAPTER 8

Summary and future work

Two important polyfluorene derivatives PF8 and PF2/6 were studied in depth for this research work. The performance and efficiency of polymer based devices depend largely on the structural properties and charge transport processes. Apart from charge delocalization some of the intrinsic factors which are very important to charge transport in π CPs are interchain interactions, coformations of side groups, their orientation as well as arrangements in nanometer length scale. Other parameters that impact transport on longer length scale include overall structure of the materials, presence of defects, methods of fabrication, and processing of semiconducting polymers.

In this research work we have investigated intrinsic properties like chain morphologies, conformations of side groups as well as structural phases of PF8 from temperature-dependent Raman scattering studies cast from different solvents. In order to understand their impact on electroluminescence, LEDs were fabricated and tested by casting the PF8 film using various thermal treatments. Charge transport and structural defects were studied using SCLC model from one carrier PF based diodes and finally Raman scattering studies from LED structures were investigated to get information about polaronic and bipolaronic absorption.

The motivation and object of studying PF as the active material in OLEDs for this research work is presented in Chapter 1. This is then followed by providing a theoretical background of semiconducting CP in Chapter 2, where the origin of π conjugation,

electronic transition in π-CP and their application in existent devices are discussed. A detailed description of PFs, its derivatives as well as their conformational isomers are also discussed. In Chapter 3 we have explained the various experimental techniques and setup used in this work. The basic physics of OLEDs and their operation mechanism is given in Chapter 4. A detailed theoretical description of SCLC with $I-V$ characteristics for discrete and distribution of traps is given in Chapter 5. The techniques for calculating the DOS and their distribution with respect to quasi Fermi energy level from SCLC are also presented.

There are many ambiguities in the structural-property relationships in PFs. The structural properties of PF8 are extremely sensitive to the choice of functionalizing side chains. A major controversy was the origin of the beta phase in PF8. It was thought to originate from conformations at longer length scales. By a combination of Raman scattering and theoretical modeling we show that the origin of the low energy beta phase lies in the conformation of the side chain. Our vibrational frequencies and intensities determined from Raman scattering studies as a function of thermal cycling establish a correlation between the conformational isomers and the side and main chain morphology. Density-functional calculations of the vibrational spectra of single chain oligomers in conjunction with the experimental results demonstrate the incompatibility of the β phase with the overall crystalline phase in PF8. These studies provide important steps towards the development of a universal picture of structure-property relationship in CPs that mainly derive from chain morphology at short length scales.

EL measurements from PF8-based LEDs also reveal the presence of beta conformer which strongly coupled to the overall crystalline phase of the polymer. The as-is film has

a higher fraction of the beta phase and thus resulting in a more red-shifted spectrum. Devices fabricated from thermally cycled PF8 film indicate the reduced fraction of this conformer with blue shift in EL spectra.

Charge carrier injection and transport properties of PF based light emitting diode are extensively studied. Using the theoretical models of SCLC with discrete and distribution of traps, the $I-V$ characteristics of these devices are analyzed. A unified picture of the hole transport through one carrier device is presented. Our $I-V$ measurements for PF2/6-based blue-emitting polymers show an exemplary system for charge transport with discrete level shallow traps. The charge injection in this blue-emitting polymer with a high level of molecular disorder is for the first time successfully modeled by discrete energy levels for traps. These unexpected findings suggest that charge injection and transport most probably occur through regions of ordered chain segments in the polymer. $I-V$ characteristics of devices fabricated from as-is PF2/6 shows discrete set of shallow traps which on subsequent measurements induces additional distribution of traps but subsequent bias sweeps in the annealed sample does not introduce additional traps.

Based on the results of our SCLC in PF2/6 based diodes we have investigated the charge transport as a function of sample thickness to uncover the origin of traps. The thickness dependent SCLC measurements show the influence of both surface and bulk traps on charge transport. For very thin samples the total amount of interface traps may dominate over the total amount of bulk traps and may subsequently change the behavior of the $I-V$ characteristics. Our temperature dependence of $I-V$ and dc conductivity measurements suggests thermal assisted variable-range hopping transport instead of band transport in these materials.

Since charge carrier injection and doping in CPs can induce structural deformation with the formation of self-localized excitation states as polarons or bipolarons inside the band gap, one needs a deeper understanding of creation, transport, and decay processes of these excitations in conjugated polymer devices. We have focused on Raman scattering studies from PF2/6-based LED structures in the presence of photoinduced and doped charge carriers with an external electric field to get insight into polaronic and bipolaronic absorption. Raman scattering studies with doping and in the presence of injected and photo-generated charge carriers show increasing backgrounds with asymmetric Briet-Wigner-Fano (BWF) line shapes, indicating strong electron-phonon interactions. Differences in doped versus photogenerated charges in LED structures are determined by a complete line-shape analysis of the Raman peaks. Our work has demonstrated that Raman spectroscopy has a great potential for probing electronic excitations in organic light-emitting diode structures.

Future work

This research opens up some new avenues for future research in the design and development of new optoelectronic devices based on PF and other CPs. The SCLC phenomenon observed in as-is PF2/6 diodes may be exploited in making switching devices. Our SCLC measurements show two distinct conduction levels one before trap filling and the other due to filling of traps. Since optical excitation can be used to go from a high resistivity state to a low resistivity state (detrapping), we can use it as a bi-level device.

Since our SCLC measurements of PF2/6 shows an excellent system for charge transport, one of our future research work will be to develop new devices like FETs and photovoltaics based on PF2/6 to investigate charge carrier transport.

Another possible area of future research work will be to reduce the interface defects which form during OLED fabrication in order to increase current densities which will eventually improves the device efficiency.

Since Raman spectroscopy provides a great potential for probing electronic excitations in organic light-emitting diode structures. Our future work involves a more quantitative analysis of the electron-phonon interactions by tuning the BWF resonance effect, which may be achieved by applying hydrostatic pressure, and changing the incident excitation wavelength. Also, with the development of PF-based FETs one of our goals will be to study electric field induced Raman scattering from this structure to explore the behavior of injected charge carrier at the metal organic interfaces.

Publications

- *"Probing electronic excitations in organic light-emitting-diodes via Raman scattering"* **M. Arif** , S. Guha, A. Tsami and U. Scherf (APL, 2007 in press).

- *"Structural and spectroscopic investigations of bulk poly[9,9-n-dioctyl fluorene]"*, B. Tanto, S. Guha, **M. Arif**, and M. J. Winokur. (Submitted, 2006).

- *"Influence of thermal cycling on the interface states in ethyl-hexyl substituted polyfluorene-based metal-insulator semiconductor devices"* M.Yun, S. Gangopadhyay, M. Bai, H. Taub, **M. Arif**, and S. Guha (Organic Electronics, 2007 in press).

- *"Polyfluorene as a model system for space-charge-limited conduction"* **M. Arif**, S. Guha, M.S. Yun, S. Gangopadhyay, K. Ghosh, L. Fadiga, F. Galbrecht, and U. Scherf , Physical Review B, **75**, 195202 (2007).

- "*Crystallization of amorphous silicon by self propagation of nano-engineered thermites*", M. Hossain, S. Subramanian, S. Bhattacharya, Y. Gao, S. Apperson, R. Shende, S. Guha, **M. Arif**, K. Gangopadhyay, and S. Gangopadhyay J. Appl. Phys., **101**, 054509 (2007).

- "*Conformations in polyfluorenes: a combined theoretical and experimental Raman scattering study*", C. Volz, **M. Arif**, and S. Guha**,** Journal of Chemical Physics, **126**, 064905 (2007).

- *"Capacitance-Voltage characterization of polyfluorene-based metal-insulator-semiconductor diodes"*, M.S. Yun, R. Ravindran, M. Hossain, S. Gangopadhyay, U. Scherf, T. Bünnagel, F. Galbrecht, **M. Arif** and S. Guha Appl. Phys. Lett., **89**, 013506 (2006).

- *"Chain morphologies in semi-crystalline polyfluorene: evidence from Raman scattering"* **M. Arif**, C. Volz, and S. Guha, Physical Review Letters **96**, 025503, 20th January (2006).

- *"Chain morphologies in blue-emitting polyfluorenes: impact on light-emitting diodes",* S. Guha, **M. Arif**, and C. Volz, Mat. Res. Soc. Symp. Proc. **916**, Warrendale , PA , DD01 (2006).

- *"Electrical characterization of polyfluorene-based metal-insulator-semiconductor diodes"*, M.Yun, **M. Arif**, S. Gangopadhyay, and S. Guha, Mat. Res. Soc. Symp. Proc. **973 E**, Warrendale, PA, M07-08 (2006).

- *"Development of strain reduced GaN on Si (111) by substrate engineering"*, M. Jamil, J. R. Grandusky, V. Jindal, F. Shahedipour-Sandvik, S. Guha, and **M. Arif**, Applied Physics Letters, **87**, 082103 (2005).

- *"Raman scattering from organic light emitting diodes",* S. Guha, **M. Arif**, J.G. Keeth, T.W. Kehl, K. Ghosh, and R.E. Giedd, Proceedings of the 27th International Conference on the Physics of Semiconductors, eds. J. Menendez and C. G. Van de Walle, American Institute of Physics 1079 (2005).

- *"Effect of Low Temperature Annealing on High Field Magnetoresistance and Hall effect in (Ga,Mn)As Dilute Magnetic Semiconductors"* K. Ghosh , **M. Arif**, T. Kehl, R.J.Patel, S. R. Mishra, and J. G. Broerman, S. R. Misrha, Mater. Res. Soc. Symp. Proc. Vol. **831**, (2005).

- *"Development of low dislocation and strain reduced GaN on Si(111) by substrate engineerin""*, M. Jamil , J. R. Grandusky , V. Jindal , F. Shahedipour-Sandvik , S. Guha and **M. Arif**, Proc. SPIE Int. Soc. Opt. Eng. **5941** , 59411E (2005).

VITA

Mohammad Arif was born in Bangladesh on 2nd February 1974 in a small city Dhaka, Bangladesh. Arif graduated with his bachelor's Degree in Metallurgical Engineering (Met-E) under the Department of Materials and Metallurgical Engineering (MME), Bangladesh University of Engineering and Technology, (BUET) Dhaka, Bangladesh in 1998. He came to United States in December 2000 and enrolled in graduate program in Materials Science in the Department of Physics, Astronomy and Materials Science, Missouri State University, Springfield, Missouri. After finishing his Masters in Materials Science on July 2003, Arif has enrolled in graduate program in Physics at University of Missouri Columbia, and finished his Masters degree in Physics from the Department of Physics and Astronomy. Arif will be graduating with his PhD degree in Physics in summer 2007 from the same Department. He will join as a post doctoral fellow with Dr. Shubhra Gangopadhyay at the Department of Electrical and Computer Engineering, University of Missouri Columbia, Columbia, Missouri from July 2007.